Numerical Study of Geomechanical Fault Reactivation and Caprock System Integrity in CO_2 Storage: A Sensitivity Analysis Using Fully Coupled Flow-Deformation Three-Dimensional Distinct Element Modelling

by

TOREKELDI MARATOV

THESIS SUPERVISOR

ALI MORTAZAVI

Thesis submitted to the School of Mining and Geosciences of Nazarbayev University in Partial Fulfillment of the Requirements for the Degree of

Master of Science in Mining Engineering

Nazarbayev University

30.04.2025

ORIGINALITY STATEMENT

I, Torekeldi Maratov, hereby declare that this submission is my own work and to the best of my knowledge it contains no materials previously published or written by another person, or substantial proportions of material which have been accepted for the award of any other degree or diploma at Nazarbayev University or any other educational institution, except where due acknowledgement is made in the thesis.

Any contribution made to the research by others, with whom I have worked at NU or elsewhere is explicitly acknowledged in the thesis.

I also declare that the intellectual content of this thesis is the product of my own work, except to the extent that assistance from others in the project's design and conception or in style, presentation and linguistic expression is acknowledged.

Signed on 07.04.2025

ABSTRACT

To examine fault reactivation and caprock seal integrity during CO_2 injection, a fully coupled flow-deformation model is used to evaluate geomechanical performance. The In Salah greenhouse gas storage project in Algeria is used as a field example to investigate fault slip and potential for induced seismicity across geomechanical and operational conditions. A sensitivity analysis is conducted with variations in fault geomorphology, in-situ stress ratio, injection pressure, and rate. Results indicate fault slip is sensitive to fault dip angles, where faults with 15° fault dips experience the largest shear displacement (1.07×10^{-2} m) relative to higher dipping fault angles (60° faults experience maximum slip of 2.24×10^{-3} m).

In addition, variations in the in-situ horizontal-to-vertical stress ratio revealed that raising this ratio from 1.0 to 2.0 led to a 50% decrease in vertical displacement, meaning horizontal stresses are beneficial for caprock containment. The evaluated parameters of fluid injection revealed that the injection rate affects fault stability; increasing the rate from 5 l/s to 6 l/s increased fault slip by 55%, with the resultant maximum displacements of 1.34 mm and 2.08 mm, respectively. Yet, increasing fluid viscosity by 20% increased fault slip from 1.34 mm to 1.26 mm, meaning increased fluid viscosity equals reduced fluid migration and pressure stabilization, thus decreasing fault reactivation likelihood.

Furthermore, the results showed that caprock strength controls deformation; deformation occurred in the form of 0.0004 m vertical displacement up for weak caprocks, but no vertical displacement occurred for strong caprocks. Therefore, this shows caprock failure is dependent upon stress regime and fluid properties with a possibility of failure via leakage. Ultimately, this study contributes to the body of knowledge about the complex geomechanical and fluid interactions associated with injecting/sequestering CO_2 into/from subsurface geological formations. It highlights fault geometry as well as the relative location of injection, injection volume and pressure, and caprock strength as important factors of stress manipulation for successful sequestration safety over the long term

.

DEDICATION

I dedicate this thesis to my family, whose unwavering support and encouragement have been a constant source of strength throughout this journey. And to all those who inspired and believed in me.

ACKNOWLEDGMENT

The completion of this thesis was made possible through the support and resources provided by Nazarbayev University. I would also like to express my sincere gratitude to Professor Ali Mortazavi for his guidance, supervision, and constructive feedback throughout the course of this research. I also extend my appreciation to the School of Mining and Geosciences for providing a stimulating academic environment and access to relevant facilities that significantly contributed to the progression of this study. I am sincerely thankful to my family for their continuous support and encouragement during the course of my research. Their understanding and patience have been invaluable throughout this academic journey.

TABLE OF CONTENTS

LIST OF FIGURES

LIST OF TABLES

1. INTRODUCTION

1.1 Background

Today's climate change is primarily caused by increased levels of carbon dioxide (CO_2). Increased levels of CO_2 occur from natural and anthropogenic (human-caused) processes; however, the increased anthropogenic processes that plague the world today occur predominantly from burning fossil fuels—coal, oil, and natural gas—for power and fuel for transportation and industry, as well as land-use changes such as deforestation, making cement, and agriculture. Since the Industrial Revolution, levels of CO_2 have risen from 280 parts per million (ppm) to over 410 ppm—an increase of more than 45% (Figure 1; Friedlingstein, 2020). Today, nearly 90% of human-influenced CO_2 emissions derive from cement manufacturing and fossil fuel combustion (Jackson et al., 2018), and since 1958, global carbon emissions attributable to fossil fuel sources have increased from 4 gigatonnes of carbon per year to 12 gigatonnes per year in 2019 (Friedlingstein, 2020).

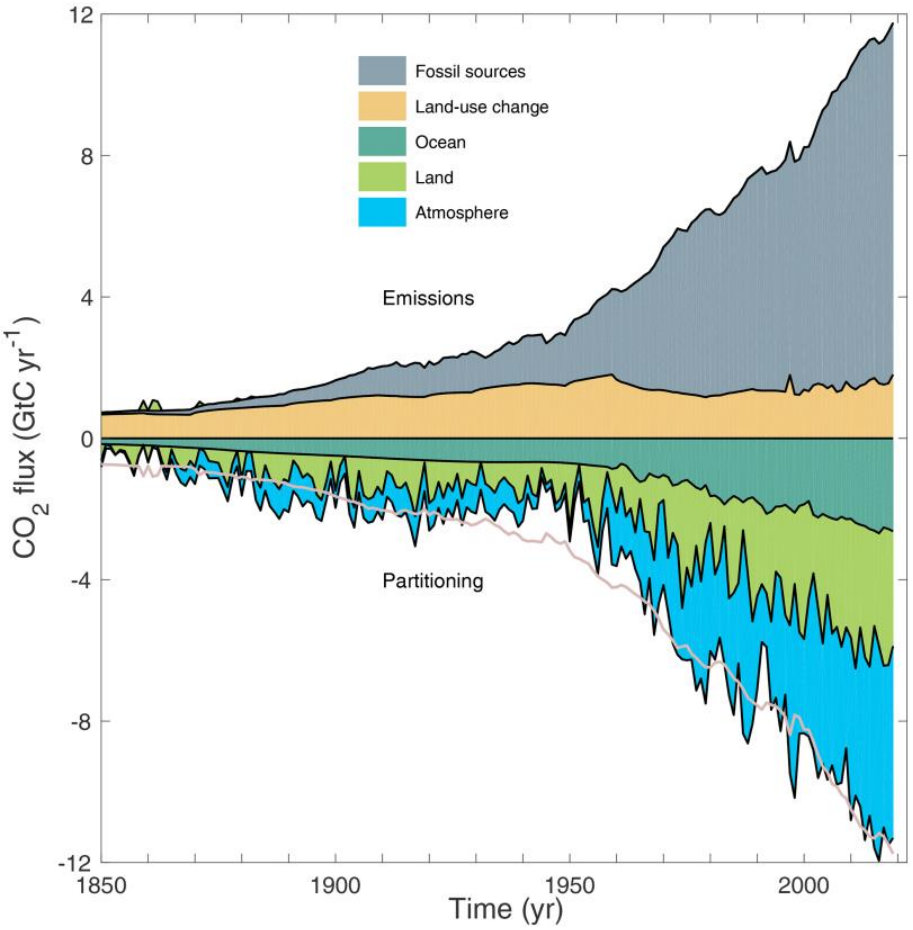

Figure 1. Time evolution of the components of the global carbon budget (Friedlingstein, 2020).

This sustained trend mostly results from economic and population growth, oftentimes outpacing the gains in energy efficiency (Malik et al., 2016; Xia et al., 2020). The impacts of increased CO_2 are global and multidimensional. For instance, global temperatures have already increased by 1.1 degrees Celsius from pre-industrial times, and while some suggest that independent of any further increases, the temperature will grow up to 6 degrees Celsius due to past emissions (Jackson et al., 2019), such drastic increases indicate stable polar ice melt, rising sea levels, ocean acidification, biodiversity loss, and increased frequencies of devastating natural disasters like floods and heat waves (Nunes, 2023; Galdies, 2017). In addition, the long-term effects are increased because CO_2 has a long atmospheric half-life, indicating that no matter how much is created today, a certain percentage will remain in the atmosphere for centuries—for generations—contributing to ongoing radiative forcing (Hansen et al., 2013). This is further complicated with socioeconomic inequity of environmental and social effects; developing nations are most vulnerable to climate shocks, despite contributing low levels to overall international emissions (Allafta & Opp, 2024). Not to mention additional feedback loops that can facilitate further warming, such as permafrost melting and decreased carbon sinks (Friedlingstein, 2020). Thus, when implicating such a large scale, sustainable impact and inequitable impact, understanding the causes and effects of CO_2 emissions is crucial to climate science, policy creation, and mitigation effectiveness.

Carbon capture and storage (CCS) is one of the most often proposed and economically viable methods for reducing net CO_2 emissions. Carbon capture and storage refers to capturing carbon dioxide emissions from the point source and injecting it deep into suitable geological formations in the subsurface (Figure 2). The intent is to keep this greenhouse gas from entering the atmosphere and exacerbating global warming issues (Chang et al., 2022; Cappa & Rutqvist, 2011). As an overall concept, CCS is already somewhat understood. Carbon dioxide can be removed from the flue gas stream at power generation facilities or chemical processing plants. It is removed by chemical absorption or physical separation. What remains after the process is a compressed, dense phase that can be transported—mainly via pipelines—to a storage area. The storage aspect often involves injecting CO_2 into ultra-deep formations, including depleted oil&gas reservoirs, deep saline aquifers, and unmineable coal seams; such formations exist at depths where pressure and temperature sustain supercritical conditions for the carbon dioxide. Under supercritical conditions, CO_2 acts like both a gas and a liquid, which provides space-filling characteristics inside pore spaces of the host rock (Rutqvist & Tsang, 2002; Reyes-Montes et al., 2011).

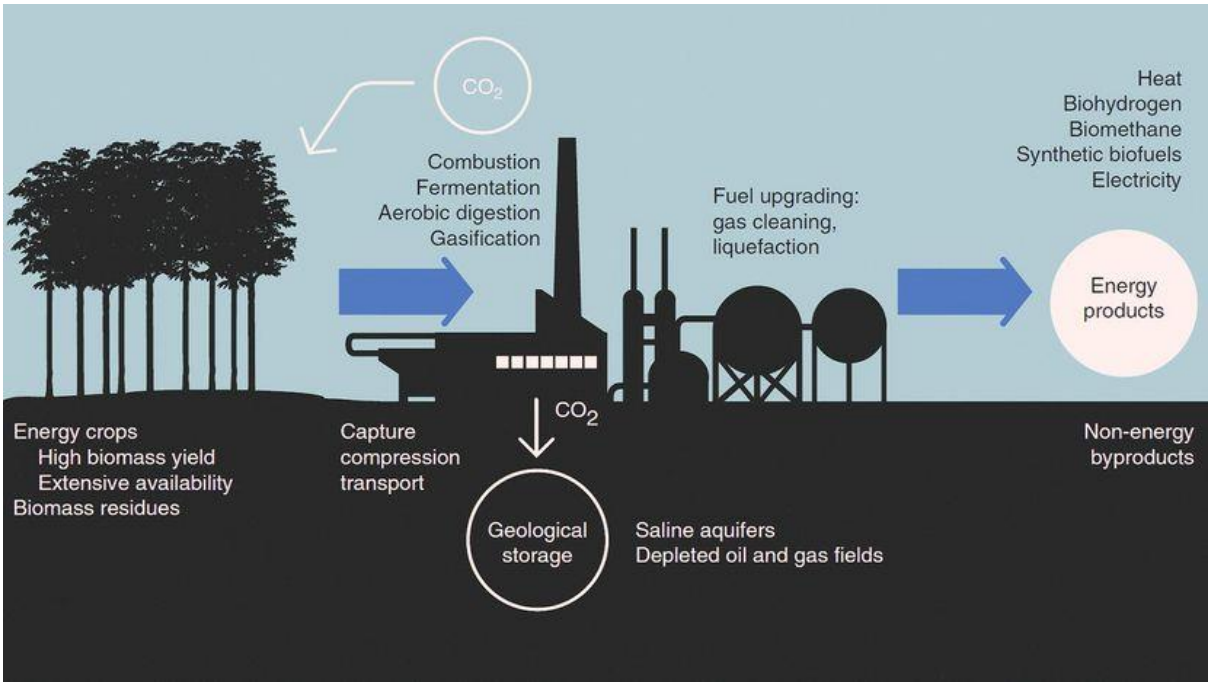

Figure 2. The working principle of carbon capture and storage (Ronca & Mancini, 2008).

There are multiple reasons why these formations keep CO_2 stored over time. For example, structural trapping happens due to an impermeable caprock over the accumulation that prevents vertical movement; resin trapping occurs when the CO_2 is trapped in pore spaces due to capillary pressure; solubility trapping describes cases where CO_2 eventually dissolves into the formation brines; and mineral trapping relies on the eventual transformation of CO_2 into permanent carbonate minerals due to chemical interaction with minerals that form rocks (Cappa & Rutqvist, 2011). All of these forms of trapping allow for better safety and longevity of CO_2 storage either in tandem or series. Yet with billions of tons of pressurized CO_2 stored below the surface, geomechanical concerns exist, primarily the emergence of slip along a naturally occurring fault. Faults are fractures or weaknesses in the lithosphere, and the responsible pressurization of the reservoirs during CO_2 injection changes the stress state of the surrounding environment. Pore pressure increases reduce the effective normal stress that keeps a fault locked, which places it at a nearer-to-failure state. Ultimately, if a slip occurs to a sufficient degree, it can create induced seismicity or compromise the seal integrity of the storage formation, which affects the likelihood of migration from its intended location (Chang et al., 2022; Rongved & Cerasi, 2019). Therefore, understanding the characteristics of faulting in response to fluid injection has become necessary for CCS effective execution. Furthermore, as with any subsurface phenomenon that is complex and requires prediction of various mechanical and fluid migration responses, numerical modeling is essential to predicting CCS

response at the site.

Such models can recreate stresses, pressures, and displacements over time and during CO_2 injection and retention. For example, one type is the Discrete Element Method (DEM), where the geologic setting is formed as particles or blocks with distinct identities that interact depending on predetermined contact laws. The advantage of the Discrete Element Method is that it replicates fracturing conditions of onset and propagation and the granular response or flow of materials that may be better assessed than with traditional continuum approaches. Furthermore, scientists can verify their findings against microseismic reports or surface uplift results to validate or challenge discrepancies. The latter can be slight but also significant up to centimeters for substantial uplifts, as detected by satellite interferometry or deep ground movement sensors. Therefore, ground-deformation readings and microseismics either validate or challenge potential risk assessments. For instance, coupled simulation software has found that (in certain conditions) wells too near critically stressed faults—particularly in the intermediate zone where faults split—are more prone to slip. Yet, despite much advancement, the challenge remains to transition the results from the DEM exposure into reality due to limitations of computing power and the ambiguity of effective properties in the subsurface realm, which are necessary to increase reliability bounds of fault reactivation predictions. Only with appropriate certainty can researchers justify that the recharging process will not hinder later safe and efficient CO_2 sequestration.

1.2. Problem Statement

Efficient long-term geological storage of carbon dioxide (CO_2) calls for a stable subsurface environment where injected fluids stay contained inside specified reservoirs. Fluid injection changes the pore pressure and stress conditions of the reservoir, therefore increasing the risk of fault reactivation and caprock failure. These geomechanical disturbances could weaken the sealing integrity of the storage site, so causing possible leakage or induced seismicity. Although field studies and monitoring data from initiatives like In Salah show proof of such hazards, the highly heterogeneous character of subsurface formations, together with uncertainty in fault architecture and stress regimes, challenges predictive evaluations. Especially under coupled hydro-mechanical conditions, conventional continuum-based models frequently lack the resolution to capture discontinuous behaviors along fault zones and fracture networks. Therefore, there is a demand for high-fidelity numerical models able to mimic fault slip behavior, deformation mechanisms, and the sensitivity of important parameters under

different injection conditions. This study addresses this gap by employing a fully coupled three-dimensional distinct element model (3DEC) to simulate CO_2 injection and evaluate fault reactivation mechanisms and caprock deformation. Therefore, an important study issue is: *How do geomechanical and operational parameters affect fault reactivation and caprock integrity during CO_2 injection in geological storage reservoirs, as assessed using fully coupled three-dimensional distinct element modelling?* To answer this question, the study performs a thorough parametric sensitivity analysis to clarify fault-caprock interactions and help the creation of safer design and operational plans for geological CO_2 sequestration.

1.3. Objectives of the Thesis

1.3.1. Main Objectives

- To analyze the effects of injection and pore pressure propagation on fault reactivation potential of a CO_2 storage reservoir
- To distinguish fault slip and stability concerns
- To evaluate model sensitivities through an extensive parametric study of key parameters' impact on both fault reactivation and storage reservoir stability.

1.3.2. Specific Objectives

- To measure surface and storage reservoir-fault contact zone displacements caused by fault reactivation of a CO_2 storage reservoir based on 3DEC simulations
- To understand fault slip and activation potential through a parametric study of predetermined key parameters within the model (i.e., mechanical properties of host rock, injection rates of CO_2, applied pressures) to note changes
- To assess how various fault geometries affect fault reactivation and surface displacements; the study will see how various orientations and dip angles affect the stresses during CO_2 injections
- To understand the fault slip mechanisms and thus understand the general tendencies.
- To assess whether faults are likely to reactivate in the long term, already reactivating due to prior pressure increases, and thus how this changes the hazards of this reservoir should pressures continue to increase with emissions injection over time.

1.4. Scope of Work

The scope of work surrounding the thesis is composed of multiple steps that correlate in the process. These include both primary and secondary research regarding fault reactivation mechanisms, sufficiency of CO_2 reservoir seal, fault reactivation in general from a micro and macro viewpoint, and displacement contour. More specifically, the following steps will be taken to evaluate the project:

- An extensive literature review of relevant articles, journals, and books related to CO_2 sequestration, fault reactivation, and numerical analysis will be conducted to yield as much qualitative and quantitative information as possible.
- Obtaining and screening the required data related to the chosen CCS site, that is, geological field data such as geomechanical data and fluid data.
- Creating a credible model to evaluate the issue by a distinct element analysis approach.
- Creating necessary sensitivity analyses to be conducted during the analyses.
- Assessment of the surface and fault-reservoir contact zone movement (vertical, lateral) outcomes, fault slip isoquants, pore pressure rise, and assessment.
- Sensitivity study by variation of certain key variables.

2. LITERATURE REVIEW

Geological carbon dioxide (CO_2) sequestration is a relatively new technology that attempts to combat rising emissions of greenhouse gases in the atmosphere. The goal is to capture CO_2 emissions at a point source—such as a power generation plant or industrial facility—and inject the gas underground into geologic formations that can host the emissions for an extended or permanent period of time. This is made possible with great likelihood due to the vast reservoirs available in geological formations like deep saline aquifers, depleted oil and gas reservoirs, and unmineable coal seams (Fentaw et al., 2024; Bason et al., 2024). The purpose of the geological sequestration of CO_2 is to ensure that emissions of carbon dioxide that humans naturally release do not re-enter the atmosphere by keeping the chemical compound associated with climate change below the Earth's surface for an extended or permanent period of time. The means by which the compound can be kept below ground include structural trapping below impermeable geology, residual trapping within pore networks, solubility trapping due to dissolution in brines, and mineral trapping due to chemical reactions that convert CO_2 into stable carbonate minerals (Figure 3; Han et al., 2010; Johnson et al., 2004; Kim et al., 2023).

Relative to sequestration are major concerns such as site integrity, injectivity, and assurance of containment. For example, overlying caprock formations are essential since they provide reassurance of no vertical migration and help prevent the release of buoyant CO_2, for it will rise to the surface. Thus, 3D geological rendering and visualization, geochemical testing and assessment, and computational modeling become commonplace for determining the feasibility of such an end-use application. The combination fulfills the international standards for safety and regulatory compliance of such endeavors.

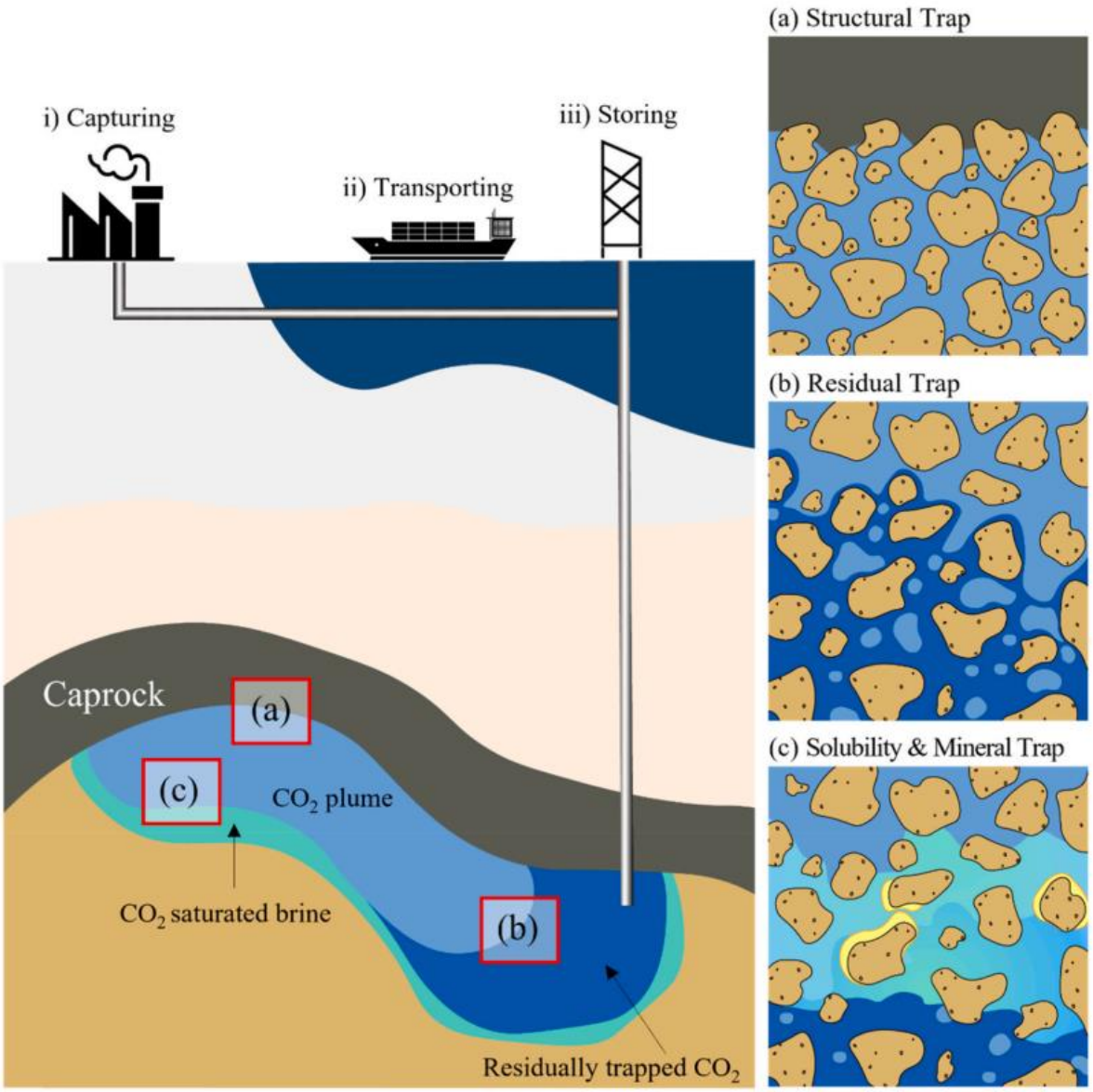

Figure 3. Mechanisms of CO_2 entrapment during CCS: (a) Structural, (b) Residual, (c) Solubility and mineral (Kim et al, 2023)

2.3. Caprock Formations as the Primary Seal

The caprock is comprised of shale or evaporitic rock types and represents the uppermost sealing layer which prevents the ever-injected CO_2 from escaping. The ability to seal comes from low permeability, high capillary entry pressures, mechanical properties, and ineffectiveness to chemical reaction with the acidic CO_2 brines. For a geological sequestration site to be effective over time, a strong and well-understood caprock is necessary (Song & Zhang, 2013). Yet the literature notes multiple potential pathways for leakage through caprock. Diffusion through the matrix, after exceeding capillary entry pressure, and along faults/fractures can all result in leakage. While the first two are immediate concerns for leakage

and occur at a faster rate, they are also more avoidable relative to feasibility assessments than molecular diffusion (Song & Zhang, 2013). Yet the real world finds that complications can arise based upon what is above and below ground. A multiscale characterization study at the Farnsworth Unit, Texas determined that from factors at micropore scale to core fracture scale to regional sedimentary scale, many characteristics determine how caprock will act. Imaging of cores, porosimetry, and geomechanical evaluations indicate that some characteristics may serve as flow paths if not fully characterized during site assessment for selection (Trujillo et al., 2021).

Then there's the concern of caprock geochemistry. For instance, at the Shenhua CCS project site in China, TOUGHREACT modeling of the site determined that with brine dissolution from the injected CO_2 and subsequent mineral interaction, secondary precipitation of carbonates like dawsonite and magnesite occurred over time. This lowered porosity and permeability resulted in some self-sealing behavior over the long term (Yang et al., 2020). But this chemical reaction does not always happen. In laboratory studies, it was determined that brine-rock-CO_2 interactions increase porosity, which decreases seal integrity given certain salinity and pH. For instance, when a study was done on a carbonate caprock, it was found that exposure to CO_2 increased porosity just a slight amount but consistently over duration. The results suggest that mineral dissolution is a bad phenomenon that overshadows any good that could come from precipitation of minerals—although under less than ideal circumstances (Sang & Liu, 2021). Furthermore, mechanical failure is a concern due to the pressurization. More specifically, faults and the like excess pressure (overpressure) create intentional and unintentional failures of containment. In specific, leak pathways are created where caprocks are faulted or fractured along the injection plume pathway.

Concurrent simulation studies have shown how stresses generated by CO_2 injection are likely to cause failure of the caprock due to fracturing (Figure 4). One study used an upscaled integrated geomechanical-compositional model to project probable deformation and failure using different injection rates and formation properties. They found that fracture pressure thresholds could be surpassed easily without precise operational adjustments, leading to avoidable failures (Alvarez et al., 2023). In another study, geomechanical modeling found that the primary mode of failure would be shear fracturing when injection pressures were near 36 MPa (Shu et al., 2024). Ultimately, however, this means that fracture pressures can be expected, suggesting the need for precise measurement of in situ stresses and rock strengths.

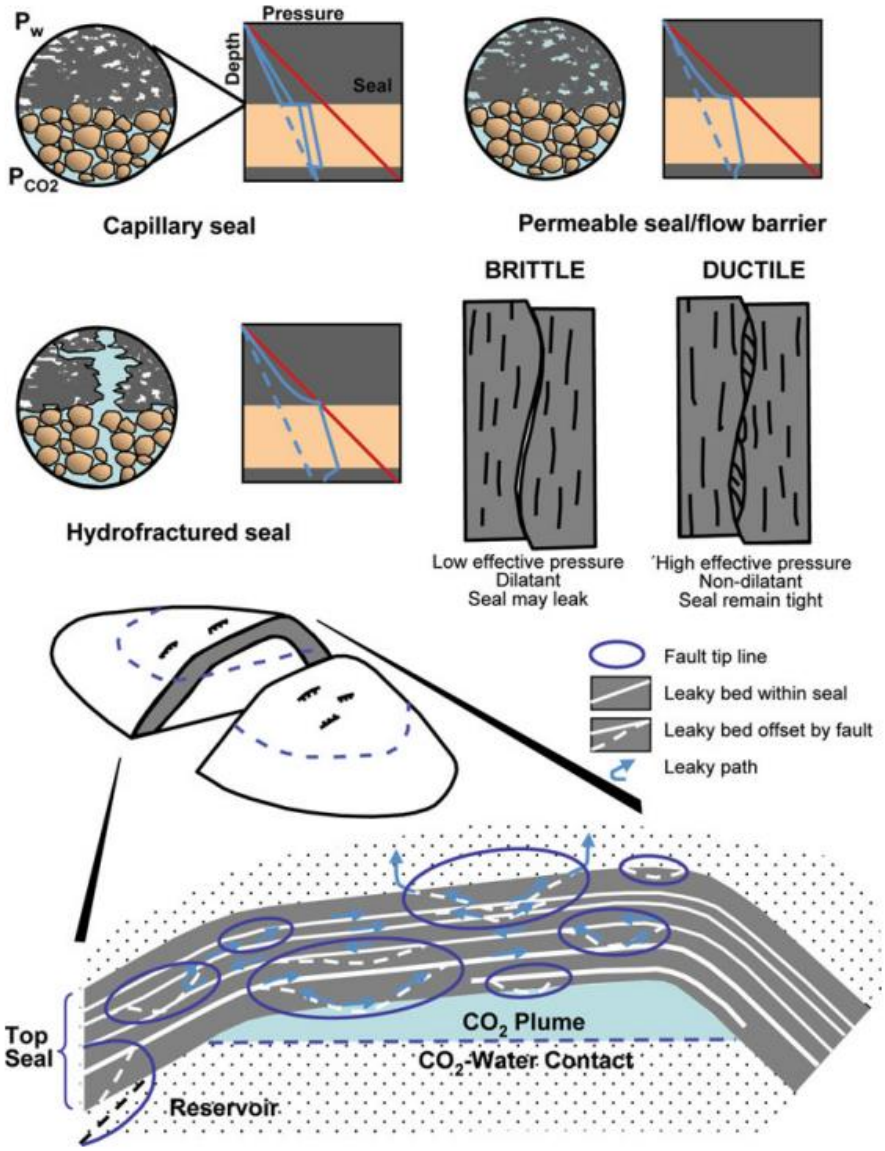

Figure 4. Major sealing properties that influence a top seal continuity in hydrocarbon reservoirs (Rutqvist, 2012)

2.4. Physical and Chemical Trapping Mechanisms Supporting Long-Term Storage

The specifics of how CO_2 successfully remains stored within the subsurface depend upon several trapping mechanisms operating across multiple spatial and temporal scales. Several studies implicate four major trapping mechanisms according to literature: structural trapping, residual (capillary) trapping, solubility trapping, and mineral trapping. Structural trapping occurs when buoyant CO_2 is physically prevented from moving upward, existing downward how passive geologic structures prevent buoyant CO_2 under low permeability caps or within

geological traps as certain structures exist to trap fault-block closures or anticline structures within formations. As long as capillary pressure gradients exist, it will not escape (Han et al., 2010); thus, structural aspects of reservoirs and surrounding formations are important—especially as they relate to plume migration orientation. When the CO_2 is injected downward relative to resident formation fluids, into the target formations, it de-pressures reservoir brine and at least some fraction of CO_2 becomes trapped within pore spaces due to capillary pressure. This is known as residual trapping; it's dependent upon rock wettability, pore throat dimension distributions, and saturation of fluids. For instance, studies modeling sites of residual saturation and capillary pressure devise means by which significant trapping can occur soon after injection and as the buoyant flow dissipates, which serves as a secondary layer of trapping (Figure 5).

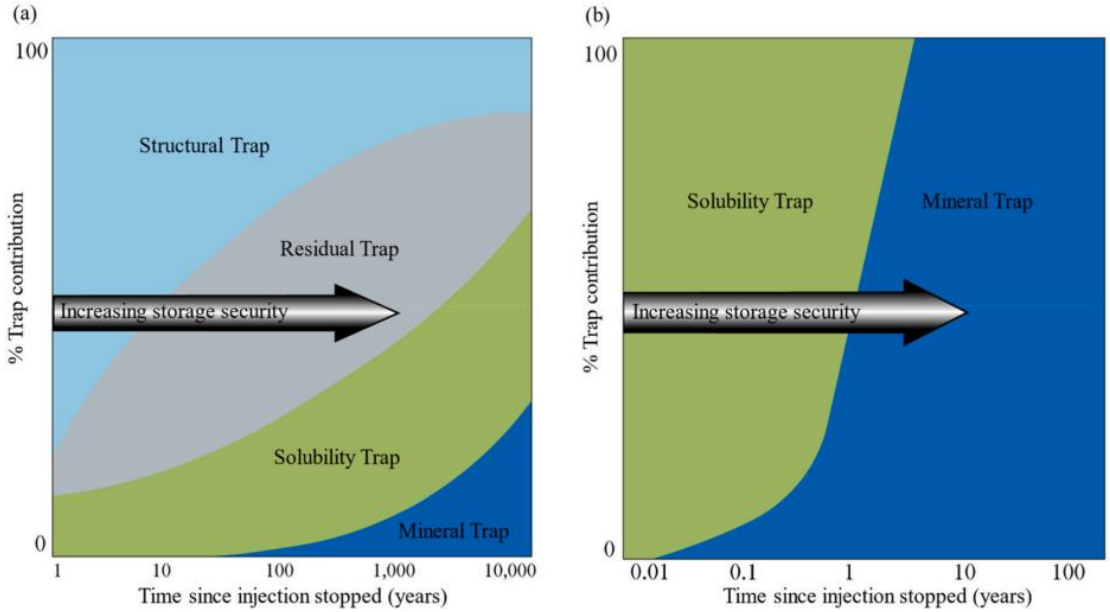

Figure 5. Contributions of various mechanisms of entrapment of CO_2 over time in: (a) sedimentary basins and (b) basalts (Kim et al, 2023).

This phenomenon was also seen at the Shenhua location as a complementary effort to mineral trapping over time, adding to the total stability of storage (Yang et al., 2020). The second type of trapping is solubility trapping, meaning that when CO_2 dissolves into brine, the more that dissolves, the less there is to create a separate phase that may be subjected to buoyant migration. Thus, this mechanism promotes stability, as CO_2 brine is much denser, leading to convective down-welling, or brine being carried deeper into geological formations and maintained there for longer. At the Sleipner site, for example, Johnson et al. (2004) were able to model this, and solubility trapping created low phase mobility over decadal scales.

Similarly, recent findings suggest that the topology of the caprock affects the efficacy of mineralization. For example, Punnam et al. (2022) studied reservoirs with two different profiles—an anticline and a horizontal cap—and found that the interaction of plumes and solubility sequestration differed significantly across structures due to different convergence and fingering patterns of flow. However, mineralization occurs over much longer timescales. Dissolved CO_2 can bond with silicate and carbonate formations to form stable, solid carbonates. This is the most effective in terms of long-term storage, although it's a relatively slow process. Liu et al. (2018) replicated a precipitation reaction in situ at the Ordos Basin and found drastic decreases in porosity as feldspar and other parent minerals changed over time, forming precipitated solids of calcite and magnesite. Yang et al. (2020) strengthen the potential for such a reaction to occur as areas that underwent mineralization also had lower flowability, which supports the efficacy of the caprock in an indirect way.

2.5. CO_2 Behavior in Geological Media

Visualization has become a popular approach to comprehend CO_2 sequestration. Visualization transforms the results of the models into manifest structures—3D models, cross-sectioned fields of concentration, isopressure planes, and saturated images over time—which permit qualitative consideration of such structures and quantitative considerations of migration phenomena and caprock pressures. For example, 3D renderings show vertical and lateral adjustments of CO_2 in a plume state, extending and navigating based on injection rates, heterogeneity of the formation, or due to greater structural restrictions. Osei (2024) demonstrates the pure vertical and lateral migration of a plume over time within a saline formation and subsequent evolution of caprock deformational stress in conjunction to compare findings. Such spatial renderings result in the greatest assessment of mineral precipitation, however, and permeability changes. For example, Yang et al. (2020) utilize visual conjunctions of regions filled with minerals, areas of CO_2 saturation, and related permeability to show how caprock integrity can be self-reinforced over time. This was also true with efforts from Punnam et al. (2022), relying on relative topographical diagrams with standard versus randomly curved caps to see how slight geometrical changes can have drastic effects over time with areas of solubility trapping. Other visualizations attempt to promote an understanding of ground deformation and stress propagation within shallow and surface-level efforts to assess the stress conditions within the injection zone. This offers a crucial understanding of the relationship between the operational performances of injection and geomechanical changes monitored or

established in situ moving forward (Seabra et al., 2024). While this is an effective way to ensure understanding as it builds off the empirical nature of subsequent monitoring efforts, it also fails at standardization and applicability across efforts. If generalized forms were to be utilized, the collections of data could be more easily assimilated across multidisciplinary efforts and additive for regulatory efforts—and potentially assist in educating general communities about safety and efficacy concerns for CO_2 storage.

2.6. CCS Site Selection

Geological site characteristics for geological carbon storage depend on how safe and suitable a geological formation is for carbon capture and sequestration (CCS). Characteristics of potential sites for carbon storage include capacity, injectivity, storage/retrieval/retention, and stability over time. The most studied geological formations that are most conducive to CCS include deep saline aquifers, depleted oil and gas reservoirs, and unmineable coal seams; each of these formations has the capability for retention of vast volumes of CO_2 under the proper temperature and pressure conditions (Tomić et al. 2018). The importance of the caprock formation reinforces this need. Competent caprocks serve as seals to prevent injected CO_2 from migrating back up. Typical geological features include confinement qualities for liquid/steam, qualities of porosity and permeability, and thickness of formation/injectivity success requirements.

Yet another consideration is geomechanical stability. The geological formations must be evaluated to see if they can withstand injection pressures without the creation of new fractures or reactivation of natural faults that would be exacerbated by increasing pressures and lead to CO_2 leakage. This is the case for formations close to more tectonically active areas. Thus, the risk assessment procedures involve not only hydrodynamic modeling but also fault stability assessments to combat over-pressurization and induced seismicity. For instance, brine extraction has been shown to successfully relieve non-injection induced over-pressurization (Solanke et al., 2024).

However, beyond geological feasibility, the site must be evaluated based on its ambient environment and logistics. For instance, proximity to CO_2 sources as well as transport and connections to other pipeline systems or industrial hubs provides economically advantageous options. Moreover, a site must allow for long-term evaluation via distributed acoustic sensing

and 4D seismic imaging to ensure that the injected CO_2 remains intact. Ultimately, various candidate sites are evaluated in a priority fashion via comprehensive screening matrices which assess technical, environmental, and permitting considerations for safety and efficacy before any CCS efforts take place (Celia, 2017).

2.7. Fault Reactivation

Fault reactivation refers to displacement along a fault that has existed. Generally, faults reactivate through stress alterations that render certain faults shifting from metastable to unstable. In the general sense, fault reactivation occurs from naturally occurring or anthropogenic conditions applying stress to a certain fault line. Fault reactivation is relative to in-situ stresses and fault direction, faulted rock's physical and mechanical properties, and pore-fluid pressure. Knowledge of reactivated faults can be of interest to geomechanics, fault and seismic stability, fluid flow within wells, and an indication of the larger rock mass integrity. This is of interest to occupied regions with hydraulic activities, including geothermal operations, fracking, wastewater injection, and CCS.

2.5.1 Fault Instability

The precipitating factor for predicting fault slip is the Coulomb failure criterion, which asserts that shearing occurs when the applied shear stress on a fault plane exceeds the frictional strength and cohesion of the fault (Figures 6-7). This threshold value relies on effective normal stress, which is decreased by increases in pore pressure. Therefore, faults are more likely to reactivate in faulting conditions—even without active tectonic loading—after being triggered by seismicity (Rutqvist, 2012).

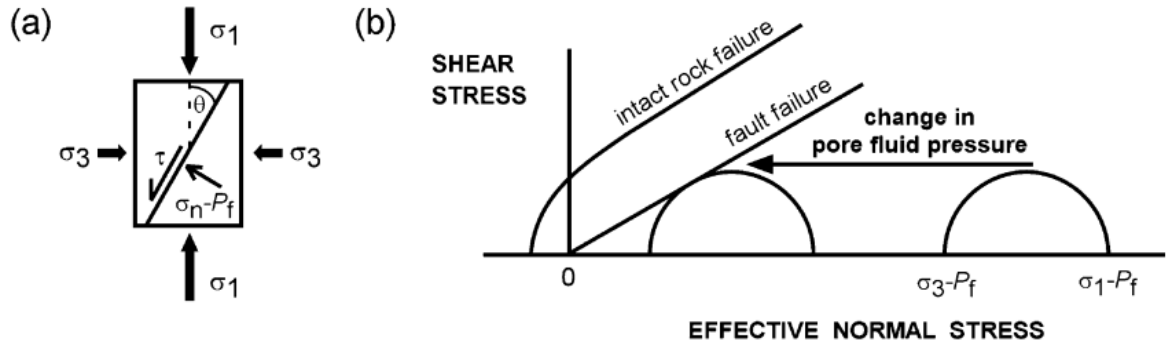

Figure 6. (a) Stress components acting on a fault; (b) Increased pore pressure impact on fault stability.

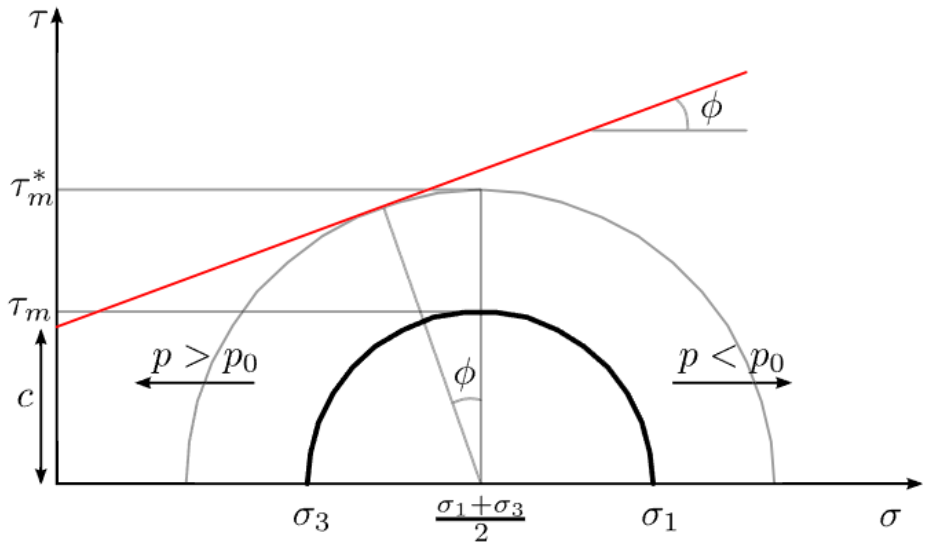

Figure 7. Mohr's circle of stress state present in a porous medium (Castelleto et al, 2012).

Wherever the fluid injected moves through the host rock and induces pore pressure increases away from the injection site, faults located kilometers from the injection wells are affected—assuming regional pressure increases sufficiently above this failure line. Cappa & Rutqvist, 2011, and Vilarrasa, 2016, reveal through coupled hydro-mechanical modeling that faulting occurs either through shear or tensile failure; increased pore pressure compounds stress redistributions at the faults such that previously established equilibrium conditions are disrupted. This occurs more often than not with shear failure occurring with the fault dip orientation and mechanical state determining the outcome. Thus, geothermal pressures find ways to escape—exiting from siltstone after induced capillary pressure or finding leakage from injection wells with worn siding (Figure 8). Faults are not straight evil planes; they are imperfect—damage zones and cores exist with high k and low k, with different mechanical strengths and orientations which promote different liability for reactivation. For example, the flaws of the fault orient stress concentrations but also obscure them, minimize critical slip displacement, or redirect fluid pathways. In addition, empirical field studies and laboratory-based simulations suggest that fault reactivation is more than just a mechanical process.

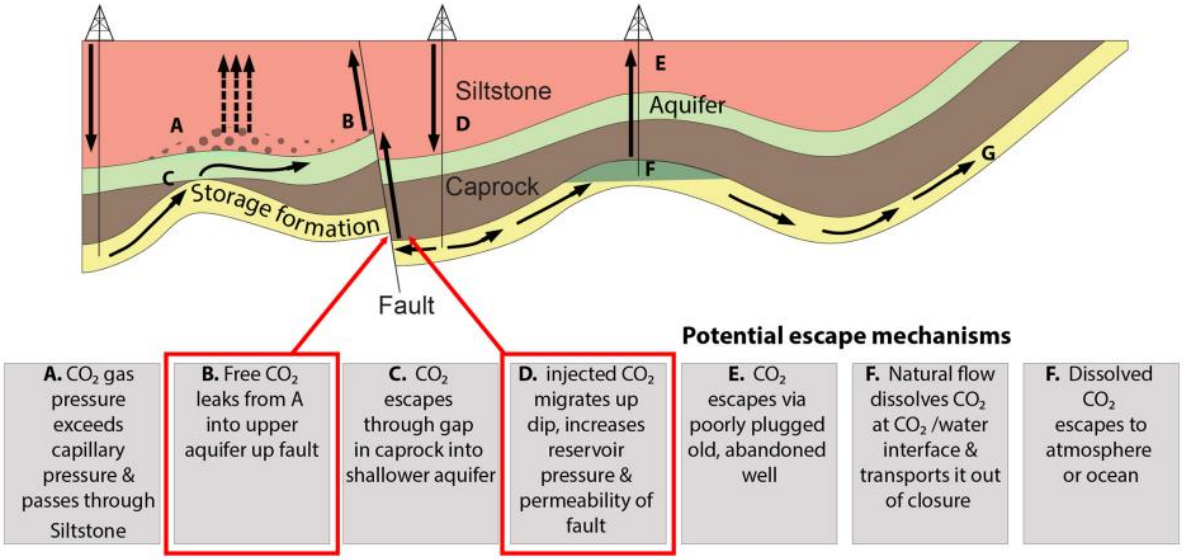

Figure 8. Potential leakage pathways for the injected CO_2 (Zappone et al., 2020)

Recently, fault reactivation has become increasingly clear through chemo-mechanical means where the presence of fluids—predominantly CO_2 or brines—interacts with the existing fault rock to weaken the fault matrix and fault gouge via mineral exchange. Although less frequent than mechanical forces, these forces exert weakening over time and, along with the potential for later reactivation in a probabilistic nature (Altaf et al., 2018), contribute to the process. However, to determine the inner workings of a fault reactivated from within, scientists must rely on seismological data, field structural geological studies, and numerical modeling. Currently, the vast majority of the information comes from numerical studies, as they can reproduce those exact levels of sub-fault stress and pressure in a controlled environment while testing reactivity—fault friction angle, cohesion/fault gouge dispersion rates, stress regime—sensitivities. So far, it has been found that faults activated near-critical stress levels are highly sensitive to slight pressure variations, which result in either seismic slip or aseismic slip of creation depending on local nucleation and response to conditions and properties (Silva et al., 2024; Rutqvist, 2012). Ultimately, the ability to model and find more field evidence supports the idea that fault reactivation occurs in a reactive manner. More assured than through a mechanical focus, faults are activated through hydro-thermo-mechanical and—now found interesting—chemical focuses; thus, a more concrete determination will come from fault-specific studies of architecture/stresses perpendicular to the fault plane and constitutive response of rocks under differing fluid/stress environments.

There are three fundamental types of seismic faults: normal, reverse, and strike-slip, based on movement and corresponding stress regime of the location where it exists.

2.5.2 Fault Types and Reactivation Mechanisms

Faults are often classified into three primary types: normal, reverse, and strike-slip, based on their relative movement and the regional stress regime (Figure 9).

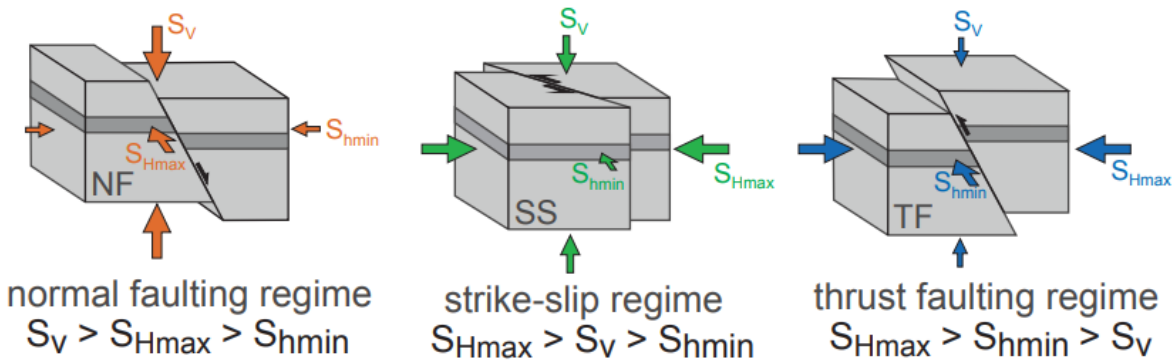

Figure 9. The major governing stress regimes (Heidbach et al, 2019)

The likelihood and mechanism of reactivation depend on orientation to major principal stress axes, stress state, and corresponding changes in pore pressures from natural or anthropogenic activities. Thus, the association of such faults and types of reactivation is critical to understanding stress perturbation for energy and environmental geotechnics. For example, normal faults are most common in extensional systems where the maximum principal stress is vertical (inverted). Normal faults are thus more likely to reactivate because of fluid injections where pore pressures achieve levels that reduce the effective normal stress across (or restored across) the fault plane (Figure 10). For example, modeling shows that normal faults aligned subvertical in extensional systems undergo shear failure due to increases in reservoir pressure during fluid injections (with specific fault reactivation attributed to high slip tendency orientation) (Cappa & Rutqvist, 2011). Similarly, normal faults undergo reactivity over subvertical orientations due to increasing pressures over time; nearly any increased pressure induces fault reactivity over subvertical faults which align with the principal stress orientation owing to enhanced systemic permeability attributed to reservoirs connected to other reservoirs; over time, extensive fluid injection can provide pressurization around such faults depending on fault permeability and interconnections with reservoirs over time. Reverse and strike-slip faults experience more reactivation potential, but at increased effective normal stresses due to

increased frictional resistances developed due to increased stresses developed at depth. Yet for deeper faults influenced by the thermal stress incrementality, collinear injection has a unique response. For example, when cooled fluids (such as that from CO_2) get injected into deep reservoirs, there exists a thermal-hydro-mechanical component. In deep sequestration, for example, this cooled temperature alters the in-situ temperature—from decreased temperature through depth in some cases. This stress change alters the Mohr-Coulomb failure envelope).

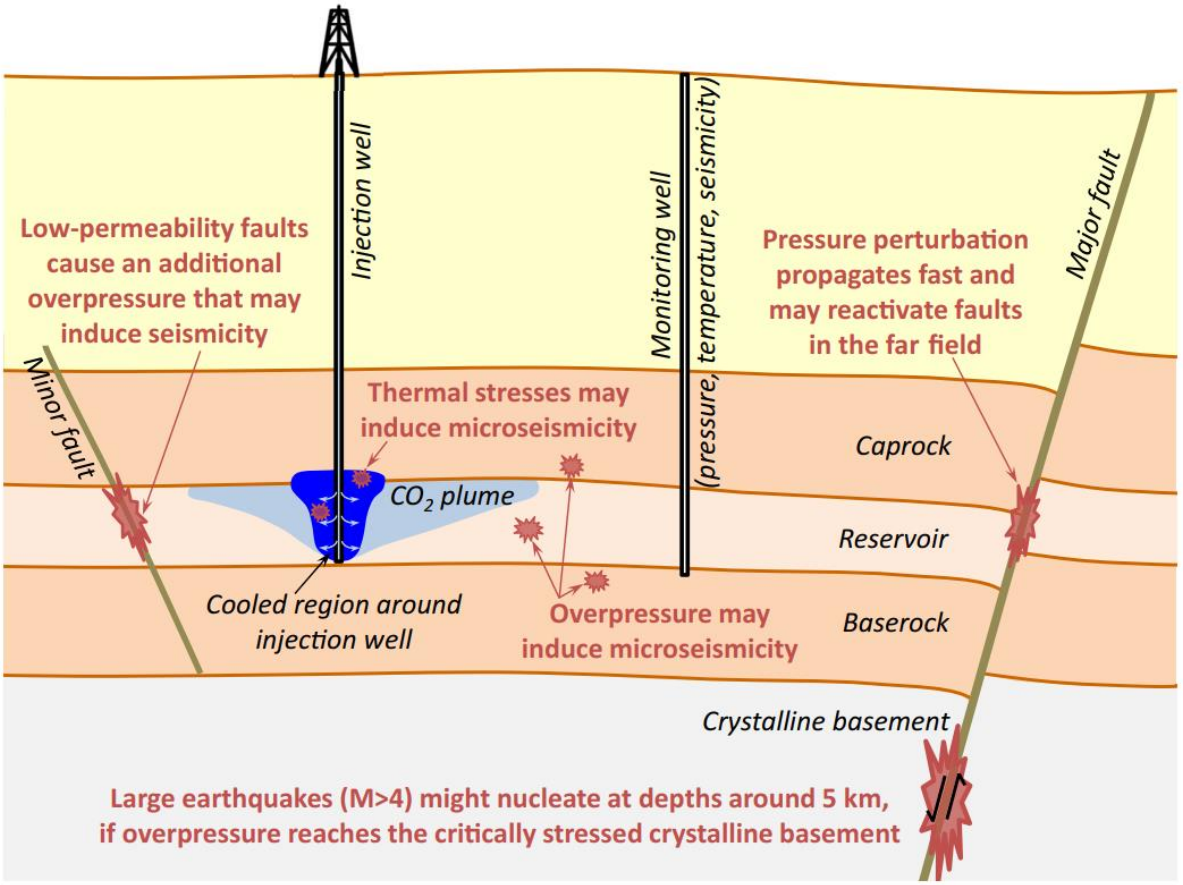

Figure 10. Potential origins of microseismicity and felt seismicity linked to geological storage of CO_2 (Vilarrasa, 2016).

Under a reverse or transpressional regime, the combination of stress redistribution with thermal effects increases the number of fault orientations at risk of destabilization. Faults are not uniform. Many are anisotropic with a fault core and surrounding damage zones with fractured, brecciated, and altered materials. These structural elements possess different permeabilities and strengths which impact pressure dissipation and mechanical properties. The presence of such attributes complicates the stress-strain response under injection. For example, Rinaldi et al. (2014) investigated the mechanics of multilayered sedimentary systems with complex fault features and found that internal heterogeneities in hydraulic and mechanical properties dictate how fluid pressures develop along the fault. Their

simulations suggest that mechanical heteroscedasticity focuses or dissipates stress which can cause low-magnitude earthquakes or, depending on caprock thickness and fluid interconnections with surface aquifers, vertical blowouts of CO_2. Impermeability of a fault zone is more effective than fault isolated permeability. In other instances, damage zones can be high-permeability highways while the fault core is a blow-up. This type of response is expected due to the anisotropic pressures associated with the fault zone architecture. Others have modeled buried faults with through caprock to aquifers and argue that the intensity of the permeability gradient and where it exists fault components determines effective stress evolution. These either cause faults to fail in shear or open or create preferential flow paths (Zappone et al., 2020; Wenning et al., 2020). For example, sustained injection can create a net increase in permeability as dilatancy or wear of fault minerals can over time create increasing flow leakage potential.

Another fault feature that assesses whether a fault will reactivate is fault geometry. Non-planar faults, step-overs, and branching faults exhibit complex loading responses that differ from those expected from planar faults. For example, a simulation that uses non-linear elements and multiphase flow characteristics shows that pressure and slip localization occurs not along the fault plane, but at connecting, high-permeability branches (Rohmer & Allanic, 2013; Cao et al., 2024). Moreover, the width and length where active changes in pressures occur also influence stress reconfiguration over distance and increase the likelihood of the extent of failure. Similarly, preexisting conditions factor in stress levels and how much incremental stress is necessary to cause fault slip. The notion of "critically stressed" faults suggests that many faults exist already at failure with present stress levels—meaning that only a slight perturbation is needed for slip to occur. For instance, at faults where CO_2 is injected, critically stressed faults, if oriented properly to the maximum horizontal stress, are likely to slip even with small changes to injection pressure (Silva et al., 2024). Thus, the compilation of information obtained from 3D fault mapping relative to the regional stress tensor orientation and assessments of strength should be factored into the probability of reactivation.

Recent studies exploring fault reactivation go beyond the realm of mechanical explanations to include chemical interactions. For instance, dissolved CO_2 can acidify reservoir brines, and resultant changes in fault gouge and host mineralogy. While such chemical changes can reduce effective frictional strength over time or develop induced porosity, the review by Altaf et al. (2018) notes that the chemical reactivity of such injected fluids has been assessed in mineral trapping. Yet relatively few studies assess whether the induced reactivity alters

mechanical properties—namely, cohesion or Young's modulus—of mineral interfaces. Yet with the increasing number of studies championing such changes, the findings might promote softening faults that seal over time, reducing slip resistance and thresholds for reactivation slips. In addition, not all fault stress changes due to injection are destabilizing; some studies show increased normal stress, from poroelasticity, can stabilize portions of the fault. For instance, Silva et al. (2024) note that depending on the orientation and depth of the fault, certain pore pressure increases can be negated by poroelastic changes in the opposite direction. Therefore, stress changes associated with CO_2 injection are both destabilizing and stabilizing; the subsurface geomechanical impacts occur in a conditionally diverse spatial context.

2.5.3 Fault Reactivation in the Context of Carbon Sequestration

Over the past twenty years, the motivation to evaluate such risk has been a widely researched topic through numerical simulation, field studies, and laboratory investigations. For example, Rutqvist (2012) presented a seminal paper suggesting that faults may be reactivated due to coupled hydro-mechanical processes associated with CO_2 injection. Since injection promotes increased pore fluid pressure, the effective stress associated with vertical stresses acting on faults is diminished, increasing the likelihood of failure for critically stressed faults. This conclusion was drawn from a modeling study associated with the In Salah project in Algeria, which detected a relationship between subvertical faults and surface uplift through InSAR. The principal investigators anticipated that the deformation trends via InSAR occurred as a result of fault reactivation along the preferred pathways of CO_2 migration. Therefore, faults need to be characterized beyond the zone of interest/zone of injection. Field observations support this claim from other efforts, including the Decatur project in Illinois. For example, Silva et al. (2024) discussed multiphase flow and geomechanical modeling results incorporating the regional stress field, fault geometry, and microseismicity.

2.6. Discrete Element Simulation and Its Applications

The Discrete Element Method (DEM) is a versatile set of numerical modeling techniques capable of replicating responses of material made up from separate particles or blocks, rendering this method the most appropriate for fragmented, granular, or non-continuous intact material. The Discrete Element Method originates from Cundall and Strack in 1979 and becomes synthesized into the geological/rock mechanics modeling arsenal due to its ability to simulate discontinuities and fracture-related occurrences across vast lengths and time scales.

Unlike continuum-based methods, particles are tracked with the elements representing inert material particles or blocks over time with mechanical interactions including, but not limited to: contact forces, displacements, and failures (Morris & Cleary, 2009). For mining applications and geological CO_2 sequestration/storage operations, the Discrete Element Method is a universal method to assess stress responses from strain under complicated mining and injection stresses. In addition, the Discrete Element Method is a standalone method and is utilized in conjunction with Finite Element Method (FEM), Computational Fluid Dynamics (CFD), and Discrete Fracture Network (DFN) modeling when large or coupled thermo-hydro-mechanical (THM) analyses are necessary (Bao et al., 2015; Elmo et al., 2010). As computer processing grows more powerful throughout our time with more complex programming, DEM will become increasingly important to assess stress response from fractured rocks during excavation efforts and under fluid injection/stresses in the overburden and caprock.

2.6.1 Theoretical Background of Distinct Element Modelling

At its core, the Discrete Element Method solves Newton's equations of motion for a network of particles or blocks where the means of interaction originates from force–displacement relationships. In terms of rock mechanics, the discrete elements are parallel to the granular materials and bonded clusters of particles that pin together to form the intact rock properties and the jointed, healed, or pre-failure loading regions. Contact models determine the response of elements at their interfaces, from simple frictional contacts to advanced bonds or cohesive laws that allow for tensile and shear failure. For example, in DEM, bonded-particle contact models are commonly used to allow for the simulation of crack start, growth, and merging (Bao et al., 2015; Ju et al., 2018). Yet the cracks can be further specialized with dedicated formulations, such as the Smooth Joint Model (SJM), which differentiates between naturally occurring fracture planes and analytically induced ones, allowing for more aggressive incremental interactions to occur for jointed rock masses undergoing fracturing from hydraulic stimulation (Fu et al., 2024).

Particles in DEM can also be polyhedral or clumped spheres to accommodate more irregular grain geometry and mesoscopic, non-homogeneous styles of deformation. Perhaps the most impactful feature of DEM is the ability of non-mechanical coupling with multiple physical phenomena. For example, coupling with fluid flow is necessarily predicated upon pore-scale or particle-scale applications of Darcy's law within the DEM, and for certain

applications, such as the bonded-DEM approach for carbon sequestration, hydraulic pressures are applied directly onto the particle mesh to determine how rock deformation occurs simultaneously with fluid dispersion (Bao et al., 2015). For these bonded-DEM experiments, stresses induced by fluid intrusion or changes in pore pressures result in fracture networks that can emerge and grow over time, altering reservoir permeability, which is critical for understanding not only the migration of CO_2 to the atmosphere but also its ability to be hydrofracked.

The problem with DEM, however, is that it is computation heavy. The elements and contact requirements compound very quickly, especially in 3D. One solution would be to only use it in places where fracture propagation would be applied and couple the boundary to a standard finite element method (FEM) domain which is less intensive and more attuned to the comprehensive geomechanical picture (Bao et al., 2015). Yet it could also be noted that such 3D applications are becoming more plausible with new parallel computing applications, such as General Purpose Graphics Processing Units (GPGPU) to spread the demand across nodes. For example, Takarada et al. (2024) use GPGPU for their extended finite-discrete element modeling of induced fracturing activities for mining operation scenarios. Their precision for such modeling is increased—along with using GPGPU—by data-driven parameterization. This means that their large-scale project evaluates fracturing at the particle level observed via micro-CT and examined with XRD to determine input values and calibrations indicative of rock texture and petrophysical properties (Peter-Borie et al., 2011). It seems plausible to use DEM in these projects; they are micro to start with but can grow to evaluate and understand macro mechanical behaviors. In geomechanics, it's critical that DEM understands the microstructure and larger scale mechanical response.

2.6.2 Practical Applications in Mining and Carbon Sequestration

Within the mining sector, the Discrete Element Method (DEM) is paramount in assessing and characterizing rock response characteristics to highly stressed, fracturing environments. One application that pertains to hydraulic preconditioning of fractured ore bodies is hydraulic fracturing. Such techniques are typically employed in cave mining to facilitate fragmentation and caving while decreasing seismic risks. For instance, hydraulic fracturing is studied by developing a lattice-based DEM to simulate fluid-injected fracture progression from stress fields generated by active cave voids (Fu et al., 2023). In this case, the

stress fields from continuum-based modeling are input into DEM elements to assess the most effective hydraulic fracturing. The researchers test various borehole points in relation to active caves and orientation to predict fracture growth and future development design, spacing, etc. Fracturing is vital to cave operations as stresses from subsequent mining may shift within fracture design, and understanding these shifts can facilitate cave continuity.

Regarding subsidence and draw control predictions during panel cave operations, a hybrid discrete fracture network (DFN) and finite/discrete element method (FEM/DEM) assess the relationship between naturally formed and mining-induced fractures during draw (Elmo et al., 2010). This provides insight into how the nature of existing fractures and faults exhibit asymmetric response behaviors with subsidence, which can help inform draw control activities. Similarly, DEM is incorporated with fractured carbon sequestration techniques. For instance, the activation of fractures and associated permeability post-CO_2 injection are assessed via DEM. For example, coupled DEM-FEM studies assess the failure zones around injection wells and inform fault reactivation potential due to stress and thermal fluctuations (Bao et al., 2015). Furthermore, 2D DEM studies regarding CO_2 injection and resulting microseismic events were sensitive to the temperature of the storage site and fracture permeability, attributing findings to the multi-phase flow of CO_2 and thermal stresses on caprock integrity (Reyes-Montes et al., 2011). Using a similar approach, albeit a lower-dimensional discrete fracture model, the damage to fracture surface is studied to assess the post-CO_2 injection fluid transport (Tomac et al., 2015). This determines how stress induced by fluid action causes microcracking around existing fractures which increases porosity and results as preferential pathways—important for the long-term viability of CO_2 containment. Additionally, some thermally induced mechanical stresses are assessed via thermomechanical experiments. For example, Peter-Borie et al. (2011) apply particulate DEM to assess the mechanical changes from thermal events after CO_2 injection to determine how thermal contraction of the host rock would induce ore fracture opening. Thus, these applications highlight real-world uses of DEM to simulate fracturing systems where conditions are more unique compared to non-fractured systems in mining or geological environments—important for assessing how fracturing evolves or how integrity is assessed during long-term efforts of CO_2 storage.

3. METHODOLOGY

Novel methodologies include a coupled mechanical-fluid flow solution with three-dimensional distinct element modeling. Discrete element modeling (DEM) used for geomechanical assessment of fault reactivation in underground CO_2 reservoirs provides critical information about fault systems relative to stress redistribution due to fluid injection/expansion. DEM is utilized because it assesses the geomechanical properties of the rocks, as it represents the discontinuous rock formations. Therefore, it can evaluate the mechanics of faults and subsequent stress redistributions, fault slip, and second-order fractures formed from CO_2 expansion. Through an accurate representation of fault reactivation, it provides critical assessments of fault zone permeability and stability under increasing pore pressure. For open and closed shifting faults, reactivation may occur; however, assessing the geomechanics of the process is critical in understanding the potential for induced seismicity and leakage during CO_2 sequestration.

The uncoupled solution analyzes how fluid pressure changes without any regard to the mechanical response and behavior of the reservoir. This is a more basic, less accurate measurement of the full system response because fluid movement does not happen on its own and increased pressure will have stress distribution effects throughout the reservoir. In addition, the sensitivity analysis derives from the coupled solution with critical reservoir parameters changed. The host rock property components, in-situ stresses (horizontal to vertical stress component), fault plane orientation, and fault fluid properties are assessed from the final results. Therefore, this coupled solution promotes a thorough analysis of the system's mechanical and hydro-mechanical response to CO_2 injection.

3.1. In Salah CO_2 Storage Site

This study aims to explore fault activation mechanisms in relation to the in-situ scale. Therefore, a number of global CO_2 storage sites were evaluated. Of the sites evaluated, the In Salah site in Algeria was found to be one of the most well documented and actively monitored storage sites. Thus, the site's overall geology, confining boundary conditions, geomechanical/rheological host rock architectural data, geological impressions, history of overpressurization, and post-injection monitoring were assessed and accepted as a pathway for numerical analysis performed.

3.1.1. Geomechanical Behavior at In Salah

The In Salah CO_2 storage project in Algeria is one of the most studied locations of CO_2 storage within a low-permeability, fractured sandstone reservoir (Figure 11). Operational between 2004 and 2011, it greatly contributes to current literature on geomechanical hazards, fractures, and faults reactivation from deep injections into saline aquifers. The driving force behind the study was the assessment of the stress field relative to fracture reactivation and caprock stability, addressing potential changes to an in situ stress field owing to pressure from injection combined with pressure increases from geomechanics. For example, by determining the coupling flows early on, researchers could understand leakage potential through changes to pore pressure in the principal stress field created by diffusion of pressure in the injection zone. The initiation of in situ effective stress assessment showed that CO_2 injection could decrease effective normal stress acting on subvertical fractures, allowing for more tensile and shear fractures and associated failure. Thus, pressure was of interest at compartmentalized areas where localized pressure increases would be expected.

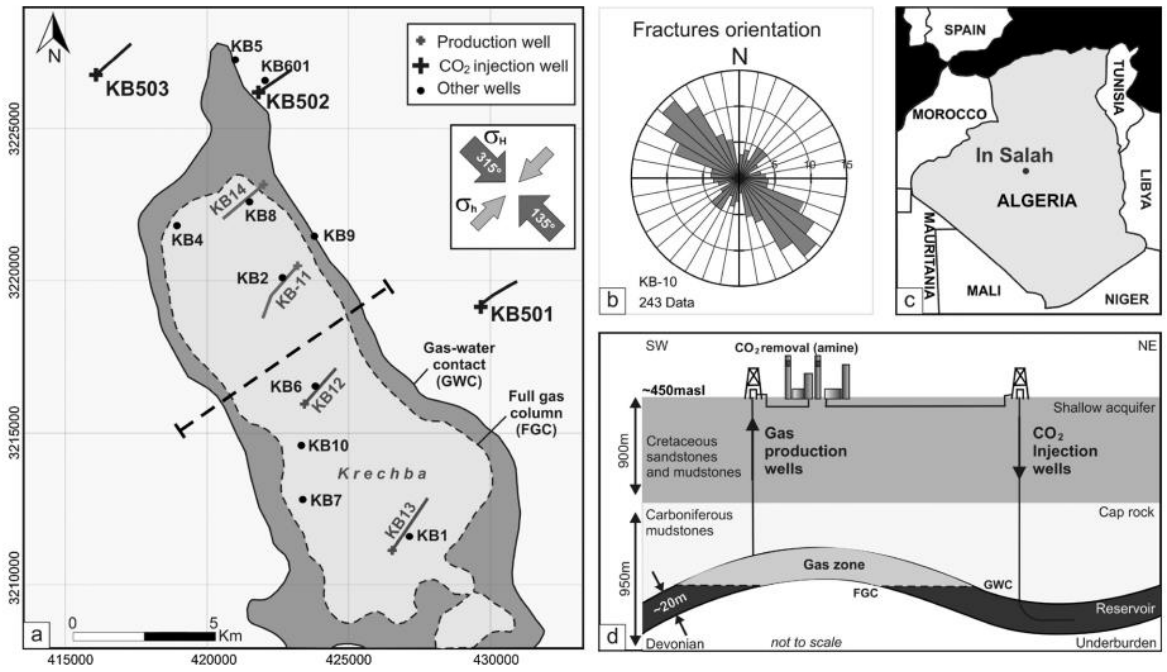

Figure 11. The In Salah CO_2 sequestration project: (a, c) Location map of injection and production wells, (b) Rose diagram of natural fractures observed in well KB10, (d) Injection horizon structure (Bjørnarå, 2018)

An additional study replicated the short-term response to these stress changes—vertical deformation, for instance, and the evolution of the damage zone width—largely about and in the well injector KB-502 (Rinaldi & Rutqvist, 2013). By accounting for poroelastic effects and

permeability increases due to deformation, it was found that the stress-induced elevation was related to changes of stress induced inside and outside the fracture zones intersecting well injection pathways. A more comprehensive assessment of these mechanical interactions comes from Whites et al. (2014) assessment, who assessed the major mechanical stress interaction between the overburden and the lower/caprock units and the injection reservoir. They found that while pressure and possibly CO_2 migrated upwards into the lower caprock, the overlying main sealing units remained mostly unaffected. Whereas mechanical buffering from caprock's layered internal structure helped maintain stored integrity where injection pressures increased, the subsequent information showed pressures moving up; the lesson learned was the necessity of assessing vertical seal integrity under chemical and mechanical pressures.

Furthering the investigation into the integrity of the caprock is the alignment of thermal disturbances concerning caprock integrity. That is, the injected CO_2 is usually colder than the surrounding formation, which creates a thermal gradient where the rock contracts near the wellbore, changing stress states. Vilarrasa et al. (2015) provided a thermo-poroelastic sensitivity analysis to assess stress changes due to temperature gradient within the Krechba caprock. They revealed that Krechba cooling reduced confining stress in Krechba caprock, primarily in the depths, which could render pre-existing fractures reactive in shear (although tensile failure is still unlikely). The model revealed that even though the uppermost parts of the seal, 900 m depth, had mechanically induced stress stability, the lower regions did not; thus, findings confirmed that stability assessments should consider pore pressure and temperature effects as well.

Most recently, a more in-depth study of fault slip potential through mechanistic fault slip simulations permitted the assessment of fault reactivation potential under a higher resolution. Although the studies used varying modeling assumptions and input variables, there seems to be a general agreement that fracture reactivation at In Salah occurs due to localized stress changes from compartmentalized pressure changes, faulted geometry, and thermal-mechanical coupling. However, most believe that the seal has not been breached to any significant extent, especially due to the multi-level nature of the caprock system (White et al., 2014; Vilarrasa et al., 2015). This set of geomechanical studies highlights the necessity of in situ research and obtaining as much useful geomechanical and geological data as possible (Figure 12).

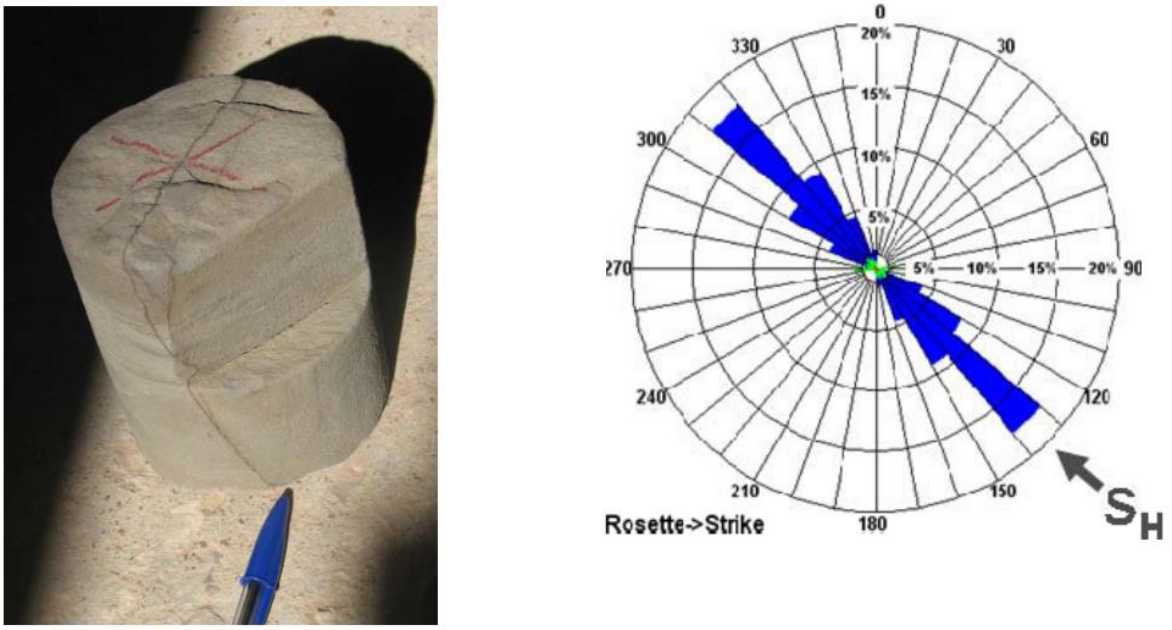

Figure 12. Fracture studies: (left) Mineralized fracture from well KB-2 core, (right) Fracture azimuth from FMI image log in well KB-502 (Iding & Ringrose, 2009)

3.1.2 Monitoring Techniques and CO_2 Migration Patterns

Key monitoring techniques contributed to understanding CO_2 behavior in situ at In Salah, including linking surface displacement to subsurface pressure changes and fracture development. One of the critical monitoring techniques was InSAR, which produced high-resolution temporal and spatial data relative to surface displacement. Thus, the fact that InSAR could capture such slight hypocenter pressures through uplift was critical to combining it with geomechanical and hydrological models to better understand the changes occurring below the surface. For example, Rucci et al. (2011) generated multicomponent SAR datasets from ascending and descending satellite passes that allowed researchers to differentiate between the uplifts noted in vertical versus horizontal displacement. Over time and at super specific locations around KB-502, a matched analysis over time produced a two-lobed pattern of surface uplift that could not be explained by a radial expansion model of the reservoir (Figure 13). Instead, this fracture pattern indicated the activation of subvertical damage zones traversing the lateral extent of injector wells.

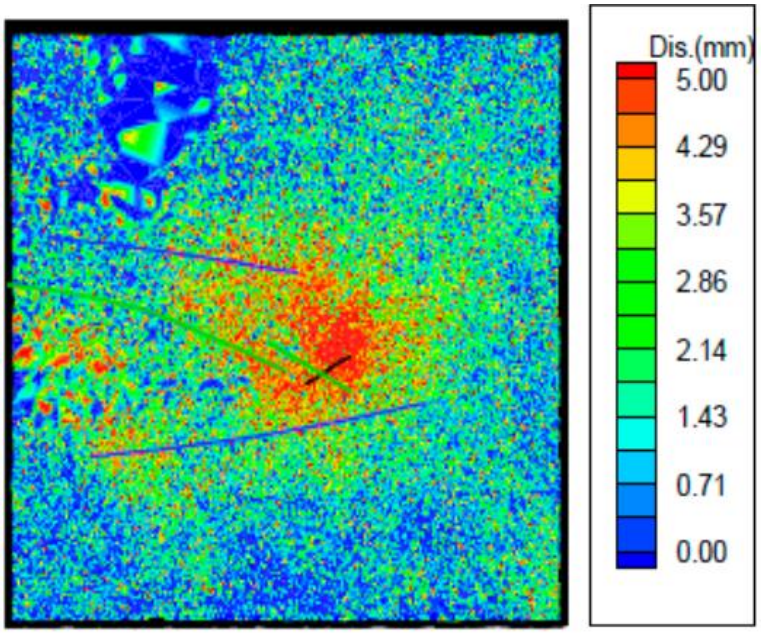

Figure 13. InSAR surface deformation above the KB-502 well after one year of injection (Morris et al., 2011).

The uplift occurred because of pressure changes over the same lengths as well, similar to the distributed aperture changes along those fractures seen in the numerical simulations, supported by the predicted direction of fracture migration and the coupling with mechanical displacement of the fractured formation. Rinaldi et al. (2014) conducted a similar numerical inverse analysis to correlate the InSAR deformation that they observed with cumulative pressures associated with injection (see Figure 14) for the KB-501, KB-502, and KB-503. They wanted to demonstrate that preferred flow paths exist in orientations (and correlate with the current stress field), where during pressure excursions incremental stress related to fracturing opened and expanded within its associated stress fields forming horizontal and vertical flow conduits over time. For example, pressure migration estimates over the temporal deformation suggested pressure moved from the well location over time to further out, supporting the need for modified transmissibility values in their dual-porosity reservoir model. Their modified transmissibility values allowed for a better correlation of the historical bottom hole pressure indicators with their observed and modeled responses in time suggesting an understanding of pressure history is better understood with the notion of reservoir deformation. There were also time lags in which surface deformation occurred subsequent to the pump ins. For example, Bohloli et al. (2013) found through their InSAR data that at the surface, uplift was not evident until months later but had occurred, accumulating 15–20 mm in vertical displacement by the end of effort in 2011.

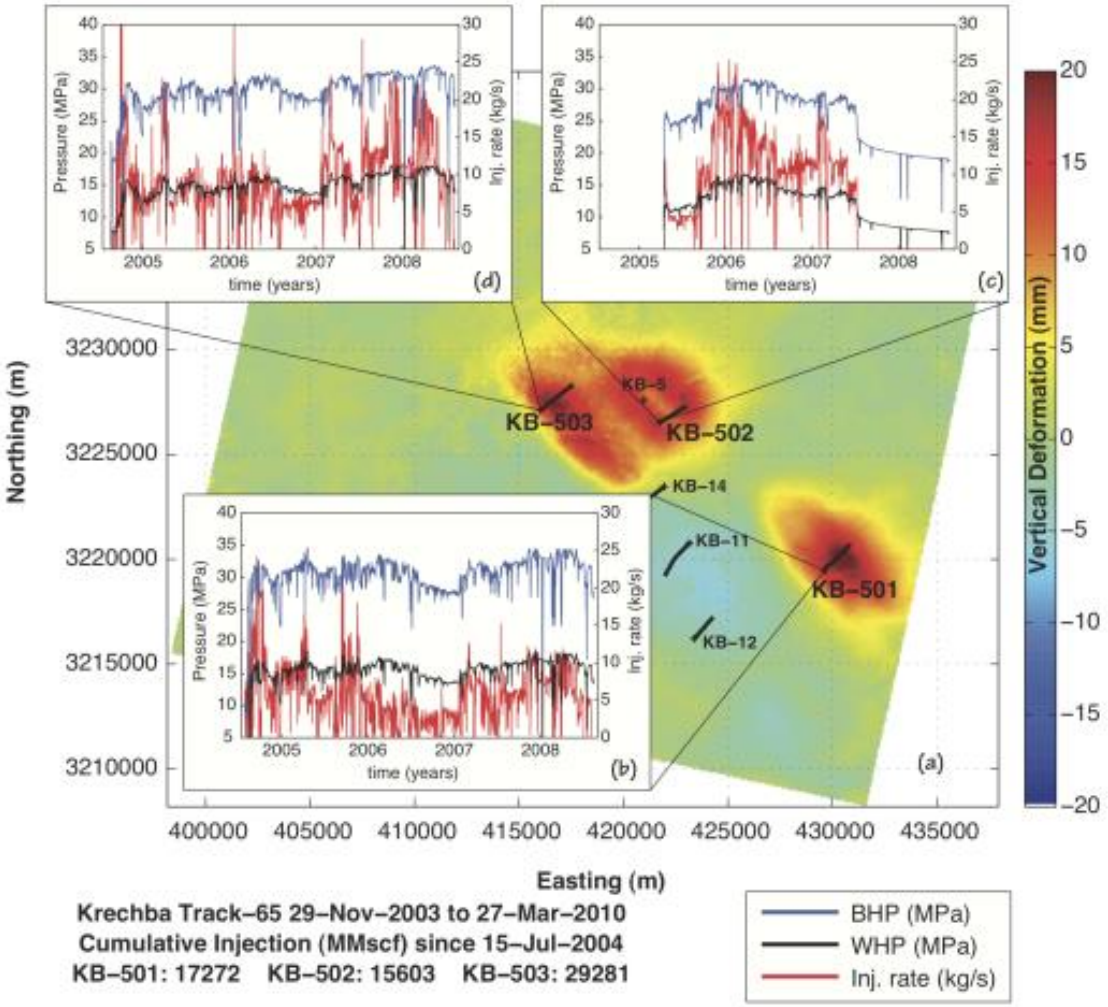

Figure 14. InSAR and injection data at In Salah. (a) Uplift measured by InSAR from Nov. 2003 to Mar. 2010 (b,c,d) Measured injection rate (red line) and wellhead pressure (black line), and calculated bottom-hole pressure (blue line) at the three injection wells (Rinaldi et al, 2014)

Places of displacement maxima were frequently found directly above the injection site, while certain places were even subject to uplift in locations of low injection or where injections were turned off temporarily. The fact that these places were displaced, however, once injection stopped, suggests a delay. So one explanation for these delays is a poroelastic time delay between sub-surface pressure changes and resultant surface deformation. This, in turn, implies that InSAR efforts need to be ongoing to assess what's going on in the reservoir from above. While satellites can provide information to assess plume activity, seismic characterization helped assess the CO_2 plume itself and the internal reservoir structure. For example, Zhang et al. (2015) used poststack seismic attribute analysis—curvature and ant-tracking—to show that linear features existed that matched the characteristics of the fracture networks. In turn, these seismic features aligned with the zones of InSAR displacement, suggesting that fractures used

to transport CO_2 for injection caused uplift and subsidence were the same fractures engaged. In addition, they used seismic inversion techniques to identify regions of impedance change due to saturation of CO_2 within the reservoir, facilitating a better assessment of the plume boundaries.

Yet another plume study tried by Ringrose et al. (2008) intersected well data with production telemetry and ground deformation, noting a more extensive radial extent for CO_2 around KB-502. Such intersection allowed the authors to confine the plume geometry and evaluate trapping effectiveness in addition to determining which parts of the reservoir were hydraulically connected due to fractured networks. Therefore, anecdotal evidence in advance showed that In Salah migration was in line with the paths taken perpendicular/parallel to regional heterogeneities, with trapping due to arrangements of capillary pressures, solubility, and spatial incidents over fault lines. More elaborate intersections/integration occurred via history-matching. For example, Shi et al. (2019) assessed stress-dependent permeability as coupled flow models, history-matching with InSAR and pressure responses. They determined that effective permeability responds to excited pressures, which is a vital factor for predicting stress reorientation and pressure response through time in low-permeability reservoirs like Krechba. Ultimately, observational evidence and theoretical modeling confirm that various factors dictate the plume migration process: complexity of faulting patterns, anisotropic permeability, fracture networking, and shifting transmissibility. Satellite interferometry, geochemistry, and geophysical explorations successfully established a historical reservoir picture through real-time assessments of plume activity and simultaneous reservoir confirmation. To combine multiple reservoirs into one theory as successful in In Salah suggests the merit of such techniques applied elsewhere for similar monitoring of geographically diverse projects with limited geological understanding.

3.2 Discrete Element Modelling Framework

3.2.1 Numerical Operations

To conduct coupled flow-deformation analysis, a proper configuration is required in 3DEC's environment to allow for proper interaction. 3DEC allows for coupled flow-mechanical response via empirical and physically based methods. Fractures and their surrounding porous rock matrix allow for fluid flow. This subsection covers the theoretical aspects and implementation numerically of such coupling, which involves stresses and

apertures, matrix permeability, conservation of mass and flow continuity, and fluid-mechanical coupling.

3.2.1.1 Aperture-Stress Coupling and Joint Flow Mechanics

Fluid flow in fractured rock occurs as a function of joint/discontinuity interaction. In 3DEC, joints are defined, and the mechanical/hydraulic behavior of the joint is interdependent. For example, a joint flow property is hydraulic aperture, which signifies the effective diameter of the area through which flow occurs. The hydraulic aperture u_h is defined as:

$$u_h = u_{h0} + \Delta u_n \quad (1)$$

where u_{h0} is the aperture under zero normal stress, and Δu_n is the current mechanical displacement across the joint. The displacement term is positive for opening and negative for closure. Thus, this real-time adjustment of aperture allows for stress-dependent permeability to be rendered. Yet the model also enforces a minimum aperture whereby unrealistic values of zero or negative apertures are avoided to ensure some effective permeability exists even under confining stresses that are high (Itasca Consulting Group, 2023a). The influence of stress on aperture is captured through the concept of effective normal stress. In 3DEC, this is calculated as:

$$\sigma_n' = \sigma_n + p \quad (2)$$

where σ_n is the total normal stress acting on the joint and p is the fluid pressure. The connection between stress and aperture is relayed through effective normal stress. An effective stress factor of one occurs, meaning that pore fluid pressure counteracts normal stress entirely. Thus, when pore fluid pressure is higher, effective stress is lower, meaning that joints open further. This is an important trigger for how permeability can change over time due to injection, increased fault interaction, or pore pressure build-up. Once the hydraulic aperture is determined, joint permeability is obtained from the cubic law:

$$k_j = \frac{u_h^2}{12} \quad (3)$$

This formula applies to laminar flow between two smooth, parallel plates, essentially nonlinear, meaning flow within a joint is highly responsive to variation between apertures. An

increase in hydraulic aperture produces a disproportionate increase in permeability, so 3DEC can compensate for rapid changes in fluid transmissivity during mechanical processes like slip or dilation. This is significant for applications related to CO_2 injection, stress and stimulation of the reservoir, and even induced seismicity. Joints can be simulated via shear behavior, normal stiffness, and dilation. Therefore, 3DEC can accommodate such mechanical characteristics in addition to the fluid flow formulas to create hydro-mechanical interactions in a discrete discontinuity network. The fluid of the joint can change as the joints change, and the hydraulic conductivity can be updated per time step.

3.2.1.2 Flow Continuity in the Matrix and Darcy Flow Representation

Beyond joint flow, 3DEC is capable of simulating fluid flow within the intact rock matrix as well. When the mesh command matrixflow is invoked, the matrix acts as if it were a porous medium. This means that the matrix permeability and matrix storage affect the calculation, although this enhancement is more applicable to dual-porosity flow systems or pressure dissipation over low-permeable blocks. The fluid continuity equation in the matrix is expressed as:

$$\frac{\partial}{\partial t}\left(\varphi\rho_f\right) + \nabla * \ \rho_f v = Q \tag{4}$$

Here, φ is porosity, ρ_f is fluid density, v is Darcy velocity, and Q is a source/sink term. The transient term indicates storage of pressure in the matrix, and the divergence term indicates flow into or out of a control volume. In this way, pore pressure can dissipate, deplete, or recharge during the calculation. The fluid velocity v is governed by Darcy's law:

$$v = \ -\frac{k_m}{\mu}\nabla p \tag{5}$$

where k_m is the matrix permeability, μ is the dynamic viscosity of the fluid, and ∇p is the pressure gradient. This link is established with the assumption that an isotropic, saturated state occurs. Thus, by using Darcy's law to translate the relationship between physical rock properties to flow properties, the code can facilitate a more natural interaction between the pressure field and rock deformation afterwards. Where, in reality, joint permeability is many

orders of magnitude greater than matrix permeability, this is a relationship more likely to be bonded further on in the procedure down the line; over extended timescales or if the joint network is clogged from closure. Furthermore, matrix flow allows for the potential of leak-off to be assessed, which is necessary for injection situations and temporally changing pressures

.

3.2.1.3 Numerical Coupling of Flow and Mechanical Processes

The benefit of 3DEC is that it couples fluid flow and mechanical deformation in a fully interactive fashion. For instance, through the effective stress concept, the same mechanical and hydraulic solvers allow for coupling. When the mechanical model's nodes are grid points, these become the flow nodes of the fluid model. Therefore, all pathways are solved at the same discretized level—fluid or solid. Stresses, fluid pressures, and displacements occur at the same joint locations. The mechanical solver solves for displacements, stresses, and joint (interaction) deformations by solving its mechanical equilibrium equation through an explicit finite difference method; simultaneously, the flow model, via a finite volume method, solves for fluid pressures at the same joint nodes. They are coupled because pore pressure changes effective stress:

$$\sigma' = \sigma - \alpha p \tag{6}$$

In 3DEC, the Biot coefficient α is generally equal to 1.0 because it believes that fluid pressure is entirely mechanical. When pore pressure rises, effective stress is reduced, and mechanical responses occur like joint slippage or yielding of the matrix. The same is true for mechanical yielding that alters the volume of pore spaces, which changes fluid pressures and fluid velocities accordingly. The solver is fully coupled, meaning that mechanical and flow solving occurs within the same time step. Thus, one can create conditions that rely on iterative feedback, like pressure-determined failures and temporal changes in permeability.

3.2.1.4 Joint-Matrix Interaction and Leak-Off Mechanisms

An important aspect of 3DEC's fully coupled flow condition is the ability to simulate fluid exchange between the joints and the rock matrix. This is known as leak-off, as the fluid can move from a relatively high permeability fracture into a lower permeability matrix. The volumetric flow rate per unit area between a joint and matrix is calculated as:

$$q = C(p_j - p_m) \quad (6)$$

where q is the flux, C is the conductance coefficient, p_j is the pressure in the joint, and p_m is the pressure in the matrix. This equation allows for dynamic, two-way fluid movement based on pressure differences. When injecting, for example, the pressure in the joint may be greater than in the matrix, allowing fluid to leave the joint and go into the matrix. However, when the pressures are decreased, fluid may re-enter the fracture from the matrix. The matrix conductance term is a function of the joint-matrix interaction geometry and attributes; therefore, this is user-defined. This interaction is critical to simulating pressure wave attenuation properly, as leak-off during high-pressure injection is what mitigates uncontrollable pressure propagation and mechanical response. 3DEC's ability to couple joints and matrices provides for the ideal simulation for immediate hydraulic response in the fracture and long-term stabilization during pressure propagation through the matrix. Similar to a dual-porosity system, natural occurrences or man-made solutions have adopted, fractures allow rapid movement in response while the matrix, although slower, carries more significance over time for success. For instance, pressure will still be generated after consistent injection has stopped as the matrix will still be drawing in fluid. Such adjustments for stabilization need to be factored into understanding potential fracture closure, re-activation, or long-term viability of a caprock during storage efforts.

3.2.2 Modelling Strategy and Assumptions

A 3D simulation domain was established over 3 km by 2 km, extending 2 km below the ground surface. An injection well was simulated approximately 1800 m below ground, horizontally, within the C10.2 sandstone layer, measuring 20 m thick. The primary CO_2 storage reservoir is located approximately 1800 m below ground, measuring approximately 20 to 25 m thick. It is a Carboniferous Tournasian sandstone unit, with multiple formations below and above. Above the reservoir is a significant sandstone and siltstone layer with approximately equal thickness. The lowermost caprock is the sealing layer, positioned between 1550 and 1800 m, composed of silty shale, which has fractures preventing upward migration of the CO_2. The primary caprock is a Carboniferous Visean mudstone, which has a siltstone layer and a thin dolomite layer interbedded, allowing a secondary sealing capability. The primary caprock is

overlain by a Hercynian unconformity approximately 20 m thick. The overburden above the primary caprock is understood from significant formations. The uppermost level is a Cretaceous Continental Intercalaire, a 730 m unconsolidated sand and from 170 m to 900 m, a Pan-Saharan aquifer. From 170 m to ground level, the Cretaceous Supérieur exists, mainly limestone and silt. These geometries create the system and containment capacity for the storage site. Figure 15 shows the base model framework and sensitivity analyses conducted.

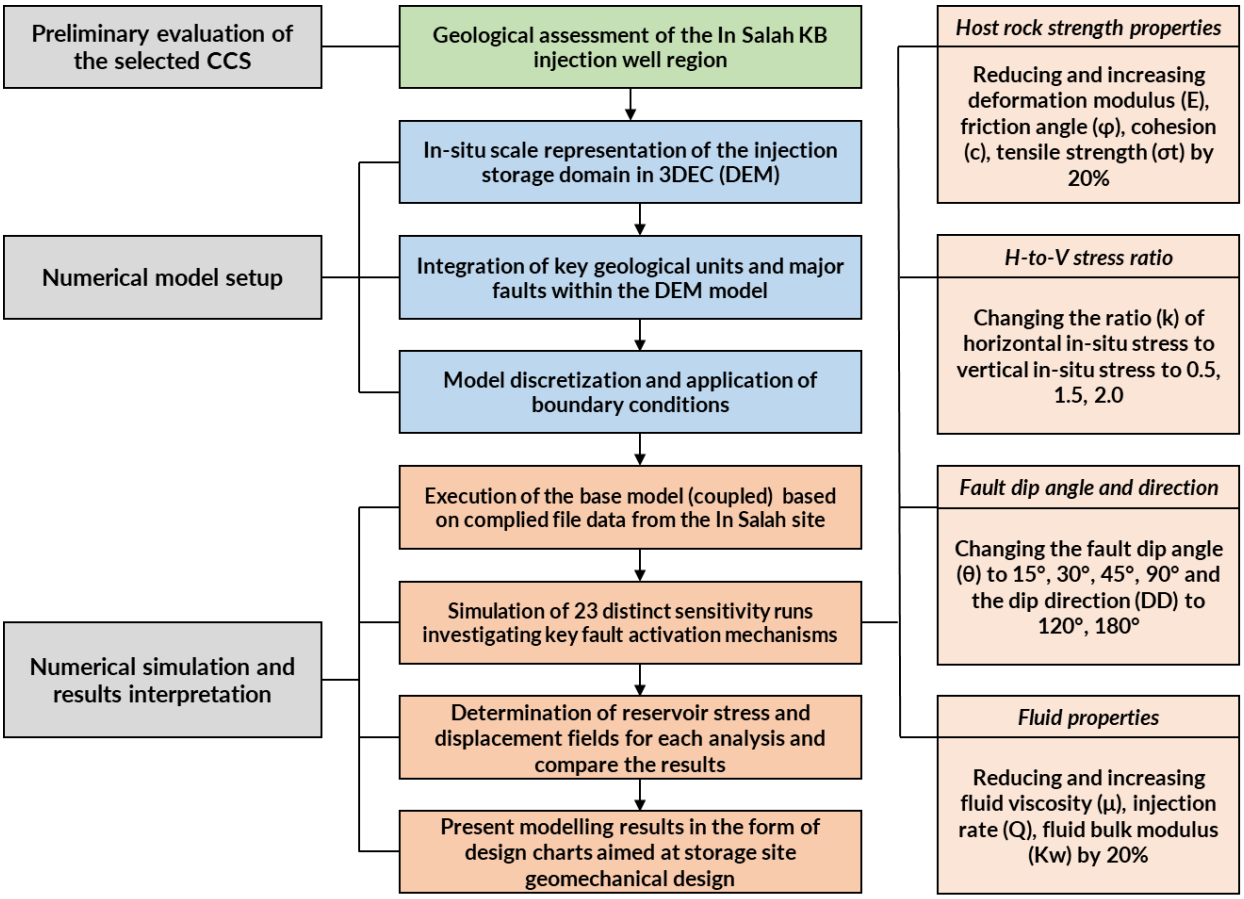

Figure 15. Numerical simulation strategy

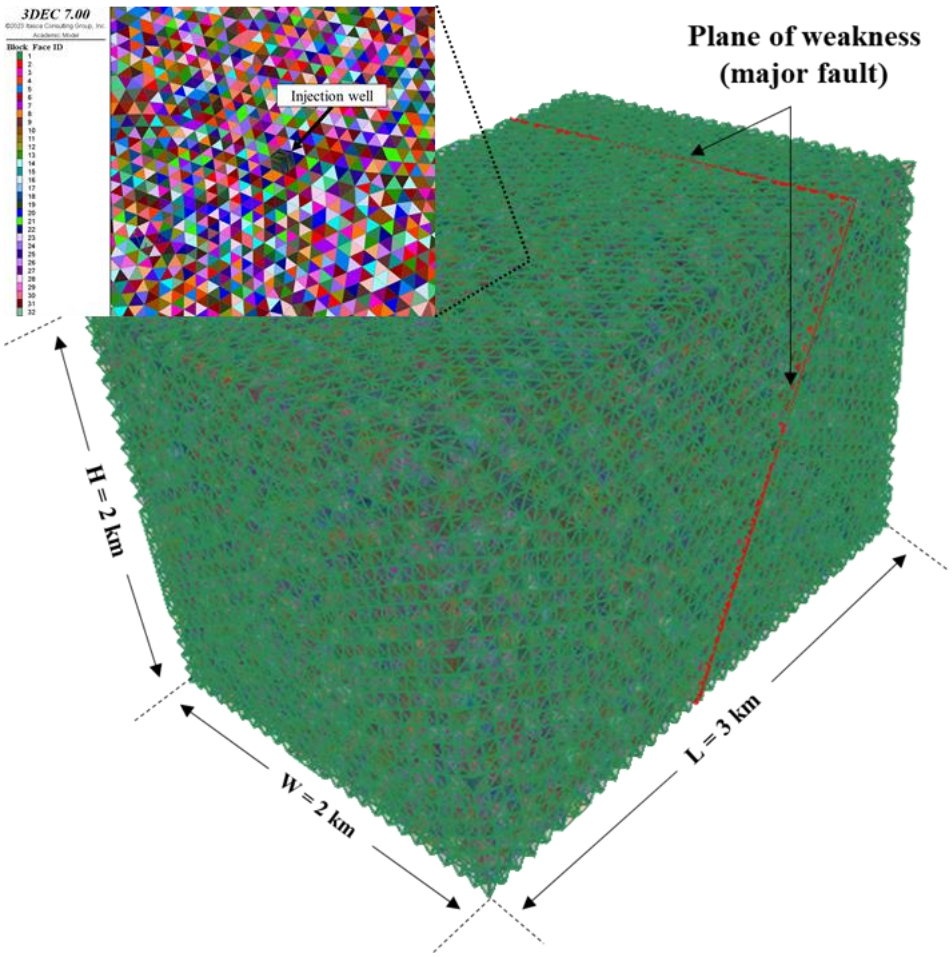

Figure 16. The 3D model implemented in 3DEC

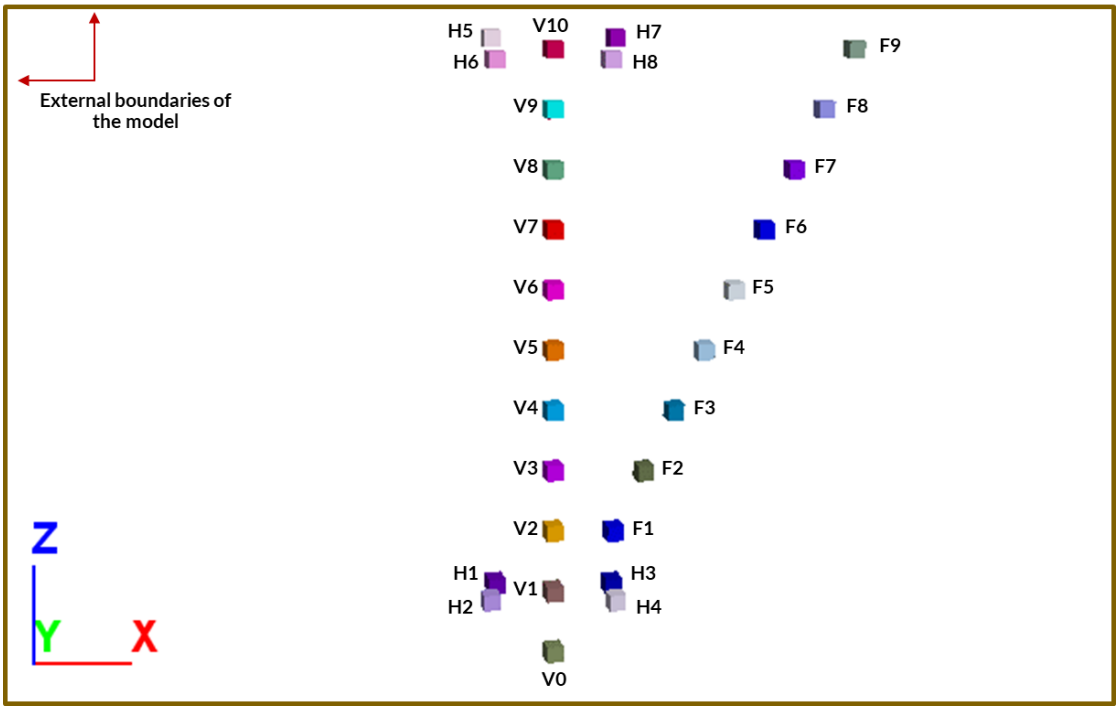

Figure 17. Monitoring points selected for the analysis: V – points along the vertical section, F – points along the fault plane, and H – points at the horizontal plane (XY) of the model.

A 3D reconstructed model of the storage site location was created from the anticipated regional geology. A snapshot of the generated model can be found in Figure 16, including the injection well (KB-502) and the major fault. The points of interest's locations and orientations are found in Figure 17. The points of interest are numbered according to their distinction. For example, the points are numbered according to their location since some are located on the vertical axis of the model (V0-V10), on the fault plane (F1-F9), or on the horizontal (XZ) plane of the model (H1-H8).

3.2.3 Boundary Conditions

Then, in order to create a stress regime that mirrors that of the reservoir, a numerical simulation is applied with the following stress boundary conditions: $\sigma H = \sigma y = \sigma 1 = 80$ MPa; $\sigma V = \sigma Z = \sigma 2 = 80$ MPa; $\sigma h = \sigma X = \sigma 3 = 80$ MPa. The condition bound to the model is displacement boundary conditions in which fixed (0 velocity) are applied to the exterior boundaries of the model, and all boundaries of the model are assumed to be permeable. In Figure 18, one can see the displacement boundary conditions applied to the model and the rotation of the fault respectively.

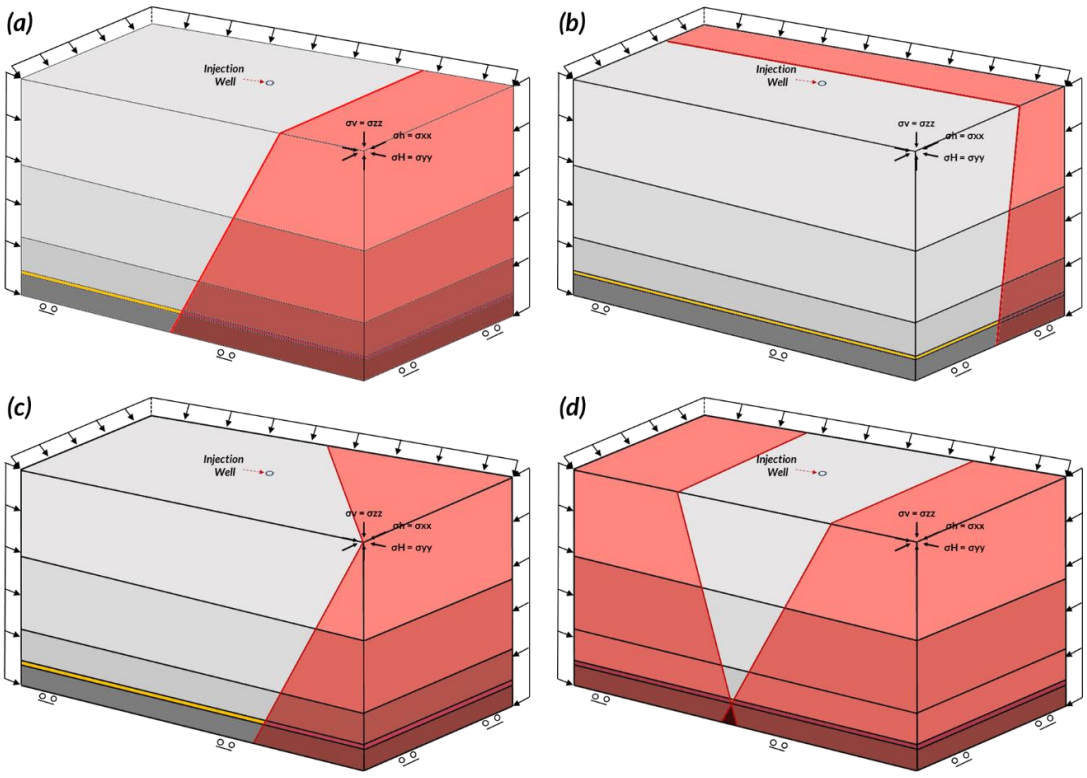

Figure 18. Fault orientation changes implemented in the numerical model: a) One fault dipping at Θfault = 15°, DD = 270°, b) One fault dipping at Θfault = 60°, DD = 180°, c) One fault dipping at Θfault = 60°, DD = 120°, d) Double fault: (1) Fault 1: Θfault = 60°,

3.2.4 Geomechanical Parameters

Table 1. Geomechanical input parameters used for the numerical simulation

Layers	Overburden	Main Caprock	Lower Caprock	Reservoir	Underburden
Lithologies	Cretaceous sandstones and mudstones	Carboniferous mudstones	Silty shale	Carboniferous Sandstone (C10.2)	Mudstone (D70)
Depth Range (m)	0-900	900-1550	1550-1800	1800-1820	1820-2000
Young's Modulus (GPa)	1.5	20	20	6	20
Poisson's ratio	0.20	0.15	0.15	0.20	0.15
Friction angle (deg)	22	30	37	25	35
Cohesion (MPa)	1.5	5	8	3	10.5
Tensile strength (MPa)	0.8	1.2	1.5	1.2	1.5
Effective Porosity	0.10	0.01	0.01	0.17	0.01
Permeability (m^2)	$1x10^{-17}$	$1x10^{-21}$	$1x10^{-19}$	$1x10^{-14}$	$1x10^{-19}$

3.2.5 Operational Parameters

To replicate the injection process, a constant injection rate of 5.0 l/s was applied at the center of the wellbore. The injection rate is adopted from In Salah charts and past studies. The operational parameters employed in the simulation are included in Table 2.

Table 2. Key operational parameters used in numerical simulation.

Property	**Magnitude**
J-set normal stiffness (GPA/m)	300
J-set shear stiffness (GPA/m)	110
Fluid viscosity (cP)	1.0
Fluid density (kg/m^3)	1000
Injection rate (l/s)	5.0
Fluid bulk modulus (MPa)	180

3.3 Sensitivity Analysis

A full sensitivity analysis was conducted to determine the primary mechanism of fault activation and caprock failure during CO_2 injection and post-injection. Dominant boundary conditions were established, and geo-mechanical and geo-physical parameters were evaluated for their impact on fault activation probability and displacement field of the injection location. Ultimately, four groups of parameters were chosen for the sensitivity analysis—they are as

follows: reservoir caprock strength, horizontal to vertical in-situ stress ratio, faulting dip angle, and fluid properties. Parameter adjustments of ±20% of the base run value were done to assess the relevant output in a control environment. Twenty-two unique runs were completed, and results were compared to each other. Each sensitivity run had only one variable adjusted while the remainder of the parameters were kept consistent. The summary of the sensitivity analysis is seen in Table 3.

Table 3. Details of the conducted parametric study.

Analysis Groups	Run no.	Parameter subject to manipulation
Base Analysis	1	Base parameters
Analysis Group A: The effect of host rock strength	2	Reduction of friction angle (ϕ) by 20%
	3	Reduction of cohesion (c) by 20%
	4	Reduction of tensile strength (σ_t) by 20%
	5	Increase of host rock friction angle (ϕ) by 20%
	6	Increase of host rock cohesion (c) by 20%
	7	Increase of host rock tensile strength (σ_t) by 20%
Analysis Group B: The effect of in-situ stress ratio	8	In-situ horizontal stress to vertical stress ratio k = 0.5
	9	In-situ horizontal stress to vertical stress ratio k = 1.5
	10	In-situ horizontal stress to vertical stress ratio k = 2.0
	11	In-situ horizontal stress to vertical stress ratio k = 2.5
Analysis Group C: The effect of fault orientation	12	Fault dip angle Θ_{fault} = 15°, dip direction (DD) = 270°
	13	Fault dip angle Θ_{fault} = 45°, dip direction (DD) = 270°
	14	Fault dip angle Θ_{fault} = 90°, dip direction (DD) = 270°
	15	Fault dip angle Θ_{fault} = 60°, dip direction (DD) = 225°
	16	Fault dip angle Θ_{fault} = 60°, dip direction (DD) = 180°
	17	Double fault: (1) Θ_{fault} = 60° and DD = 90° and (2) Θ_{fault} = 60° and DD = 270°
Analysis Group D: The effect of flow parameters	18	Reduction of fluid viscosity (μ) by 20%
	19	Reduction of injection rate (Q) by 20%
	20	Reduction of fluid bulk modulus (K_w) by 20%

	21	Increase of fluid viscosity (μ) by 20%
	22	Increase of injection rate (Q) by 20%
	23	Increase of fluid bulk modulus (K_w) by 20%

3.4 Phase I Numerical Analysis

3.4.1 Two-Dimensional Finite Element Modelling

Our contribution to the investigation of CO_2 storage seal integrity was a two-dimensional finite element modeling experiment to assess the geomechanical behavior of the faulted storage formations. Using RS2—an established finite element modeling code—we generated a model of the In Salah storage location in Algeria to assess the potential for fault reactivation based upon fault orientation, stress ratio, and pressurization (Mortazavi & Maratov, 2023). The geometry includes all relevant lithological units of the overburden and reservoir—overburden, primary caprock, secondary/lower caprock, and underburden—with a geometry of 4 km by 2 km. The estimated physical properties of the caprock and reservoir came from well logs and previous investigations in situ, which permitted logical assumptions of geomechanical response based on subsurface stress below the reservoir. The reservoir was excavated in the simulation to create a preexisting layer of the CO_2 reservoir (Figure 19).

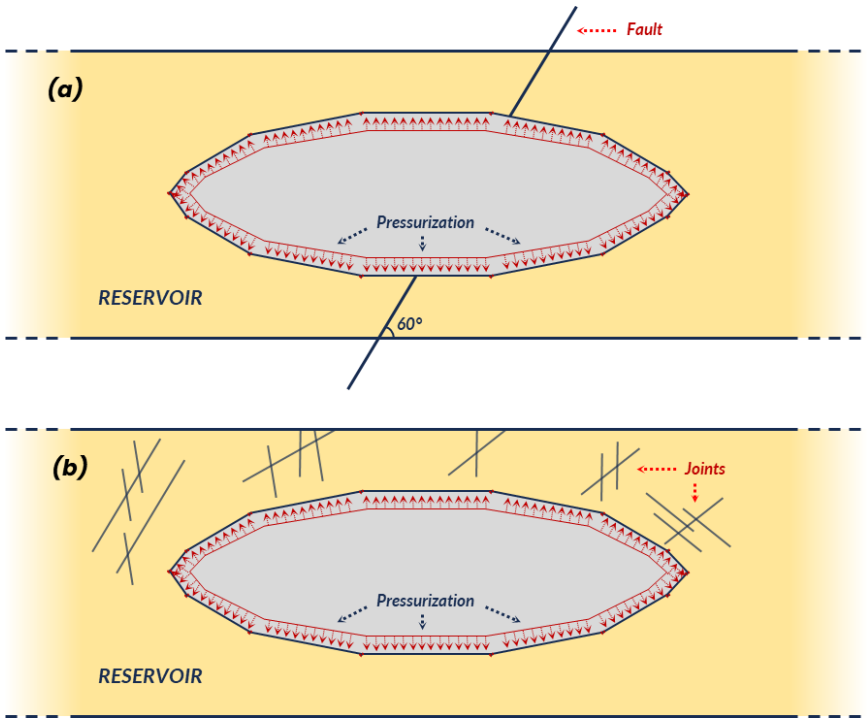

Figure 19. Representation of reservoir pressurization and fault zone structure using 2D FEM in (a) homogeneous and (b) heterogeneous jointed media.

The benchmark experiment we performed applied a base pressure of 32 MPa, and pressurization cycles increased beyond this magnitude, the displacements intensified proportionally (Figure 20). For the base analysis, the input conditions created a maximum vertical displacement of the caprock of 0.044 meters and ground surface heave of 0.015–0.020 meters (Figure 21). These are similar to the deformation trends captured by InSAR at KB-502; therefore, the model's applicability is correct. The final findings of the sensitivity analysis determined that the fault dip angle and the horizontal-to-vertical stress ratio influenced the resultant displacement field. First, with a fault dip angle of 30°, the increase in surface deformation signifies that more shallow faults are prone to reactivation compared to deeper faults. In addition, with a stress ratio of 0.5, where horizontal stresses confine vertical stresses, deformation decreases; therefore, confining effective in situ stresses reduce faults slipping.

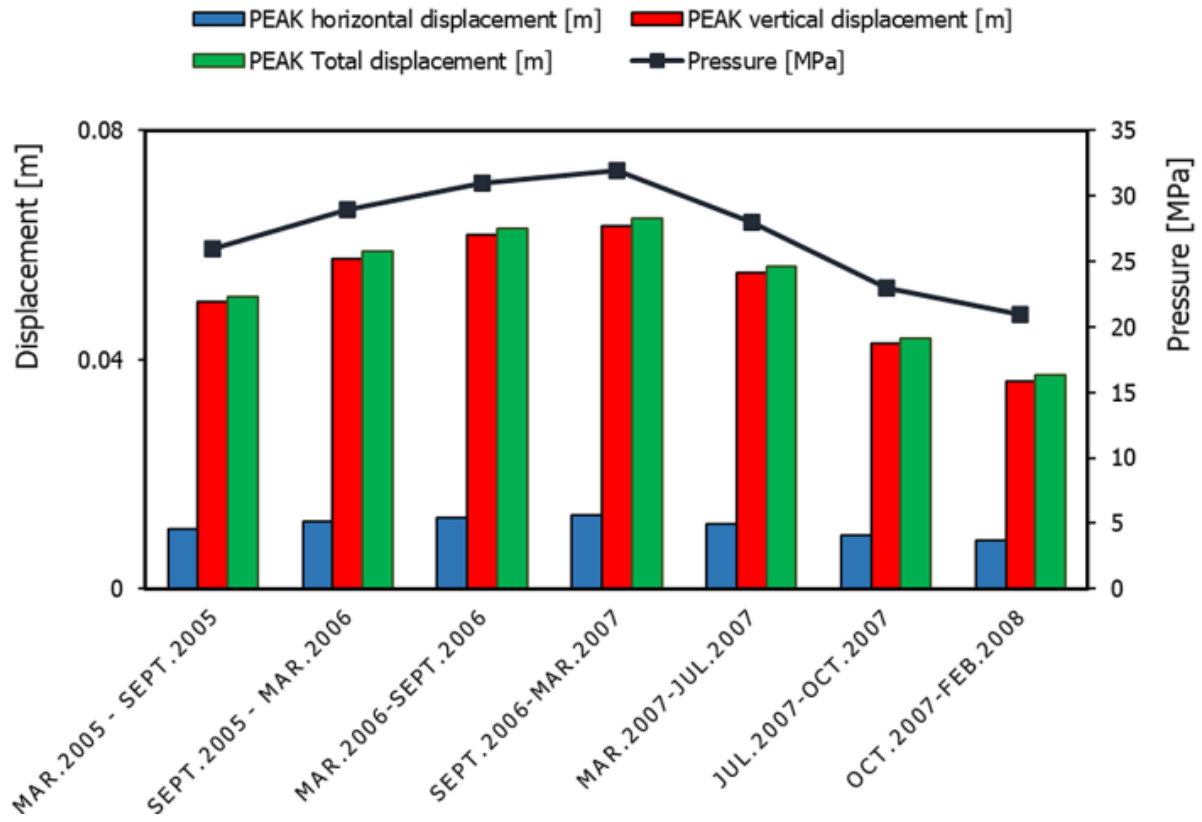

Figure 20. History of simulated peak displacement magnitudes at monitoring points 11−20 correlated with the pressurization cycle.

2D FEM works well in a vacuum, unobserved, but not everything is that simple in the world. 3D stress orientations and location, strike-slip and dip slip distributions, fault segmentation, and lateral heterogeneity are all omitted but are critical for a fault FEM.

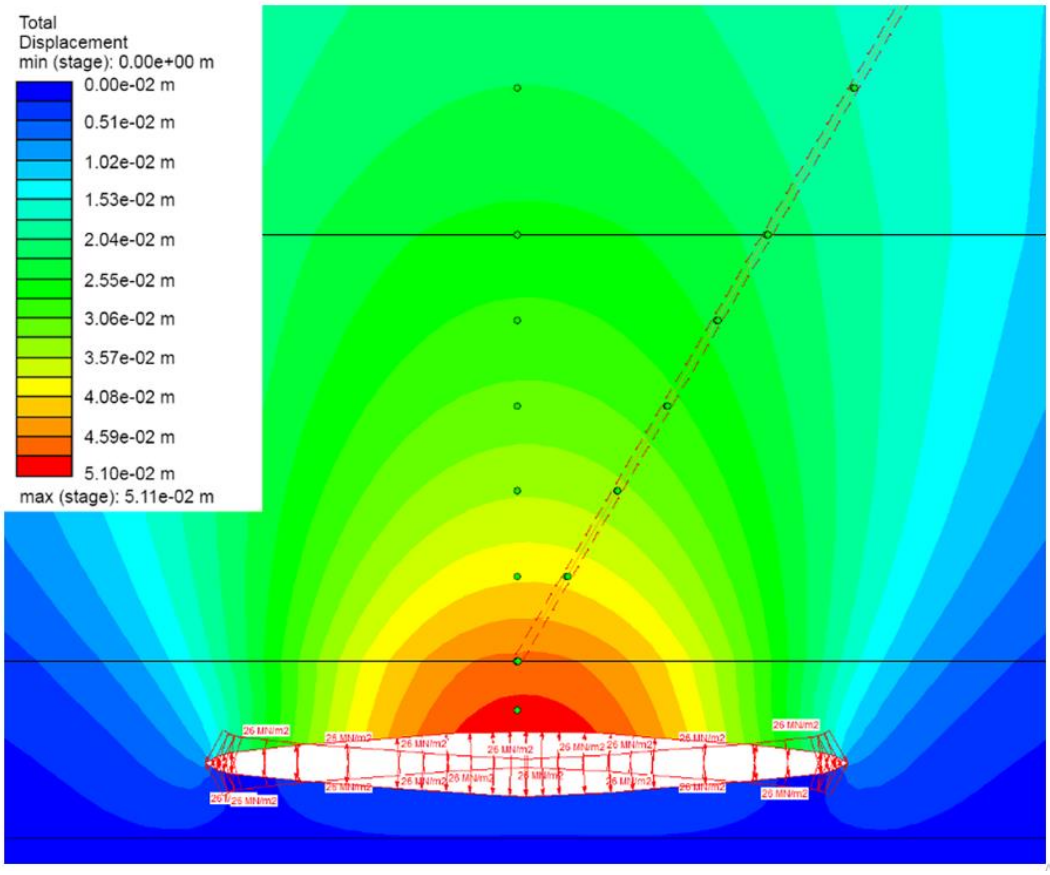

Figure 21. Geomechanical response of the model to the initial pressurization (26 MPa) of the reservoir.

Applying a continuum behavior ignores the realities of what's going on across fault zone mechanics—shear dilation, joint slip, fracture network evolution, etc. Yet compelling concerns exist with the geomechanical input data that are accessible. While the tensile strength is nearly unknown, the time-dependent attributes and fault cohesion could highly tune the friction states to increase predictive accuracy.

3.5. Phase II Numerical Analysis

3.5.1 Distinct Element Modelling

Once the 2D limitations were surpassed, a 3-dimensional numerical model was developed using the Distinct Element Method (DEM) within 3DEC (Mortazavi & Maratov, 2024). 3DEC is capable of assessing the blocky, discrete nature of fractured media behaviors and gives the capability to assess deformational fields that are not limited to a plane-strain situation. Thus, a 3 km × 2 km × 1.7 km block was created with a position of the CO_2 plume located within the caprock at a realistic pressure field of 32 MPa—this is similar to the

maximum bottom-hole pressures collected in the field. The findings of the 3D model determined that the maximum vertical displacement occurred at the reservoir—caprock overlay of 0.052 meters, while at ground surface, the uplift was determined to be 0.011 meters (Figure 22).

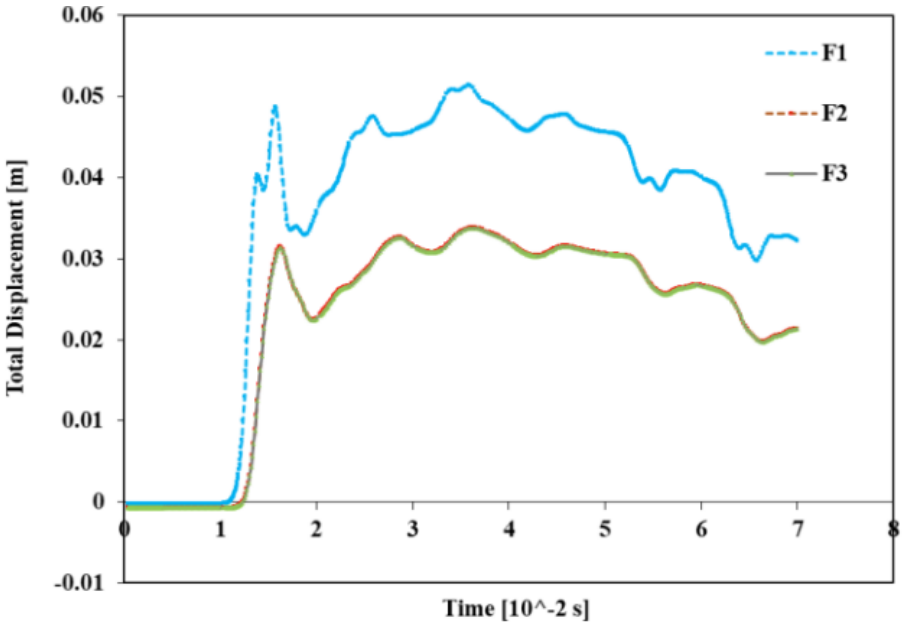

Figure 22. Total displacement magnitudes along the fault history points (F1 – closest to the reservoir, F3 – farthest from the reservoir / closest to the model boundary; distance between the points = 100 m)

Ultimately, the results confirmed the caprock's containment capacity under a base-case loading scenario, and the 3D simulation allowed for a spatial understanding of where stress occurred beyond just a magnitude value, as the fault was stressed and displaced in the orientation of a 60° dipping fault with increased stress and displacement at the contact with the reservoir. Although it, too, did not fully reactivate, the use of a 3D model allowed for physical experimental evidence beyond the 2D. However, despite the benefits of 3D modeling, there are also increased computational loads with less parametric accessibility. We could not test a wide variation of scenarios or even fully engage multiphase flow due to convergence requirements needed for iteration completion. Additionally, there was no direct coupling of fluid pressure change to rock deformation, which limited us from assessing poroelastic or shear-dilation effects over time. Furthermore, absent the ability to dynamically simulate fault rupture, this model does not speak to natural and induced seismicity for regulatory determination for long-term CO_2 storage sites. Thus, each model validated the other conceptually through different analyses, but each had limitations the other did not possess. Therefore, future works should

assess 3D coupled hydro-mechanical models against real-world fault characteristics to assess the safety of CO_2 injections and fault behavior more fully.

Table 4. Summary of the recent research attempts and major differences in the approach to the numerical simulation.

Studies / Attributes	2D FEM (Mortazavi & Maratov, 2023)	2D FEM Expanded (Mortazavi & Maratov, 2023)	3D DEM (Mortazavi & Maratov, 2024)	3D DEM Expanded (Master's Thesis, 2025)
Type of Analysis	Mechanical	Mechanical	Mechanical	Coupled Flow-Mechanical
Sensitivity Analysis	Minimal	Advanced	Minimal	Advanced
Software	RS2	RS2	3DEC	3DEC

3.6 Limitations of the Study

Yet despite such significant breakthroughs throughout the course of investigation, we encountered critical limitations as well that impacted both the findings and the subsequent discussion. For example, although our model was designed to create a more true-to-life stress distribution and deformation response and stress-related fault slip during fluid injection in a carbon sequestration environment, we were slightly constrained in the evaluation by overly simplified assumptions and computational trade-offs that unfortunately rendered the study quality less than ideal overall. The following are the challenges and observed limitations of the employed method:

- The most challenging aspect was the practicality of fully coupled 3D runs at the reservoir scale. Given the very detailed fault geometry, stratigraphy, and pressure gradient, the extended running time would allow practically no sensitivity analyses or geomechanical scenarios to be applied. Thus, the applied parametric changes had to be reduced to faulting and its subsequent stresses and permeability contrasts and orientations based on stress regimes, even though these were known to affect fault stability. Material behavior calibration required a material in a vertical lithological orientation over several layers; applying this in a 3D fashion rendered uncertainty for

the calibration of mechanical responses within heterogeneous fault zones.

- However, our shortcomings went beyond merely gathering and implementing data; for instance, we utilized a linear elastic Mohr-Coulomb failure criteria, which does not exist in a vacuum of all constitutive responses. Creep, stress relaxation, and strain hardening/softening greatly depend upon what type of injection pressures occur over time, and although 3DEC allows this to be entered, we did not have the means to calculate such active pressures over time. While 3DEC allows users to enter discontinuities explicitly, we still had a challenge adjusting for fractures that evolved over time or did not have a rupture process that could be studied via dynamics.
- Ultimately, we determined that while 3D coupled simulation allowed for a better visual representation of fault activity in space, it does not fulfill the requirements for accurate assessment since it hinges on too many assumptions, numerical issues, and fluid-mechanical couplings that fail to communicate. Fluid-flow coupling with the solid data must be validated in addition to constitutive responses with both simulated and real-world applications.

4. RESULTS

4.1. Numerical Simulation Results

The numerical simulation of the base case scenario with the above input parameters shows that the fault plane significantly affects geomechanical response. The cut plane to the front of the model (vertical plane) shows a total displacement distribution from 1×10^{-4} m to 1.38×10^{-3} m. The rainbow gradient represents the fault's spatially distributed total displacement to emphasize the fault's mechanical response from CO_2 pressurization. Thus, the linearly increasing higher displacement levels in and around the reservoir-fault interface up to and including 1.38×10^{-4} m conversion is acknowledged where the fault behaves like a strain concentrator, associated with slippage or discontinuity of displacement. Further, although slippage still occurs as stresses dissipate along the fault, the displacements decrease down to levels less than 2.0×10^{-4} m as indicated by the dark blue contours—representing a less disturbed host rock less invaded in upper levels. Yet, even still, it is displaced relative to a faulted system which corresponds to stress redistribution from heterogeneous orientations. Additionally, the gradient is smooth. This shows that the numerical simulation successfully reflects the geologic interactions from the pressures applied comparable to that of In Salah experienced along its faulted systems. Such a response mirrors fault reactivation as being only in areas where the

planes exist as it decorrelates into far field.

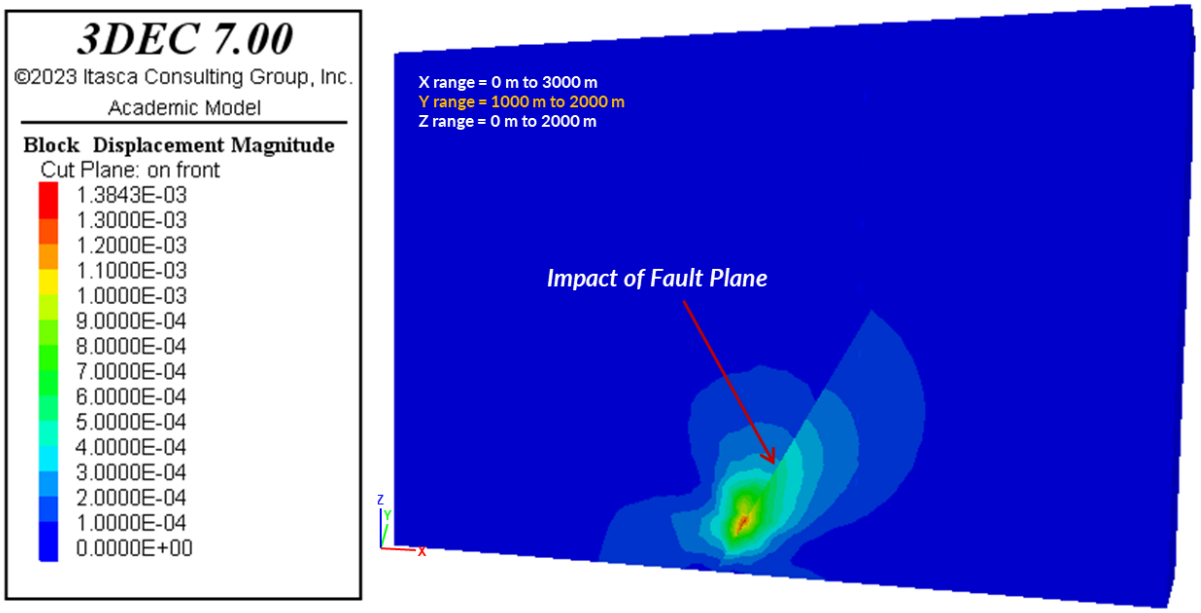

Figure 23. The calculated displacement field on the XZ plane after pressurization (fault dip angle Θ_{fault} = 60°; dip direction (DD) = 270°)

Furthermore, the profile of displacement on other planes reveals the same in terms of displacement values and total displacements within a faulted volume with planes along the XZ plane (vertical plane) of Y= 1000m, 1050m, 1100m, and 1200m (Figure 23). The evaluation of each profile suggests that the fault plane is the center of deformation as it is the place where the majority of deformation occurs. For instance, in Figs 8a-d, the magnitude of displacement indicates that no matter which plane was assessed, large magnitudes occur closer to the fault plane. The greatest magnitudes occur adjacent to the fault core and decrease thereafter as distance increases from the fault, creating an attenuation effect, which essentially illustrates how effective the fault is in accommodating deformation as stress dissipates through the intact rock mass. Similarly, the planes of intersection assessed for the total displacement within the XZ plane by viewing Figure 24 assess the total displacement of the resultant total displacement in the XZ plane. Here, this field is not even, which implies that the resultant total displacements are occurring along the fault plane and further, over distance, the magnitude of displacement significantly decreases such that relative to faulted displacements to non-faulted displacements grows.

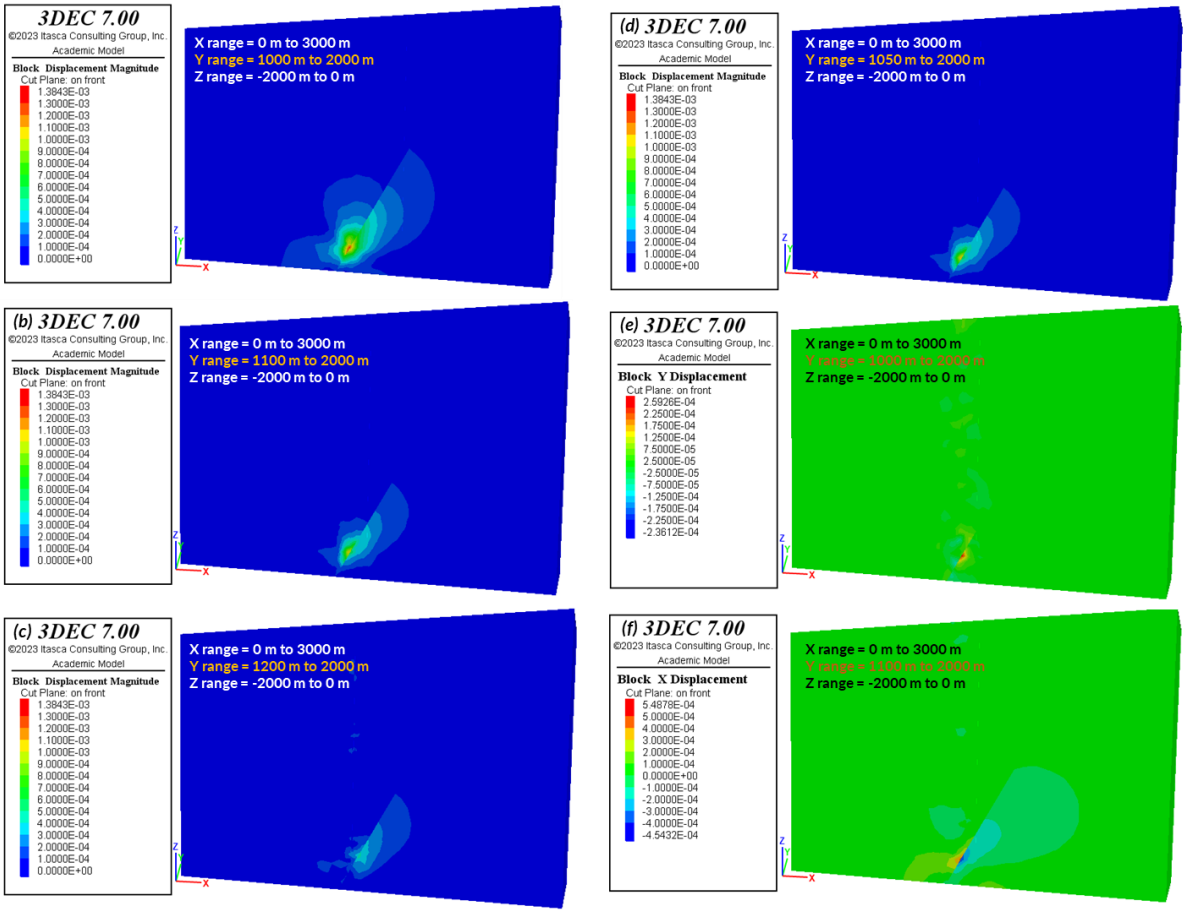

Figure 24. Displacement magnitudes and total displacements in a faulted domain (fault dip angle Θfault = 60°; dip direction (DD) = 270°), showing localized deformation near the fault plane.

Along the fault plane itself, the displacement magnitudes are highest where one would assume, right along the fault plane (Figures 25-26). It's important to note that fault slip is something that occurs as shear displacement along a fault surface. The maximum shear displacement is 2.24×10^{-3} m within the fault's central zone where stress concentration and slip are focused. There is also slip in the direction of the fault plane, which is determined by the orientation of the shear displacement vectors that align parallel to the fault plane. The global displacement vectors on the fault plane show the incremental fault impact on the mechanical stress field. Since perpendicular to the fault plane, the farther away one gets, the lower the incremental displacement magnitude is. Therefore, the orientation of the shear displacements compared to the fault slip suggests that they are highly coupled. Fault slip is noted to be asymmetric, however. This means that the resultant direction and magnitude of displacements are due to additional factors such as fault geometry. Ultimately, such findings relative to localized shears and alignment of displacement direction along the faults indicate that slip along the fault is good to relieve the induced strain field while causing decreased deformation.

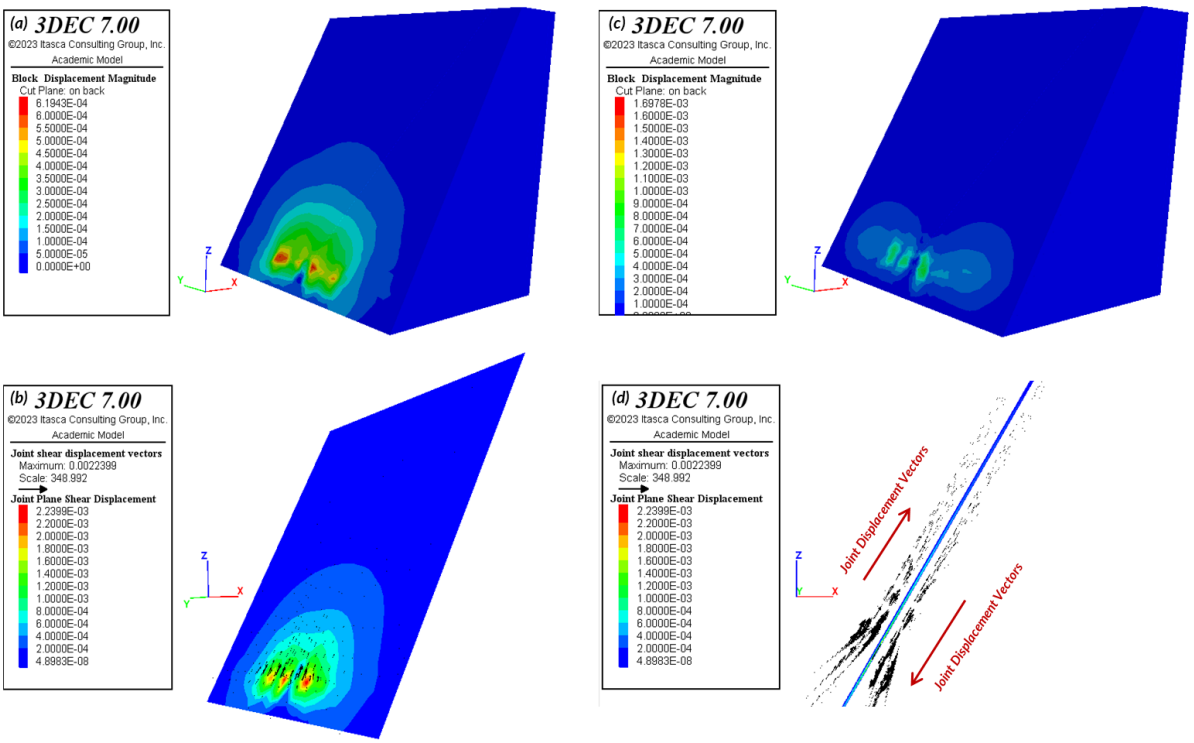

Figure 25. Fault slip showing localized shear displacement and aligned displacement vectors along the fault plane (fault dip angle Θfault = 60°; dip direction (DD) = 270°) at the region of interest (X = 1500, Y = 1000, Z = -1800): a) block displacement magnitude, b) shear displacement magnitude, c) block displacement magnitude at X = 1520 m, -d) fault displacement vectors showing the slip profile.

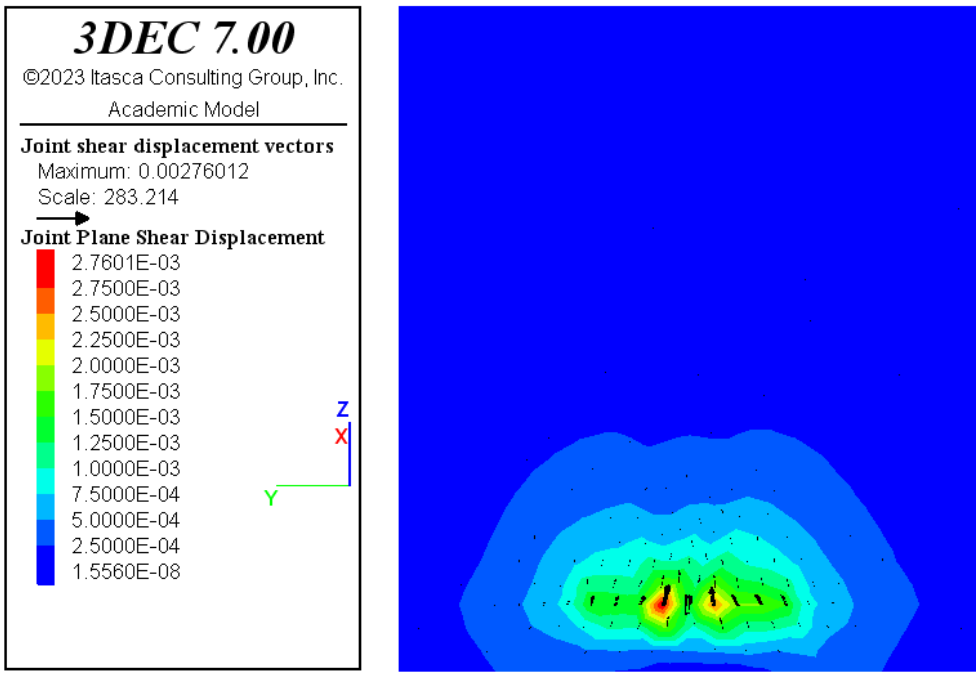

Figure 26. Shear displacement and slip vector distribution on fault plane for base case injection scenario at the region of interest (X = 1490, Y = 1000, Z = -1800)

The maximum resolved shear displacement is approximately 2.76×10^{-3} m and is obtained in two localized slip patches at the center of the fault plane. An elliptical shape of lower slip displacements exists relative to the distance from the core of the fault between these two high slip patches. This suggests that rather than being reactivated through uniform sliding over the fault surface owing to pore pressure and stress concentration along the fault trace from CO_2 injection, the fault is reactivated in a distributed fashion. The orientation of the shear vectors parallel to the fault suggests that the slip motion occurs primarily as a strike-slip. In addition, the displacement field extends over a large radius about the fault plane in the horizontal direction with minimal vertical dispersion; this suggests, through the spatial gradient of field support, that the slip occurs with the greatest force at the central fault planes and dissipates along the way where stress reduces and shear resistance increases. The irregularity of the vector density might imply that the fault geometrics are non-uniform or that fault mechanical properties are heterogeneous. The fact that the fault is still in a steady state of slip operation comes from neither the magnitude of the shear vector field nor the shear vector field having allegiance to one directional force. The fact that it is limited and localized implies that while the fault experienced an increase in pressure, it was not enough to push the fault over the edge into runaway slip, instead keeping it in a shear-controlled state with stressed conditions based on in situ stresses, fault strengths, and volume of pressured fluid exerted.

Across the XY-plane of the model (Figure 27), the location of interest (X = 1500, Y = 1000, Z = -1800) features an adjacent deformation of the rock domains of the storage reservoir with the induced stress leading to block displacement of 1.7×10^{-3} m. Outside the location of interest, however, the stress application remains less; thus, there is an attenuation of strain energy into less stressed areas of the model. The fault, however, is apparent in the top-down views as a linear feature inducing displacement in both directions along its length with a symmetrical alignment of displacement values. The fact that high values of displacements exist on the fault's interior but extend outward to low values suggests that fault geometry plays a role in the reallocation of stress. This makes sense, as the fault seems to take on a lot of the displacement well while the excess material just outside the faulted region seems relatively spared. The side views (Figure 27e-f) help render this clearer, as displacement extends perpendicularly along the fault itself. Those zones where blocks exist with no deformation are situated further away from the fault. Areas of maximum displacement are confined to the interior of the fault, once again.

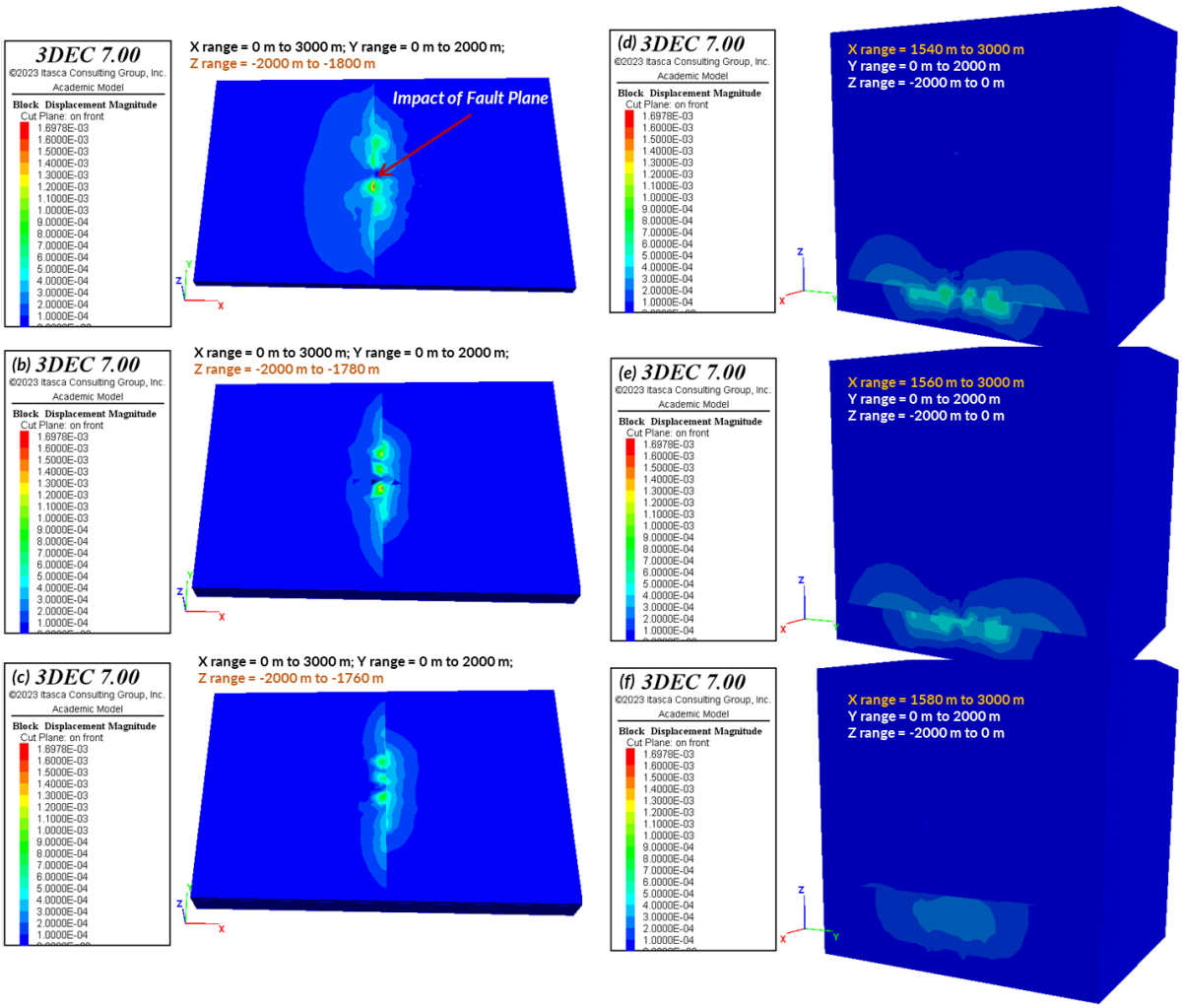

Figure 27. Displacement magnitudes highlighting fault-controlled deformation at XY- and YZ-planes (fault dip angle Θfault = 60°; dip direction (DD) = 270°) at: a) Z = -1800 m, b) Z = -1820 m, c) Z = -1840 m, d) X = 1540 m, e) X = 1560 m, f) X = 1580 m.

Figure 28 reveals the comparative vertical displacement over timesteps from the simulations per nine monitoring points at specified coordinates relative to the Z-axis (detailed in the legend). The sequential displacement thus helps determine how this system deformed over the applied loading per depth. For example, monitoring point V1 (X = 1500 m, Y = 1000 m, Z = -1800 m) exists in the middle of the XY-plane directly above the storage reservoir (deeper section, Z = -1800 m) and thus, from the onset, provides a clear negative displacement (subsidence). Its Z-displacement goes down to about -0.0005 m before creeping back up in a positive direction slowly. Thus, as this reservoir is a boundary condition, significant loading condition pressure applied in this area stabilized initially leads to these conclusions. The conclusions indicate that excessive pressure from the boundary conditions mainly affects the storage reservoir seal units (i.e., lower caprock and underburden) with some additional displacement from fault reactivation. In contrast, history points closer to the surface (Z = -1000

m) over time experience less displacement; stabilized transition displacements show stabilization over timesteps. For instance, V9 (X = 1500 m, Y = 1000 m, Z = -200 m) still has a substantially lower maximum/minimum Z-displacement than points above. However, like V1, it is a consistent increase in positive Z-displacement over time, meaning stabilization occurs in the upward direction for many of these other Z-displacement locations. The locations that have Z-displacement in the middle of both ranges assist in supporting the gradient of depth-based displacements. Ultimately, regardless of whether the displacements across depths stabilize over time in a positive or negative direction, they all show distinctions that indicate complexities in stress redistribution across various faulted domains throughout the mesh. For the deeper parts, this indicates more stress-related volume changes due to being closer to the fault core or increased confining pressures; for the shallower points, this indicates being less relatively stressed influences.

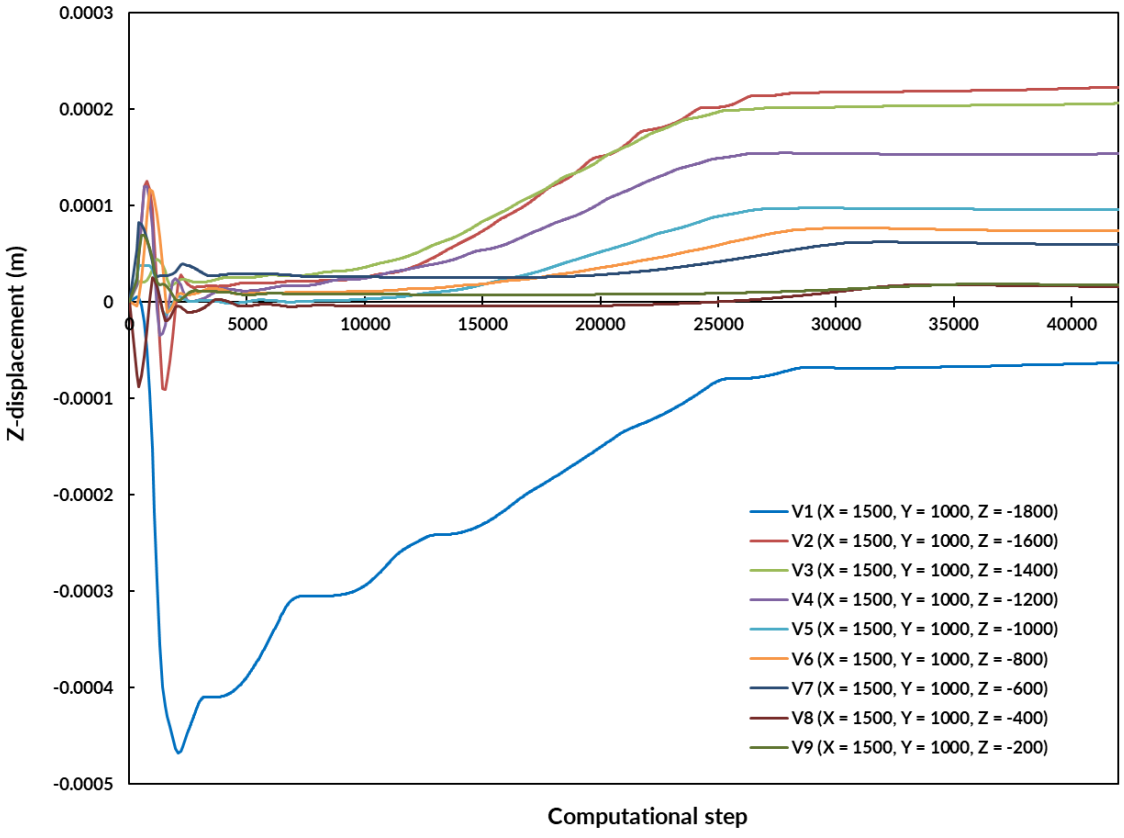

Figure 28. Vertical displacement evolution at monitoring points (refer to Figure 17)

Figure 28 notes that at first there's a little bit of stick-slip, but afterward, similarly to the rest, each point has fault displacement steadily increasing over time, reaching a semblance of steady state at the end and re-fault plane arrest. Because V1 is a measurement point directly

above the reservoir storage layer, this location is more affected by the seal pressure. When well flow starts to enter the reservoir, part of the seal drops. Therefore, during the injection period, the prolonged pressure geometry increases the upthrusting rate for this location (X = 1500, Y = 1000, Z = -1800).

4.2 Sensitivity Study

4.2.1. Parametric study of the effect of host rock strength

This subsection will demonstrate how varying host rock strength parameters will change the reservoir displacement field related to fault slipping and the induced caprock penetration mechanisms. Figure 29 shows how fault host rock physical properties—Young's modulus, cohesion, and friction angle—all impact fault slip during CO_2 injection. The first subpanel indicates how varying Young's modulus impacts the fault slip sub-distribution. Here, we see that varying Young's modulus provides an increasing trend; decreased stiffness yields increased slip with the maximum displacement occurring in 1.6 mm increments above and below the fault plane at the injection zones. This is indicative of greater deformability capacity of a softer rock mass that will be more effective at absorbing stress concentrations. Conversely, a stiffer fault host rock compound will restrict deformation and reduce peak slip to 1.1 mm whilst marginally increasing the active slip zone width. The average percent change in cohesion—blue line—experiences marginally non-increasing slip with the maximum peak just above 1.5 mm. Lower cohesion values respond similarly, suggesting that similar trends are at play here; however, they are less impactful or dominant to the modulus-related findings—all likely secondary to fault slip occurring after failure occurs. When cohesion increases, though, the fault slip fairly decreases, meaning that increased cohesion provided some resistance to reactivation early on, but not enough to change the overall area of impact pattern as similar slips occurred overall; just at a different time frame. Yet the right subpanel induces more probable change patterns, with a 20% decrease in friction angle yielding an over 2.0 mm peak fault slip and wider fault slip zone. Increasing the friction angle, however, keeps slip below 1.0 mm and confines displacement to slightly deeper than the injection depth at finality. Thus, it appears that fault weakness as shear strength is easily overcome during incremental slip under varying pore pressures, with the third subpanel showing how effective friction angle is as a controlling mechanism for fault onset and growth.

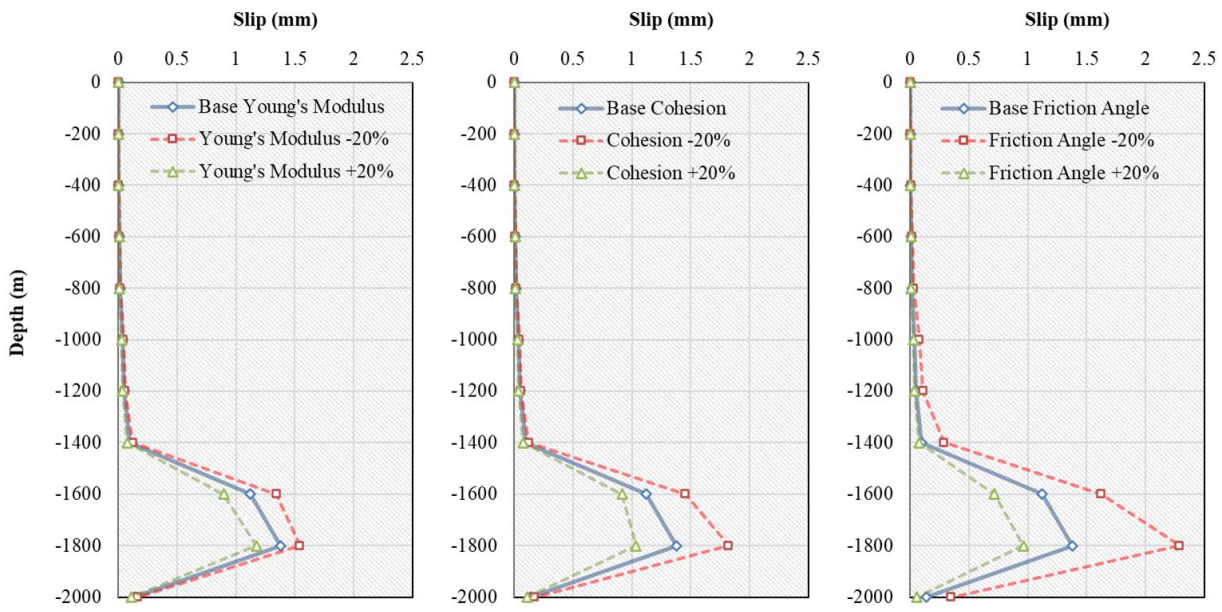

Figure 29. Sensitivity of Fault Slip Distribution to Variations in Host Rock Mechanical Properties During CO_2 Injection

Figure 30 illustrates the fault plane vertical displacement at the monitoring point when running with different caprock strength properties (Table 1). For the weakened caprock scenario, the monitoring point obtains the maximum Z-upward displacement of approximately 0.0004 m. This behavior suggests less mechanical confining abilities for the weakened caprock, where less vertical displacement is resisted and pressure can transfer from depth. Thus, this trend suggests that deeper in the caprock layer, there is no effective resistance, and thus it continues to rise, albeit at a lessening rate. For the base run scenario, Z-upward displacement is slightly positively biased but levels off at 0.0002 m. This average response is due to the fact that the caprock and fault properties have enough abilities to confine such a response that stress does not travel too far, but not enough to prevent some stress displacement from deeper in the caprock. Finally, for the strengthened caprock situation, Z-upward displacement is the least and levels off at zero after an initial negative spike. The strengthened properties of the caprock nearly eliminate vertical displacement, effectively confining stress volumes above and below the fault core layer. The leveling off at zero suggests that the strengthened caprock confined stress enough to not allow too much transfer to the monitoring point. The initial negative Z-displacement indicates some sort of settling across all three cases which is probably inherent due to the negative volume response, which implies some stress reallocation that occurs quickly after the run begins. However, how much Z-displacement upwards or downwards occurs depends significantly on the mechanical properties of the caprock in place.

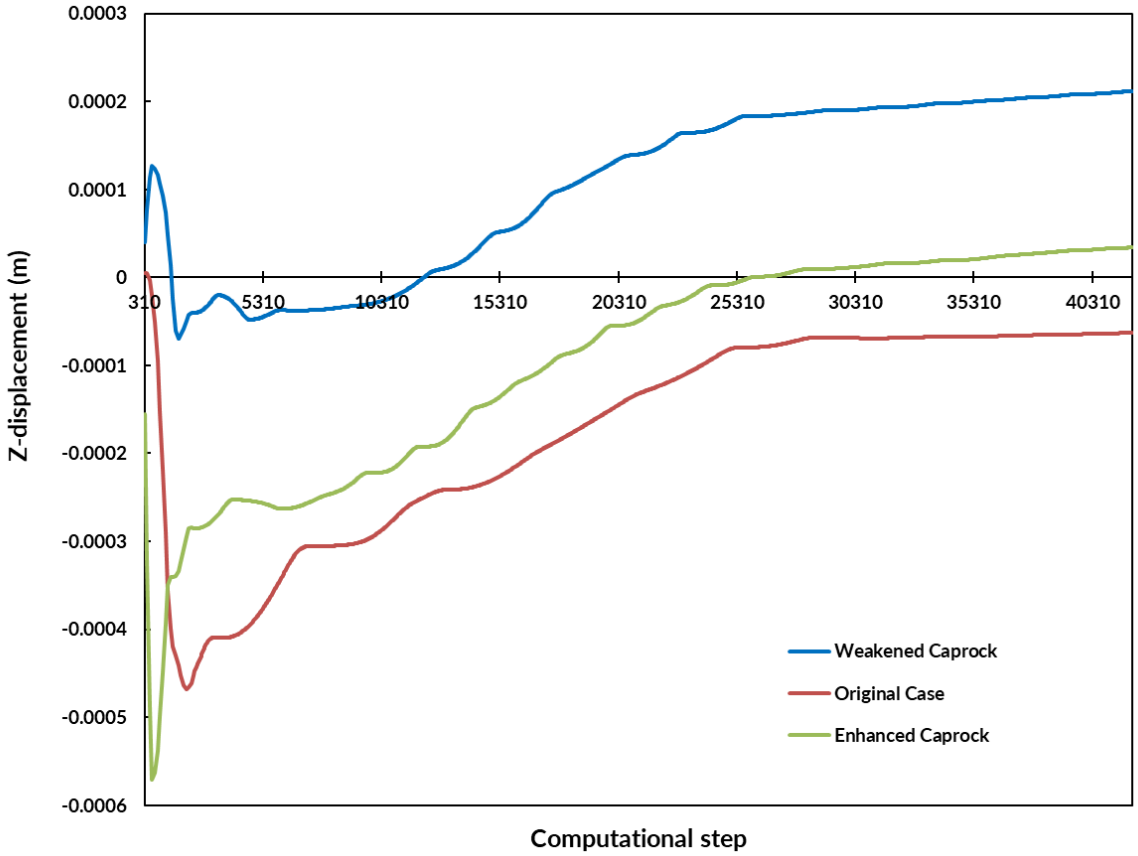

Figure 30. Vertical displacement evolution at monitoring point V1 (1500 m, 1000 m, -1800 m)

4.2.2. Sensitivity study of the effect of in-situ stress ratio

The stress field surrounding the reservoir varies depending on in-situ stress ratio (horizontal stress to vertical stress ratio, k), which affects caprock displacement and failure. Figure 31 presents the fault slip response with depth for increasing to decreasing horizontal-to-vertical stress ratios (k=0.5, k=1.0, k=1.5, k=2.0, k=2.5). While the caprock displacement response is provided elsewhere, this fault response figure only captures the shear movement of the fault plane itself. Yet, we can still determine from the fault reactivation response that in-situ stress ratios clearly dictate whether or not faults reactivate. For k=1.0, representing a hydrostatic condition, minimal slip occurs, with maximum slip in the reservoir zone at 1.1 mm. For k=1.5 and k=2.0, maxima are about 1.35 mm and 1.6 mm respectively, with the faults reactivating at the same depths and limitation of displacement confined to 1600 m to 1900 m. Yet for k=2.5, maximum slip exceeds 2.1 mm limited strictly to 1800 m. Thus, increased horizontal stress favors a shear failure of the fault plane since the maximum differential stress occurs in the direction of the fault plane orientation; the more pressure applied perpendicular to its plane, the easier fault planes fail and fail shear-wise. Yet for k=0.5, contrary findings

prevail; maximum slip occurs earlier and over a more extensive interval, meaning that lower lateral support provides more opportunity for uniform shear failure over a vertical domain, increasing the height of the fault rupture zone. It's clear that it's not just horizontal stress that allows or disallows increased fault reactivation but how stress anisotropy plays with the stress field geometry and extents—presented by a non-linear response across k values.

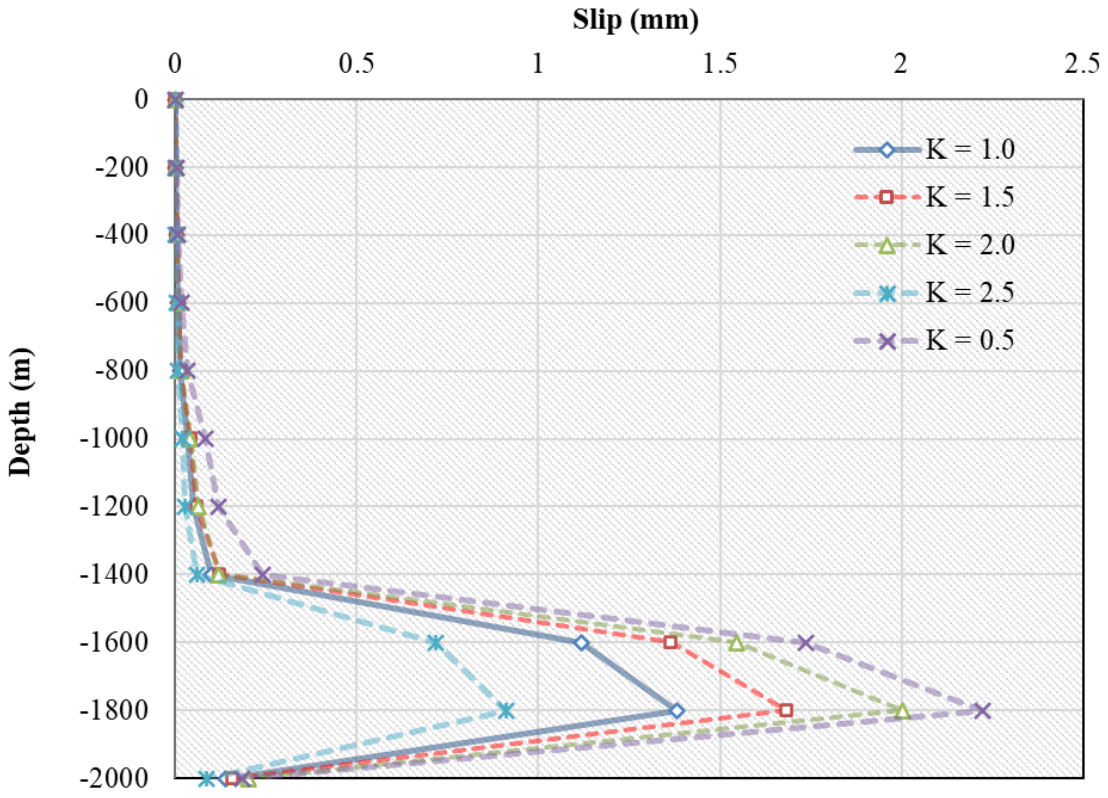

Figure 31. Depth-dependent fault slip distribution under varying in-situ horizontal-to-vertical stress ratios (k) measured at monitoring points V0, V1, F1-F9.

The k ratio has a significant impact on the reservoir displacement field. For example, Figure 32 presents the caprock vertical displacement very close to the locus of injection. For k = 0.5, we see a slight negative subdisplacement followed by a relatively great positive displacement with everything leveling off around 0.0003 m. Thus, this means with a weaker horizontal confinement stress, that vertical deformation is the more potent force. Thus, the system is less confined and more subject to effective stress changes by how much it can withstand and be transformed into displacement. For k = 1.0, however, this means the stress field is hydrostatic and the caprock displacement field becomes stabilized as evidenced by the relevant curve essentially plateaued with no change in the domain of displacement magnitude. This is because the ratio of vertical and horizontal stresses has been balanced so that a stabilized system is formed where neither stress can overpower the other at any given node of observation

while those select nodes of observation stabilize successfully and dissipate the magnitude of displacement at this certain location. As k increases for k = 1.5, 2.0, and 2.5, the response of the final k monitored node is all different. Incrementally increasing k, however, increases the displacement about this k. Yet for k = 2.5, it levels off lower than 0.0001 m. Thus, a much higher k means less net upward displacement. Thus, for very high stress ratios, horizontal stresses in the stress field as a whole prevail and they act as a clamping/confining stress to the caprock. Thus, less vertical deformation occurs, but more strength and stabilization of the caprock is obtained due to relative gains in in-situ strengths of the rock mass such as increased horizontal confinement of stresses. Moreover, even the initially negative subdisplacement found in all cases becomes less negative relative to k = 0.5 with higher k—meaning that increased horizontal stress not only allows for stabilization, but it provides benefits for static conditions as well.

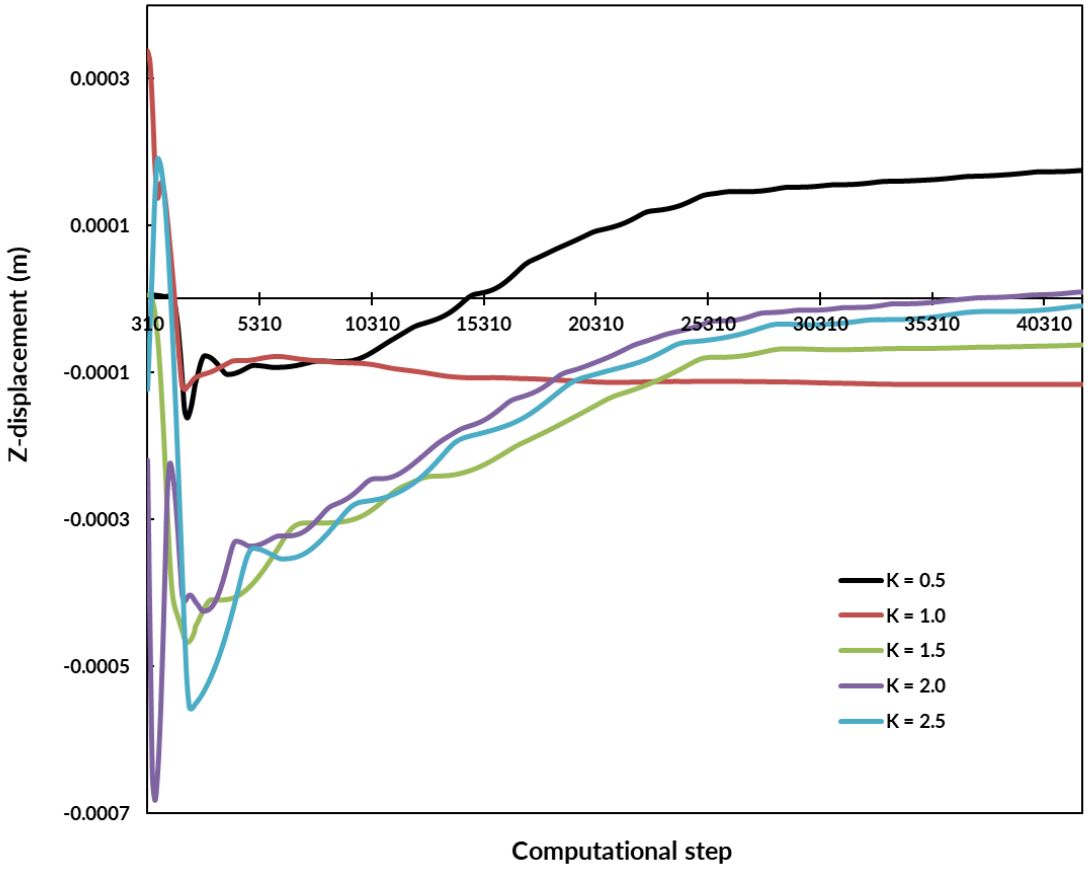

Figure 32. Variations of vertical displacement at monitoring point V1 (1500 m, 1000 m, -1800 m) for varying in-situ stress ratio

4.2.3. Parametric study of the effect of fluid parameters

Figure 33 compares fault slip with depth due to other fluid properties—bulk modulus,

viscosity, and injection rate—during CO_2 injection. For the bulk modulus, on the left, increasing the value from 180 MPa to 216 MPa has the peak slip within the reservoir zone go from 1.34 mm to 1.65 mm. This is a 22% increase because the stiffer fluid phase is less compressible, leading to more pore pressure being transmitted to the fault, thus resulting in greater effective stress perturbations. Lowering the bulk modulus to 144 MPa results in a peak slip of 1.17 mm; that is, more fluid accommodation and mechanical damping. For viscosity, the impact is slightly less. Lowering it from 1.0 cP to 0.8 cP increases the reservoir slip from 1.34 mm to 1.43 mm; therefore, this means it factors in positive pressure diffusion and fault stress accumulation over longer timescales. Raising viscosity to 1.2 cP drops slip to 1.26 mm, which makes sense, as it means that pressure transfer takes longer and aquifer permeability has higher resistance. While the magnitude is relatively small—10%—the resultant change in direction shows how viscosity can either promote or inhibit effective pressure transfer. Increasing the injection rate from 5 l/s to 6 l/s, however, increases the peak from 1.34 mm to 2.08 mm—which is a 55% increase—and the thickness of the depth range affected increases in the positive direction. Thus, by lowering it to 4 l/s, the peak slip falls to 0.99 mm, and the width of the slip zone decreases in thickness, indicating that pressure transfer is the most effective contributor to fault reactivation.

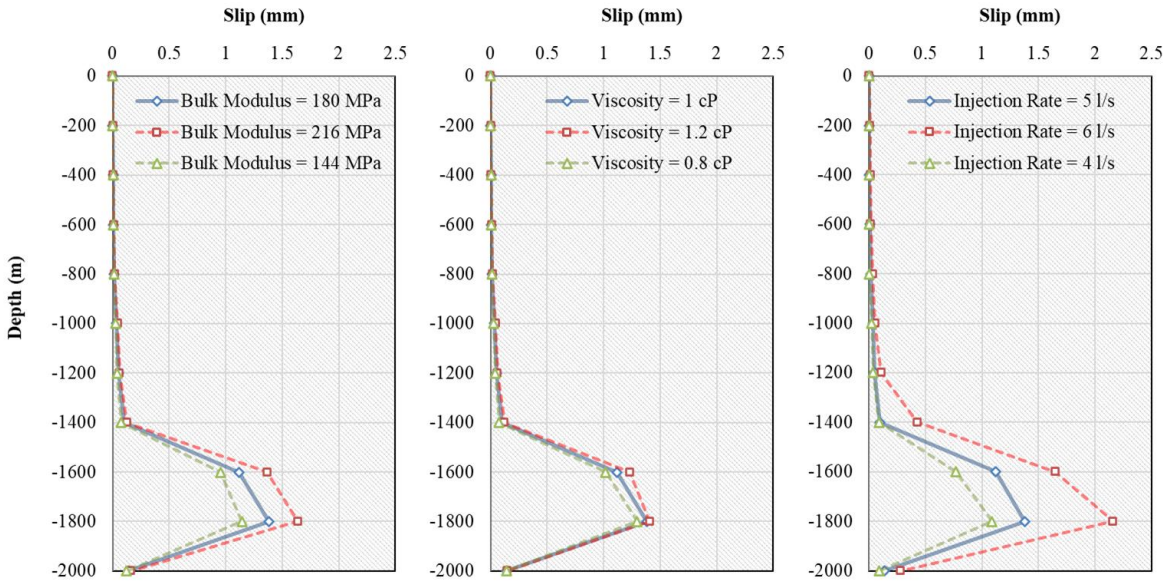

Figure 33. Depth-dependent fault slip distribution under varying operational parameters (injection rate, fluid viscosity, fluid bulk modulus) measured at monitoring points V0, V1, F1-F9.

Figure 34 shows varying transient response for pore pressure changes, indicating that the direction and magnitude of oscillations occur based on selected parameters (i.e., bulk

modulus, viscosity, and flow rate). The highest flow rate had the highest pore pressure initial peak at over 26 MPa created at first but then declined at a consistent rate once systems stabilized; the lowest flow rate had a much lower peak level with a less aggressive transient increase, meaning that with slower flow, the system takes longer to adjust but avoids aggressive changes. The same is true for increasing or decreasing changes in viscosity. Decreasing the viscosity creates a much more stabilized response, as shown by the lower transient peak and higher levels relative to stable pore pressure; increasing it does the opposite and creates a slightly higher equilibrium pressure. The same occurs when adjusting the bulk modulus. Decreasing the bulk modulus results in decreases in both initial peak and stabilized pressures; increasing the bulk modulus leads to slightly higher stabilized pressures as it is less compressive. Ultimately, all conditions stabilize into similar stabilized pore pressures regardless of initial fluctuations.

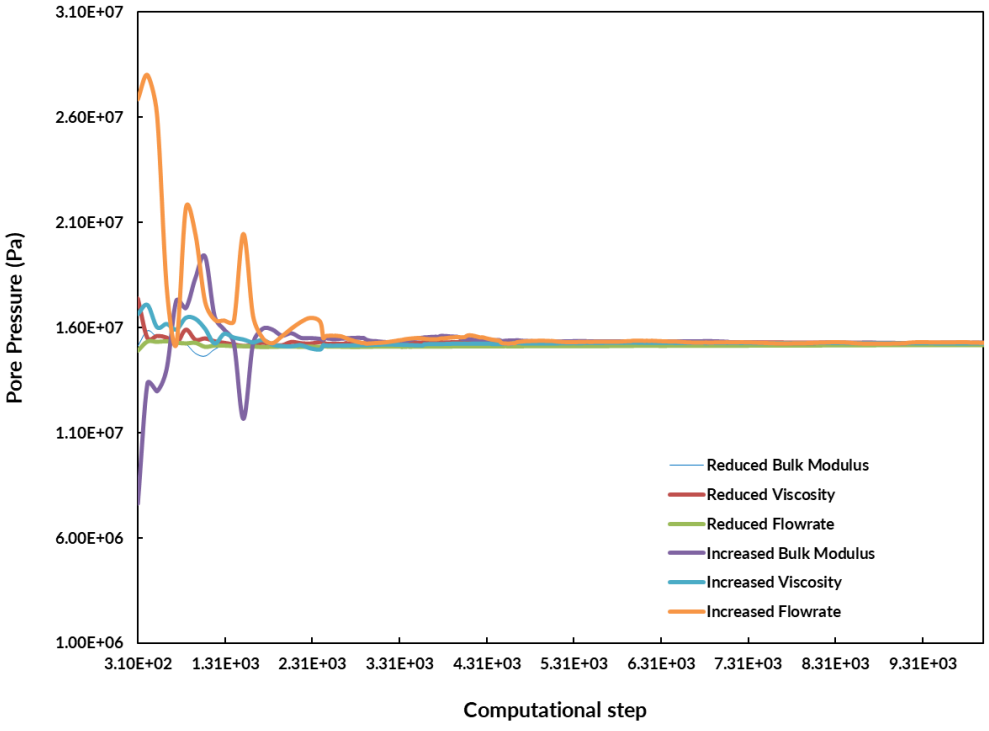

Figure 34. Pore pressure evolution under varying bulk modulus, viscosity, and injection rate conditions at monitoring point V1 (1500 m, 1000 m, -1800 m).

4.2.4. Parametric study of the effect of fault orientation

This parametric study assessed the impact of fault dip and dip direction—fault geometry—on fault activation potential based on analysis of the caprock displacement field

and fault shear displacement when fault geometry was varied and all other input parameters remained constant. Figure 35 shows the results of the observed maximum fault shear displacement in relation to fault dip angle. The results of this numerical study indicate that an increase in fault dip angle results in a decrease in shear displacement as fault slip behavior is clearly dependent on the angle at which the fault dips (Figure 35). For instance, when the fault dips at 15°, the maximum shear displacement is 1.07×10−2 m, which is the highest amount of shear displacement recorded in this study. Therefore, the tendency for low-angle faults to slip is apparently due to a preferable direction of shear stress activation relative to the orientation of the fault plane. When the dip increases to 30° and 45°, maximum shear displacements equal 8.7×10−3 m and 5.8×10−3 m, respectively, indicating that incrementally less preferable angles at which to dip provide the activation for shear stress to occur along the fault surface. Finally, at the steepest angles, 60° and 90°, the maximum shear displacements equal 2.2×10−3 m and 8.9×10−4 m, respectively. At increasingly more vertical positions, the faults are unable to slip as normal stresses dominate the fault behavior, thereby decreasing shear displacement.

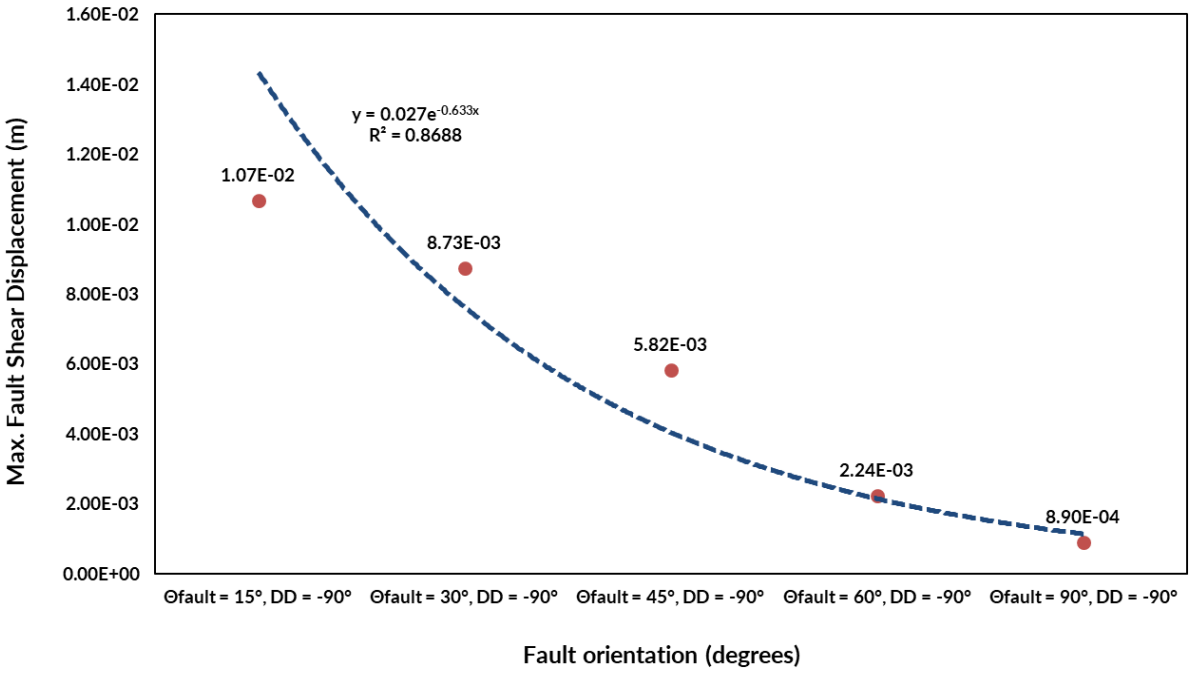

Figure 35. Change in maximum fault shear displacement as a function of fault dip angle

Yet, even with this, the dashed line trendline in the figure indicates the inverse relationship as well. Fault orientation essentially determines if it can slip or not, and therefore, these results emphasize that fault dip is important for fault behavior. Low-angle faults are more prone to be — mechanically — faults that slip. Higher angle faults are more stabilized with the

same stress application. Then, for instance, when we change the DD of the fault from 270° to 180° (maintaining the dip angle at 60°), we have greater shear displacements at 3.58×10−3 m, which means that the turning of the fault orientation changes the stress partitioning, allowing for more shear (Figure 36).

For DD = 180°, we further increase this to 4.91×10−3 m, which indicates that when the fault plane orientation aligns with the principal stress orientation, it allows for more slip potential. The largest displacement comes from two faults intersecting with DD = 270° and max shear displacement at 2.15×10−2 m. This extreme increase occurs because of the physics involved with two faults intersecting—stress is greater in the intersection, leading to stress concentrators that allow for greater shear displacement to occur. Here it seems that in addition to the primarily fault reactivation stresses inducing micro-slips, the intersection also induces micro-zones of stress convergence that highly increase the fault movement than if it were a fault alone. Therefore, while fault dip does not necessarily induce an extreme amount of discharge unless the faults are intersecting, the intersecting faults create a much more significant effect.

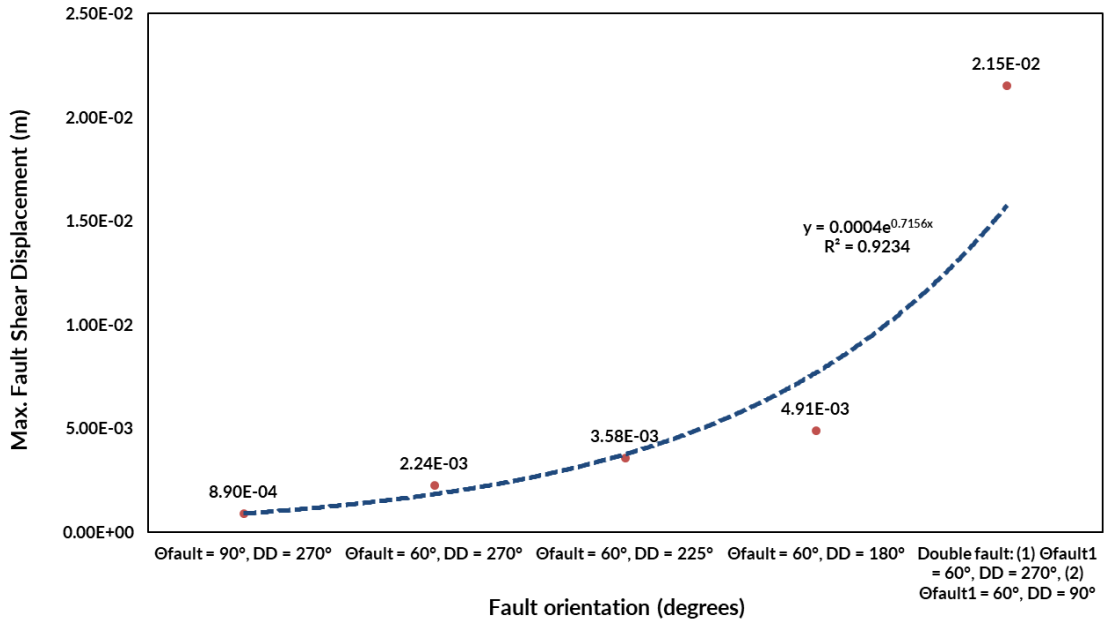

Figure 36. Maximum fault shear displacement as a function of fault dip direction.

Yet, since the maximum shear result displacement was a cause for concern with the faults crossing each other, faulting mechanisms are of interest to investigate such a geomechanical reaction. Thus, a closer profile of the fault planes is investigated in a second set of runs. The intersection area and fault shear displacement vectors in Figure 37 suggest that stress

concentration and dynamic triggering aid in slip between both faults; increased fracture complexity has less resistance to motion. The major findings established in comparison with what was learned are found in Table 5.

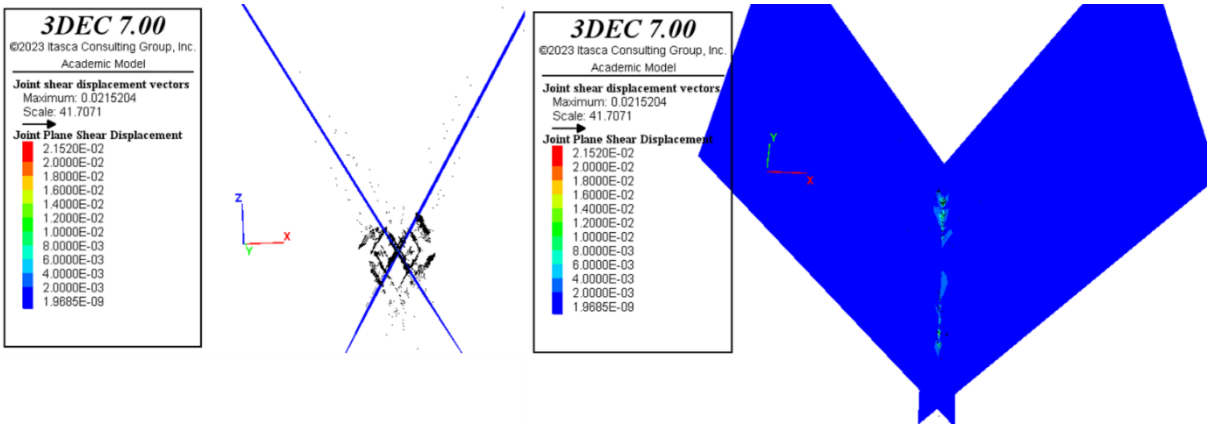

Figure 37. Shear displacement profile of two intersecting fault planes dipping at Θfault = 60°

Table 5. Summary of fault type configurations and their associated slip behaviors under varying dip angle and dip direction conditions

Fault Type	Main Observations	Fault Type	Main Observations
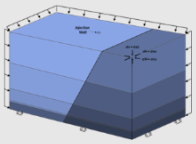	▪ Aligned with the principal stress but at a non-ideal orientation. ▪ Slip remains constrained due to higher normal stress component. ▪ Stable behavior relative to shallower faults.	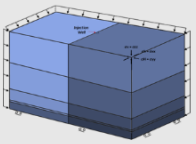	▪ Vertical fault orientation dominated by normal stress. ▪ Shear failure suppressed despite stress perturbation. ▪ Least likely configuration for slip initiation.
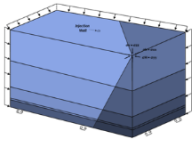	▪ Oblique dip direction aligns more favorably with shear stress. ▪ Larger rupture area suggests increased fault participation. ▪ Transition zone between stability and reactivation.	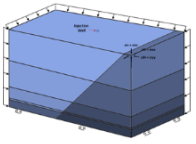	▪ Balanced interaction of shear and normal stress. ▪ Represents transition between low-angle activation and high-angle stability. ▪ Potential for slip remains but is reduced.
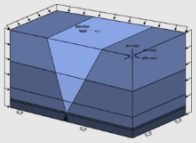	▪ Fault interaction intensifies stress concentration at junction. ▪ Triggered slip along both planes through dynamic feedback. ▪ Demonstrates the critical role of structural complexity in fault behavior.	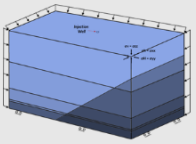	▪ Favorable shear alignment but less optimal than shallower angles. ▪ Decrease in displacement indicates growing influence of normal stress. ▪ Fault remains prone to reactivation.
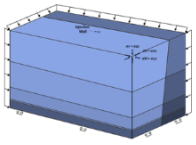	▪ Optimal orientation for shear failure under the given stress regime. ▪ Broader displacement distribution along the fault plane. ▪ Reactivation risk higher than other single-fault cases.	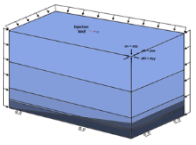	▪ Near-optimal orientation for shear stress resolution. ▪ Strongly activated under injection-induced stress. ▪ Mechanically vulnerable to slip under minimal perturbation.

5. DISCUSSION

The overall experiment and then the parametric study show that fault stability during CO_2 injection is critically sensitized due to the interplay of fluid flow patterns, stress directions,

and mechanical properties/strengths of the caprock. It shows that all three elements work in a vacuum to impact deformational characteristics of the caprock and fault reactivation likelihood within a geomechanical setting. The Table 6 notes provide a mechanistic discussion of the findings during the parametric study.

Table 6. A summary of technical findings from the sensitivity analysis of key parameters involved in CO_2 storage

Parametric Study	Major Observations
Analysis Group A: The effect of host rock strength	Alterations in rock strength parameters, particularly cohesion and friction angle, significantly affect fault behavior. Reduced cohesion amplifies fault slip and displacement due to the diminished resistance to shearing forces, whereas higher cohesion promotes stability. Interestingly, the interaction between friction angle and tensile strength amplifies these effects. For instance, simultaneous reductions by 20% of all three parameters (cohesion, friction angle, elasticity modulus) result in a compounded increase in fault slip by approximately 40%, exceeding the impact of changes to cohesion alone. This highlights the synergistic influence of multiple strength parameters on fault reactivation potential.
Analysis Group B: The effect of in-situ stress ratio	The in-situ stress ratio strongly governs fault stability, with lower values (k = 0.5) promoting vertical upward caprock deformation and higher values (k = 2.5) inducing horizontal confinement and stabilizing the caprock. Notably, the transition from k = 1.0 to k = 2.0 reduces vertical displacement by 50%, suggesting a threshold where horizontal stresses dominate fault mechanics. This finding aligns with theoretical expectations but also reveals a nonlinear stabilizing effect that warrants further investigation in scenarios with more heterogeneous stress distributions.
Analysis Group C: The effect of fault orientation	Fault dip and dip direction are primary drivers of shear displacement. Low-angle faults (15°) exhibit greater slip due to favorable stress alignment, while steeply dipping faults experience reduced displacement. However, the presence of intersecting faults introduces a unique dynamic, as these regions amplify stress localization and slip

	by nearly 80% compared to single faults. This result emphasizes the mechanical complexity at fault plane intersections, which may serve as critical zones for induced seismicity.
Analysis Group D: The effect of flow parameters	Variations in injection rate and viscosity reveal distinct effects on pore pressure evolution. Higher injection rates significantly increase transient pressure peaks, destabilizing faults in the process. However, reduced viscosity promotes faster equilibration, lowering the risk of prolonged stress accumulation near critically stressed segments. A notable observation is the delayed pore pressure dissipation in high-viscosity scenarios, which extends the risk window for fault reactivation by nearly 30% compared to low-viscosity conditions.

5.1. Comparison with the field data

The In Salah carbon storage site boasts an established time history of surface deformation from the injection onset to the last known injection activity. The remote monitoring system with remote sensing SAR from space (InSAR, ALOS PALSAR, Envisat ASAR) allows for later acquired/upward mapping with time. For example, Figure 38 is a vertical displacement time series of forces, and it's apparent that surface uplift occurs slowly and consistently over time from injection to storage. Based on increasing pressure in the reservoir from continuing CO_2 influx, vertical surface deformations increase from 0-2 mm within the first 400 days up to 4-8 mm at the 1200-day mark and 16-18 mm at the 1800-day injection end (Onuma & Okawa, 2009).

The findings from the numerical simulation here provide the same insight as well. As shown in the Figures 39-40, vertical displacement increases with time. Yet, because the numerical simulation is performed with a static mechanical timestep analysis instead of a dynamics (that would provide a proper transient outcome and time response), the time-based expectation may differ from the real and the simulated. The base case, however, has only generated operational parameters that apply to this time-based analysis; for instance, when KB-502 is at 5.0 l/s in the beginning of operations, for the beginning simulation, the flow rate is 5.0 l/s (5.0 kg/s or 5.0 m^3/s is the same) and then, major injection rates are analyzed as part of the parametric study. To accommodate for the steadily increasing flowrate during sequestration, we exerted 15 kg/s of injection rate, which is three times the base number in the analyses. Thus, the displacement field generated from such an analysis correlates with field

data since the vertical displacement at Z = 0 m increases upwards to approximately 17.0 mm.

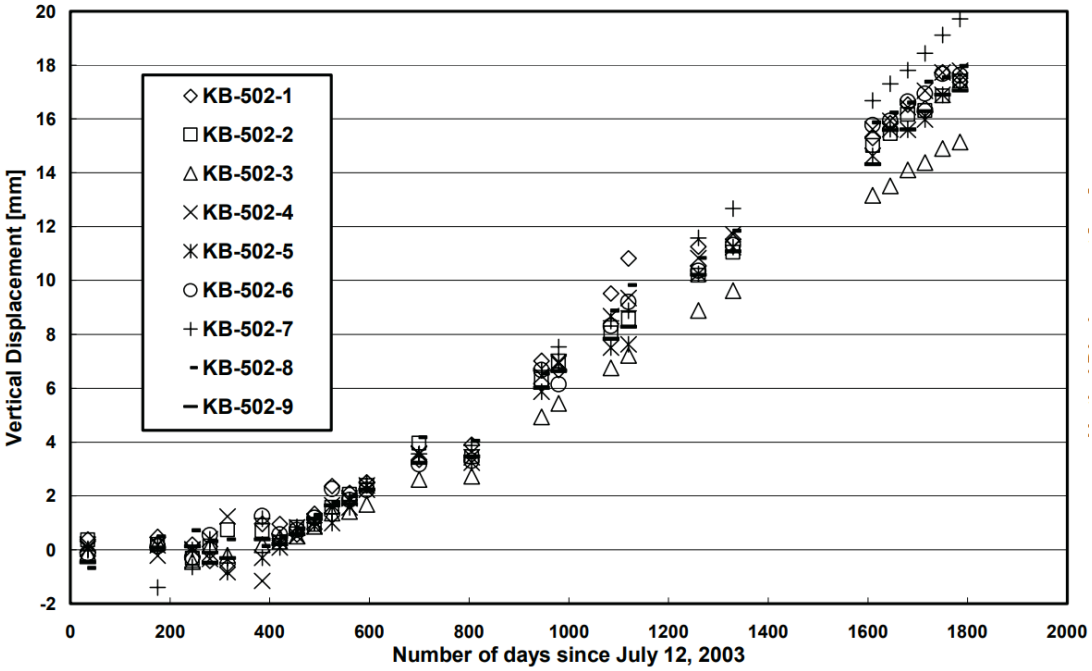

Figure 38. Deformation time series measured for areas of KB-502-1 through KB-502-9 around the injection well of KB-502 (Onuma & Okawa, 2009).

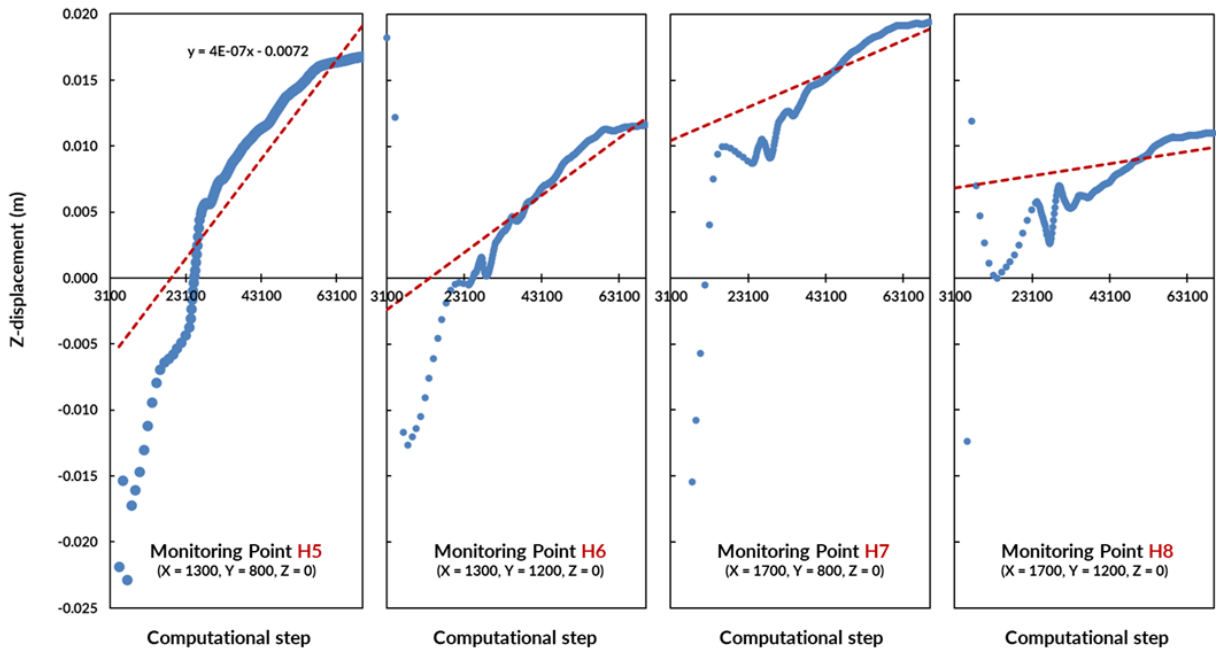

Figure 39. Changes in ground surface (Z = 0) vertical displacement determined numerically H5-H8

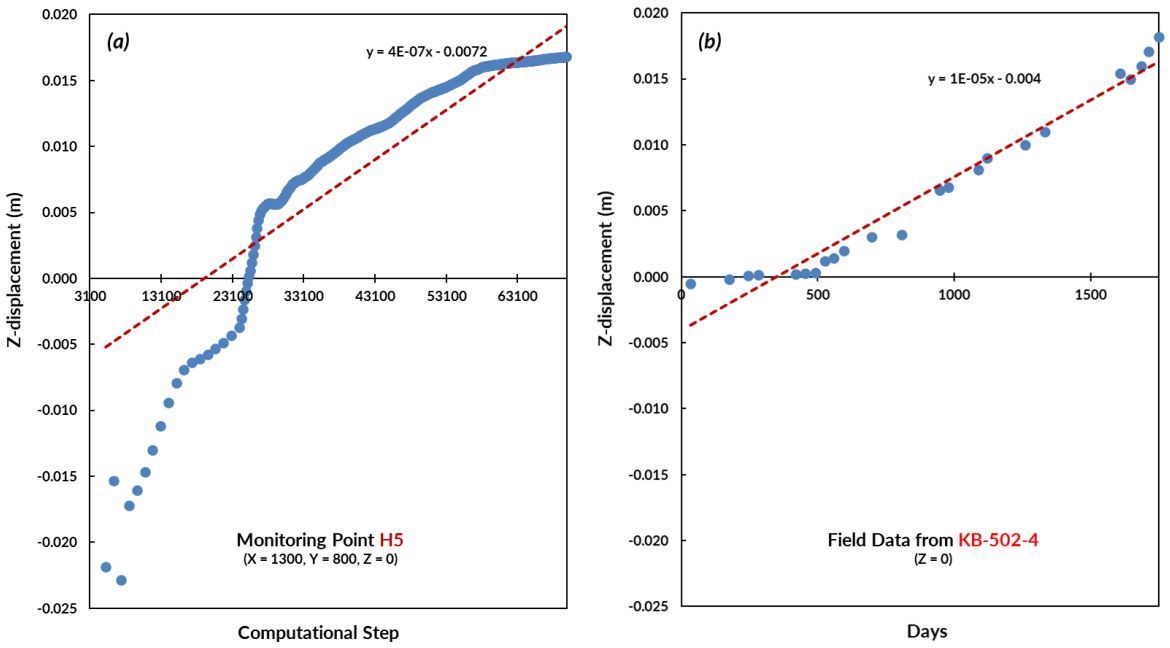

Figure 40. Comparison between numerically simulated surface uplift rate with the field data obtained by InSAR measurements (refer to Figs. 38-39): (a) Vertical displacement determined numerically at ground surface level (Z = 0 m), (b) Vertical displacement determined by remote sensing (InSAR) on KB-502-4 at ground surface level (Z = 0 m).

However, despite the unsuccessful conclusions beyond our control that exacerbate the shortcomings of this approach, we did find some consistent elements across results. These were the geographical/geomechanical/geological information provided to us and the assessed vertical depths of the faults. Furthermore, ours was a static numerical simulation, which means that the flow rate/pore pressure established was static as well, while during the actual carbon sequestration process, there is a variable input pressure which subsequently alters reservoir pressure. Therefore, future work should involve longer parametric studies as well as a full slip determination study under a dynamic assessment, obtaining overburden/caprock mechanical properties more relevant to this study.

6. CONCLUSION

This study established whether fault reactivation occurred during CO_2 injection by means of a fully coupled numerical model assessing the mechanical and hydraulic interplay of variables. The variables tested included fault geometry, stress state, host rock properties, and fault permeability and viscosity, with one base case in which the fault was evaluated post no variable adjustments. The findings offer extensive novel contributions to the current body of research on fault stability/reactivation likelihood, and field recommendations for effective

geological sequestration from a geomechanical design standpoint:

- Base case results indicated that faults were reactivated by concentrated deformation where the fault plane was located. For instance, the maximum displacement around the fault was approximately 1.38×10^{-3} m, while displacement attenuation occurred at a greater distance away from the fault. The shear displacement was aligned with the fault trace, indicating that slip occurred on the fault itself. Thus, such baseline results solidify the fault as the strain concentration source and suggest how much more effective preexisting faults are at accommodating reactivated stress transfer during fluid injection. This was used as a comparison and differentiator for the parametric study, as the faults' stability was clear at this junction.
- Fault orientation mattered for fault slip. Low-angle faults (15°) achieved a maximum fault displacement of 1.07×10^{-2} m, while steeply dipping faults (90°) did not achieve as much slip potential. Such means suggest that stress distribution along the fault plane in a consistent direction significantly influences future slip potential. In addition, faults at DD = 180° slipped more, indicating that dip direction matters for orientation. Moreover, intersecting faults created a maximum shear displacement of 2.15×10^{-2} m, meaning that additional intersecting planes encourage concentrated stress. Thus, factors based on geometry should be considered for fault viability.
- Fault stability was sensitive to stress conditions. Increased vertical deformation was observed from the parametric study at k = 0.5, relative to the base case, as vertical deformation observed at k = 1.0 (consistent with hydrostatic stress fields, stress ratio of k = 1.0). Increased fault slip was observed at k = 0.5. Alternatively, when k = 2.5, fault displacement was less and stability was higher. The fact that fault plane shear displacement decreased non-linearly from k = 1.0 to k = 2.0 shows that horizontal confinement due to horizontal in-situ stress components increases stability relative to vertical stresses.
- Increased fault displacement was observed during the parametric study relative to the host rock strength of the base case. Increased cohesion and the friction angle resulted in ~35% more slip; increased cohesion/fusion increased rock strength, resulting in up to 20% less displacement of the fault. This shows how

important the effectiveness of a caprock is to reduce the potential for fault reactivation.

- Ultimately, the average base case with mid-level injection and general fluid properties showed pore pressure development and fault response through time. Relative comparisons experienced high transient pore pressures, claiming higher injection rates and greater fluid viscosities to threaten the fault. Conversely, with lower viscosities and controlled injection rates, the fault experienced an incremental pore pressure dissipation, making slip less likely. Such findings indicate the necessity of injection best practices relative to field findings.

Moving forward, the effective coupling of more substantial field data in real time with the numerical analogs would allow for better assessment of what could happen down the line for more effective injection and extraction of the reservoir. This is necessary for the proper safety and effectiveness of any sustained CO_2 sequestration project.

7. REFERENCES

1. Alassi, H., Landrø, M., & others. (2008). Modeling Reservoir Geomechanical Changes Caused by Fluid Injection - A Discrete Element Approach.
2. Allafta, H., & Opp, C. (2024). Climate change paradox: The least responsible for it encounters the most of its implications. Climate.
3. Altaf, I., Johnson, R. L., et al. (2018). A Review of Current Knowledge with Geomechanical Fault Reactivation Modelling: The Importance of CO_2 Mechano-Chemical Effects for CO_2 Sequestration.
4. Alvarez, A., Salazar, V., Reyes, J., & González, R. (2023, June 15). Modeling Caprock Failure During Injection in a CO_2 Capture and Storage Project Using a Compositional/Geochemical/Geomechanical Coupled Numerical Simulation. Day 2 Thu, June 15, 2023.
5. Bao, J., Fang, Y., & collaborators. (2015). A coupled discrete element and finite element model for multiscale simulation of geological carbon sequestration. Greenhouse Gases-Science and Technology.
6. Bason, D., Pearce, A., & O'Brien, G. (2024). Geological Storage of CO_2: Seal Integrity Review. [Journal Not Provided].

7. Bohloli, B., Rucci, A., Korre, A., Ringrose, P., & Mathieson, A. (2013). Geomechanical assessment of ground surface uplift due to CO2 storage at In Salah, Algeria
8. Cao, M., et al. (2024). A Modeling Study of Injection-Induced Rupture and Seismicity in Complex Faults.
9. Cappa, F., & Rutqvist, J. (2011). Modeling of coupled deformation and permeability evolution during fault reactivation induced by deep underground injection of CO2. International Journal of Greenhouse Gas Control, 5(2), 336–346.
10. Castelletto, N., et al. (2013). Geological CO_2 sequestration in multi-compartment reservoirs: Geomechanical challenges.
11. Chang, K., Martinez, M., & others. (2022). Potential Seismicity Along Basement Faults Induced by Geological Carbon Sequestration. Geophysical Research Letters.
12. Chu, B., Meng, Q., & Huang, T. (2023). Residual saturation effects on CO_2 migration and caprock sealing: A study of permeability and capillary pressure models.
13. Elmo, D., Catalan, A., & collaborators. (2010). An integrated finite/discrete element method – discrete fracture network synthetic rock mass approach for the modelling of surface subsidence associated with panel cave mining.
14. Fentaw, J., Kabir, E., Islam, M. S., Pathak, S., & Thiyagarajan, S. (2024). Geochemistry in geological CO_2 sequestration: A comprehensive review. Energies.
15. Friedlingstein, P. (2020). Human induced changes on the global carbon cycle over the last 60 years.
16. Fu, W., Fuenzalida, M., & collaborators. (2023). Simulating hydraulic fracturing with varied well placement for preconditioning in cave mining.
17. Fu, W., McLennan, J., & collaborators. (2024). Modeling near-wellbore hydraulic fracture behaviors under combined impacts of wellbore perforation and natural fractures.
18. Galdies, C. (2017). A rapidly changing climate in an era of increasing global carbon emissions. Journal Not Provided.
19. Guzman, J., Korre, A., Durucan, S., & Rucci, A. (2014). InSAR monitoring leads to improved understanding of flow and pressure behaviour during CO2 injection at In Salah

20. Han, W., McPherson, B., Lichtner, P., & Wang, F. P. (2010). Evaluation of trapping mechanisms in geologic CO_2 sequestration: Case study of SACROC northern platform, a 35-year CO_2 injection site. American Journal of Science, 310(4), 282–324.

21. Hansen, J., et al. (2013). Climate forcing growth rates: Doubling down on our Faustian bargain. Environmental Research Letters.

22. Hou, S., Dong, H., Yuan, J., & Chen, Z. (2024). Caprock safety evaluation method in CCUS based on Latin hypercube sampling: A case study of a block reservoir. Journal of Physics: Conference Series, 2024,

23. Jackson, R. B., et al. (2018). Global energy growth is outpacing decarbonization. Environmental Research Letters.

24. Jackson, R. B., et al. (2019). Persistent fossil fuel growth threatens the Paris Agreement and planetary health. Environmental Research Letters.

25. Johnson, J. W., Steefel, C. I., Knauss, K. G., & DePaolo, D. J. (2004). Reactive transport modelling of CO_2 storage in saline aquifers to elucidate fundamental processes, trapping mechanisms and sequestration partitioning. Geological Society, London, Special Publications, 233(1), 107–128. https://doi.org/10.1144/GSL.SP.2004.233.01.08

26. Ju, Y., Xie, H., & collaborators. (2018). Numerical analysis of hydrofracturing behaviors and mechanisms of heterogeneous reservoir glutenite using CDEM. Journal of Geophysical Research: Solid Earth.

27. Khan, S., et al. (2020). The Geomechanical and Fault Activation Modeling during CO_2 Injection into Deep Minjur Reservoir, Eastern Saudi Arabia.

28. Kim, G.-W., Kim, Y., & Lee, K. (2018). Coupled geomechanical-flow assessment of CO_2 leakage through heterogeneous caprock during CCS. Advances in Civil Engineering, 2018, 1–14. https://doi.org/10.1155/2018/8427390

29. Liu, B., Xinghua, L., & Li, Z. (2018). Impacts of CO_2–brine–rock interaction on sealing efficiency of sand caprock: A case study of Shihezi formation in Ordos Basin. Advances in Geo-Energy Research, 2(3), 223–234.

30. Lu, H., et al. (2024). Uncertainty Quantification of Fluid Leakage and Fault Instability in Geologic CO_2 Storage.

31. Luu, K., Rutqvist, J., & others. (2021). Coupled Hydromechanical Modeling of Induced Seismicity from CO2 Injection in the Illinois Basin. Journal of Geophysical Research: Solid Earth.
32. Machado, M. V. B., Anjude, J., Aroskay, A. Z., & Sepehrnoori, K. (2024). A strategy for enhanced carbon storage: A hybrid CO_2 and aqueous formate solution injection to control buoyancy and reduce risk. Energies
33. Malik, A., et al. (2016). Trends in global greenhouse gas emissions from 1990 to 2010. Environmental Science & Technology.
34. Morris, J., & Cleary, P. (2009). Advances in discrete element methods for geomechanics. Geomechanics and Geoengineering.
35. Mortazavi, A., & Maratov, T. (2024). A numerical study of fault reactivation mechanisms in CO_2 storage. ACS Omega, 9(1), Article pending. https://doi.org/10.1021/acsomega.3c07188
36. Mortazavi, A., and T. Maratov. "An Investigation of Fault Geometric Effects on Fault Activation Mechanisms in CO_2 Storage." Paper presented at the 58th U.S. Rock Mechanics/Geomechanics Symposium, Golden, Colorado, USA, June 2024. doi: https://doi.org/10.56952/ARMA-2024-0584
37. Mortazavi, A., and T. Maratov. "Investigation of Fault Activation Mechanisms in Carbon (CO_2) Storage." Paper presented at the International Geomechanics Symposium, Al Khobar, Saudi Arabia, October 2023. doi: https://doi.org/10.56952/IGS-2023-0009
38. Nunes, L. J. R. (2023). The rising threat of atmospheric CO_2: A review on the causes, impacts, and mitigation strategies. Environments.
39. Onuma, T., & Ohkawa, S. (2009). Detection of surface deformation related with CO2 injection by DInSAR at In Salah, Algeria. Energy Procedia, 1(1), 2177–2184. https://doi.org/10.1016/j.egypro.2009.01.283
40. Osei, H. (2024). A CCUS optimisation for a greener tomorrow using a proxy model driven numerical simulation. Trends in Petroleum Engineering
41. Peter-Borie, M., Dedecker, F., & collaborators. (2011). A particulate rock model to simulate thermo-mechanical cracks induced in the near well by supercritical CO_2 injection.

42. Punnam, P. R., Yarrapragada, K., Raju, S., & Surasani, V. K. (2022). Influence of caprock morphology on solubility trapping during CO_2 geological sequestration. Geofluids, 2022, Article ID 5249027. https://doi.org/10.1155/2022/5249027
43. Reyes-Montes, J., Young, R., & collaborators. (2011). Numerical modeling of microseismicity induced by CO_2 injection.
44. Rinaldi, A. P., & Rutqvist, J. (2013). Modeling of deep fracture zone opening and transient ground surface uplift at KB-502 CO_2 injection well, In Salah, Algeria. International Journal of Greenhouse Gas Control, 18, 220–233. https://doi.org/10.1016/j.ijggc.2013.07.003
45. Rinaldi, A., et al. (2014). Effects of fault-zone architecture on earthquake magnitude and gas leakage related to CO_2 injection.
46. Ringrose, P., Iding, M., Mathieson, A., & Wright, I. (2008). Plume estimation around well KB-502 at the In Salah gas development CO2 storage site
47. Rohmer, J., & Allanic, C. (2013). Influence of Complex Internal Structures of Reservoir-scale Fault Zones on Shear Reactivation Induced by CO_2 Injection.
48. Rongved, M., & Cerasi, P. (2019). Simulation of Stress Hysteresis Effect on Permeability Increase Risk Along a Fault. Energies, 12(15), 2970.
49. Rucci, A., Vasco, D. W., & Novali, F. (2011). Monitoring the geologic storage of carbon dioxide using multicomponent SAR interferometry. Geophysical Journal International, 185(2), 593–606. https://doi.org/10.1111/j.1365-246X.2011.04964.x
50. Rutqvist, J. (2012). The Geomechanics of CO_2 Storage in Deep Sedimentary Formations.
51. Rutqvist, J., & Tsang, C. F. (2002). A study of caprock hydromechanical changes associated with CO2-injection into a brine formation. Environmental Geology.
52. Rutqvist, J., Birkholzer, J. T., Cappa, F., & Tsang, C.-F. (2010). Coupled reservoir-geomechanical analysis of CO_2 injection and ground deformations at In Salah, Algeria. International Journal of Greenhouse Gas Control, 4(2), 225–230. https://doi.org/10.1016/j.ijggc.2009.10.015
53. Saber, E., Chen, Z., & others. (2023). A New Coupled Approach to Simulating Fault Reactivation During CO2 Sequestration. Presented at Day 1 Tue, November 14, 2023.

54. Sang, G., & Liu, S. (2021). Carbonate caprock–brine–carbon dioxide interaction: Alteration of hydromechanical properties and implications on carbon dioxide leakage. SPE Journal, 26(6), 3777–3791. https://doi.org/10.2118/207065-PA
55. Seabra, G. S., Vossepoel, F. C., Lin, Y., Oliveira, M., & de Oliveira, A. (2024). Unveiling valuable geomechanical monitoring insights: Exploring ground deformation in geological carbon storage. Applied Sciences, 14(1), 122. https://doi.org/10.3390/app14010122
56. Shen, C., Zeng, F., Wang, J., & Guo, X. (2024, March 13). Geomechanical modeling and minimum fracture pressure prediction of CO_2 storage reservoir caprock in the Lloydminster area. Day 1 Wed, March 13, 2024.
57. Shi, J.-Q., Durucan, S., Mathieson, A., & Amooie, M. A. (2019). History matching and pressure analysis with stress-dependent permeability using the In Salah CO_2 storage case study. International Journal of Greenhouse Gas Control, 80, 1–11. https://doi.org/10.1016/j.ijggc.2018.11.008
58. Shu, X., Meng, L., & Xu, H. (2024). Evaluation of caprock sealing performance for CO_2 saline aquifer storage: A numerical study. Processes, 12(1), 33. https://doi.org/10.3390/pr12010033
59. Silva, J. A., et al. (2024). Mechanisms for Microseismicity Occurrence Due to CO_2 Injection at Decatur, Illinois.
60. Song, J., & Zhang, D. (2013). Comprehensive review of caprock-sealing mechanisms for geologic carbon sequestration. Environmental Science & Technology, 47(1), 9–22. https://doi.org/10.1021/es301983f
61. Takarada, K., Kawasaki, S., & collaborators. (2024). Development of a numerical simulation method for complex fracture process of rocks based on 3D ECZM-FDEM using GPGPU.
62. Tavassoli, S., et al. (2018). Modeling Fault Reactivation Using Embedded Discrete Fracture Method.
63. Tomac, I., Sauter, M., & collaborators. (2015). Effect of fracture surface damage on fluid flow and transport in geo-reservoirs.
64. Trujillo, N., Heath, J. E., Mozley, P. S., & Cather, M. (2021). Multiscale assessment of caprock integrity for geologic carbon storage in the Pennsylvanian Farnsworth Unit, Texas, USA. Energies, 14(8), 2268. https://doi.org/10.3390/en14082268

65. Vilarrasa, V. (2016). The role of the stress regime on microseismicity induced by overpressure and cooling in geologic carbon storage.

66. Vilarrasa, V., Rutqvist, J., Rinaldi, A. P., Cappa, F., & Laloui, L. (2015). Thermal and capillary effects on the caprock mechanical stability at In Salah, Algeria. Greenhouse Gases: Science and Technology, 5(4), 538–553. https://doi.org/10.1002/ghg.1514

67. Wenning, Q., et al. (2020). Fault hydromechanical characterization and CO_2-saturated water injection at the CS-D experiment.

68. White, J. A., Foxall, W., & McNab, W. (2014). Geomechanical behavior of the reservoir and caprock system at the In Salah CO_2 storage project. Proceedings of the National Academy of Sciences of the United States of America, 111(24), 8747–8752. https://doi.org/10.1073/pnas.1316446111

69. Xia, Q., et al. (2020). Drivers of global and national CO_2 emissions changes, 2000–2017. Climate Policy.

70. Yang, G., Liu, H., Wang, Y., Li, Y., Hou, Z., Li, Y., & Wang, F. (2020). Geochemical modelling of the evolution of caprock sealing capacity at the Shenhua CCS demonstration project. Minerals, 10(5), 445. https://doi.org/10.3390/min10050445

71. Yoon, S., et al. (2024). Assessing CO_2 Leakage Risks and Fault Stability: A Coupled Flow and Geomechanics Simulation.

72. Zappone, A., et al. (2020). Fault sealing and caprock integrity for CO_2 storage: an in situ injection experiment.

73. Zhang, R., Harbert, W., Vasco, D., & Wong, T.-F. (2015). Characterization of a fracture zone using seismic attributes at the In Salah CO_2 storage project. Interpretation, 3(3), SH55–SH66. https://doi.org/10.1190/INT-2014-0260.1

74. Zhang, R., Vasco, D. W., Harbert, W. P., & Wong, T.-F. (2015). Improving thin-bed resolution: Application of a sparse-layer inversion on 3D seismic observations from the In Salah carbon dioxide storage project. Interpretation, 3(3), SH35–SH54. https://doi.org/10.1190/INT-2014-0177.1